



# LIBRARY Michigan State University

This is to certify that the

thesis entitled

The Bonding Mechanism of

Aramid Fibers to Epoxy Matrices

presented by

TAVAD KALANTAR

has been accepted towards fulfillment

of the requirements for

Master of Science degree in Department of

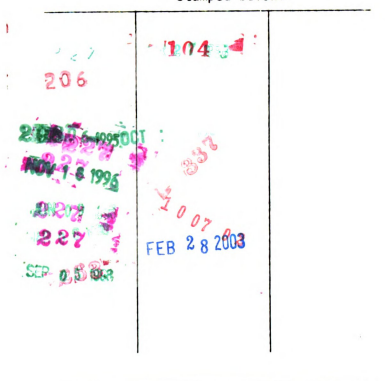
Chemical Engineering

Major professor

**O**-7639

MSU is an Affirmative Action/Equal Opportunity Institution

MSU LIBRARIES RETURNING MATERIALS: Place in book drop to remove this checkout from your record. FINES will be charged if book is returned after the date stamped below.



### **PLEASE NOTE:**

In all cases this material has been filmed in the best possible way from the available copy. Problems encountered with this document have been identified here with a check mark  $\sqrt{\phantom{a}}$ .

1.	Glossy photographs or pages
2.	Colored illustrations, paper or print
3.	Photographs with dark background
4.	Illustrations are poor copy
5.	Pages with black marks, not original copy
6.	Print shows through as there is text on both sides of page
7.	Indistinct, broken or small print on several pages
8.	Print exceeds margin requirements
9.	Tightly bound copy with print lost in spine
10.	Computer printout pages with indistinct print
11.	Page(s) lacking when material received, and not available from school or author.
12.	Page(s)seem to be missing in numbering only as text follows.
13.	Two pages numbered Text follows.
14.	Curling and wrinkled pages
15.	Dissertation contains pages with print at a slant, filmed as received
16.	Other



# THE BONDING MECHANISM OF ARAMID FIBERS TO EPOXY MATRICES

By

Javad Kalantar

### **A THESIS**

Submitted to

Michigan State University
in partial fulfillment of the requirements
for the degree of

### **MASTER OF SCIENCE**

Department of Chemical Engineering

Winter 1988

### **ABSTRACT**

## THE BONDING MECHANISM OF ARAMID FIBERS TO EPOXY MATRICES

By

### JAVAD KALANTAR

The interface between aramid fibers and epoxy matrices lacks the level of adhesion attained by other reinforcing fibers. For aramid composites, the interfacial properties attained to date are acceptable, but less than optimal for some applications. By developing a basic understanding of the interfacial interactions between aramid fibers and epoxy matrices, fundamental approaches for improving the adhesion can be identified.

Three types of interfacial interactions have been examined: mechanical interactions that include thermal strain and Poisson's ratio differences between fiber and matrix, chemical interactions that include covalent bonding and fiber-matrix wetting, and physicochemical weak boundary layers. Each of these interactions has been evaluated by manipulating the interface and the curing conditions. Both aramid and carbon fibers have been examined in order to access the interfacial interaction by comparing the behavior of these two fibers.

Our results indicate that the adhesion of aramid fibers to epoxy matrices lacks the mechanical and chemical interactions present in carbon-epoxy adhesion. Aramid fibers exhibit an interfacial shear strength as much as four times lower than the expected theoretical value. Direct observation of the aramid-epoxy interface, by transmission electron microscopy, shows fibrillar separations within the fiber surface. This type of interfacial failure suggests that <u>low aramid-epoxy</u> adhesion could be due to fiber surface failures.

TO MOHAMMAD JAHAN

### Acknowledgement

This work was accomplished at the Composite Materials and Structures Center (CMSC), at Michigan State University. I want to thank Dr. L. T. Drzal for the opportunity to be exposed to the project and his support, assistance, and patience during my work.

I wish to gratefully acknowledge E. I. du Pont de Nemours & Co. for its financial and research support.

Finally, I would like to express my appreciation to the Staff of Center for Electron Optics for their help and informative discussions.

### **Table of Contents**

List of Tables	vii
List of Figures	viii
Nomenclature	ix
Introduction	1
Background	4
Composite Interface	4
Polyaramid Fibers	5
Mechanical Properties of Aramid Fibers	12
Carbon Fibers	15
Epoxy Matrices	16
Aramid-Epoxy Adhesion	21
Aramid-Epoxy Interface	23
Microstructural Approach	23
1. Mechanical Interlocking	24
2. Adsorption Interactions	24
3. Electrostatic Attractions	25
4. Polymer Interdiffusion	25
Macrostructural Approach	26
1. Mechanical Interactions	26
Surface Topography	26
Thermal Stresses	28
Poisson's Ratio Difference	29

2. Wetting	30
3. Weak Boundary Layers	30
Theory	33
Experimental	37
Results and Discussion	42
Thermal Stresses	42
Chemical Bonding	46
Poisson Contraction	48
Fiber Wetting	50
Three dimensional stress model	50
Electron Microscopy	60
Conclusions and Recommendations	69
Appendix A: Three-Dimensional Stress Model	72
Appendix B: Critical Length distributions	76
Appendix C: Thermal Expansion Data	101
Appendix D: Microtoming Technique	108
Deferences	112

### List of Tables

Table 1	Material properties of Kevalr	49 and As-4 fibers.	•••••	13

### List of Figures

Figure 1	The sample conditions and the interactions present at each condition		
Figure 2	Structure of polyaramid PPTA monomer.	7	
Figure 3	Dobb and Johnson model for the aramid pleated structure	9	
Figure 4	Morgan's model for the aramid fibrillar morphology.	10	
Figure 5	Model of carbon fiber ribbon morphology.	17	
Figure 6	Structure of DGEBA epoxy.	19	
Figure 7	Structure of DETA, MPDA, and DETDA curing agents.	20	
Figure 8	SEM micrographs of fracture surfaces of unidirectional AS-4/epoxy and Kevlar 49/epoxy composites.	22	
Figure 9	Tensile jig for the critical length technique and a sample mold	39	
Figure 10	Plot of % thermal shrinkage of the epoxy matrices	43	
Figure 11	Plot of experimental interfacial shear strength of untreated carbon and aramid fibers with epoxy matrices cured at different temperatures	45	
Figure 12	Plot of experimental interfacial shear strength of untreated and gold coated carbon and aramid samples made with 75°C and 125°C cured epoxy	47	
Figure 13	Plot of interfacial shear strength of untreated, gold coated, and silicone coated carbon and aramid samples made with the room cured epoxy	49	
Figure 14	Plot of interfacial shear strength of untreated, gold coated, and silicone coated aramid with epoxy matrices cured at different temperatures	51	
Figure 15	Plot of epoxy elastic modulus cured at different temperatures	52	
Figure 16	Plot of theoretical and experimental critical lengths for aramid and carbon fibers with epoxy matrices cured at different temperatures	54	
Figure 17	Plot of theoretical and experimental average interfacial shear stress over the critical lengths for aramid and carbon samples.	55	
Figure 18	Optical micrographs of fiber fragment at their critical lengths with bright-field and cross-polarized light.	57	
Figure 19	Plot of theoretical average radial stresses for aramid and carbon fibers with epoxy matrices cured at different temperatures.	59	
Figure 20	TEM micrographs of Kevlar 49 and (50/50) epoxy matrices cured at 175°C (lognitudinal cut).	62	
Figure 21	TEM micrographs of Kevlar 49 and room-cured epoxy (radial cut)	63	
Figure 22	SEM micrographs of a single Kevlar 49 fiber	64	
Figure 23	TEM micrographs of a surface damaged Kevlar 49 in a epoxy matrix cured at 175°C (radial cut).	65	
Figure 24	TEM micrographs of a surface damaged Kevlar 49 in an epoxy matrix cured at $175^{\circ}$ C (radial cut). The section is stained with $OsO_4$	66	
Figure 25	TEM micrographs of a shear damaged Kevlar 49 in an epoxy matrix cured at 75°C (radial cut).	67	
Figure 26	TEM micrographs of a shear damaged Kevlar 49 in an epoxy matrix cured at 75°C (radial cut).	68	
Figure 27	Diagram of stress distributions around a fiber fragment.	75	

### **Nomenclature**

 $A_1$  = Elastic constant for fiber longitudinal stress, MPa

 $A_2$  = Elastic constant for fiber radial stress, MPa

 $A_3$  = Elastic constant for fiber radial displacement

 $A_{\Delta}$  = First elastic constant for matrix radial displacement

 $A_5$  = Second elastic constant for matrix radial displacement

 $E_{1f}$  = Axial fiber elastic modulus, MPa

 $E_{2f}$  = Radial fiber elastic modulus, MPa

 $E_m$  = Matrix elastic modulus, MPa

 $G_{2f}$  = Radial fiber elastic shear modulus, MPa

 $G_m$  = Matrix elastic shear modulus, MPa

 $K_f$  = Plane strain bulk modulus, MPa

 $l_c$  = Critical length,  $\mu$ m

r = Radial coordinate,  $\mu$ m

R = Fiber radius,  $\mu$ m

 $T_c$  = Curing temperature, °C

 $T_g$  = Glass transition temperature, °C

 $u_{xrf}$  = Longitudinal fiber displacement

 $u_{xrm}$  = Longitudinal matrix displacement

 $v_{rf}$  = Radial fiber displacement

 $v_{rm}$  = Radial matrix displacement

x = Longitudinal coordinate,  $\mu$ m

 $\overline{x}$  = Dimensionless longitudinal coordinate

### Greek

α = Weibull shape parameter = Matrix coefficient of thermal expansion, ppm/°C  $\alpha_m$ = Axial fiber coefficient of thermal expansion, ppm/°C  $\alpha_{1f}$ = Radial fiber coefficient of thermal expansion, ppm/°C  $\alpha_{2f}$ β = Weibull scale parameter, μm  $\Delta T$ Temperature difference between ambient and oven condition, °C = Far field axial strain  $\epsilon_0$ = Fiber fracture strain  $\epsilon_{uf}$ = Matrix thermal strain  $\overline{\varepsilon}_m$  $\overline{\varepsilon}_{1f}$ = Longitudinal fiber thermal strain = Radial fiber thermal strain  $\overline{\epsilon}_{1f}$ = Matrix Poisson's ratio  $V_m$ = Axial fiber Poisson's ratio  $v_{12f}$ Radial fiber Poisson's ratio, assume to be equal to  $v_{12f}$  $v_{21f}$ = Fiber tensile strength, MPa  $\sigma_{uf}$  $\sigma_{xf}$ = Longitudinal fiber stress, MPa = Radial fiber stress, MPa  $\sigma_{rf}$ Longitudinal matrix stress, MPa  $\sigma_{m}$ 

 $\sigma_{rm}$  = Radial matrix stress, MPa

 $\overline{\sigma}_r$  = Average interfacial radial stress, MPa

 $\overline{\tau}_u$  = Interfacial shear strength, MPa

 $\tau_{xrf}$  = Fiber shear stress, MPa

 $\tau_{xrm}$  = Matrix shear stress, MPa

 $\overline{\tau}_{xr}$  = Average interfacial shear stress, MPa

 $\phi$  = Bulk constant

### INTRODUCTION

Aramid fibers have a unique combination of stiffness, high strength, and low—density which rivals the properties of inorganic reinforcing fibers such as glass and—carbon. Advanced composites made of aramid fibers have excellent axial properties—as compared to inorganic fibers, but their off-axis properties are less than optimum—for some applications. The off-axis properties of fiber-reinforced composites are—generally controlled by the level of fiber-matrix adhesion.

In this study, attempts are made to understand the adhesion interactions of aramid fibers with epoxy resins. These adhesion interactions are: mechanical strains, chemical interactions, and effects of physicochemical weak boundary layers. Mechanical strains are caused by thermal shrinkage and Poisson's ratio differences between fiber and matrix. Chemical interactions include wetting and covalent bonding. The wetting of the fiber with liquid epoxy insures intimate molecular contact between them which is a prerequiste for covalent chemical bonding. Weak boundary layers can reduce the efficency of load transfer at the interface and significantly affect other interfacial interactions. Application of controlled weak boundary layers is used to manipulate fiber-matrix interactions.

The approach of this study is to separate and qualitatively analyze the adhesion interactions by modifying the curing conditions and the fiber surface. Figure 1 illustrates the experimental plan.

Sample	Mechanical Interactions		Chemical Interactions	
Conditions	Thermal Stress	Poisson Contraction	Covalent Bonding	Wetting
Untreated Fibers & Elevated Temp. Cured	+	+	+	+
Untreated Fibers & Room Temp. Cured		+	+	+
Gold Coated Fibers & Elevated Temp. Cured	+	+		+
Silicone Coated Fibers & Elevated Temp. Cured	+	+		
Gold Coated Fibers & Room Temp. Cured		+		+
Silicone Coated Fibers & Room Temp. Cured		+		

Figure 1 - The experimental sample conditions and the interactions present at each condition.

As shown in Figure 1, various combinations of epoxy curing temperatures and fiber surface modifications have allowed distinguishing different interaction mechanisms.

Gold and silicone coating of the fibers are the two types of surface treatments — examined. Both treatments introduce physicochemical weak boundary layers which effectively eliminated all the covalent bonds that might be present at the fiber-matrix interface, but also modified the thermodynamics of the fiber surface. Gold coating has produced an inert, yet wettable fiber surface. Silicone coating has produced an inert, but non-wettable fiber surface.

Carbon fibers have physical and chemical properties that are distinctly different from aramid fibers. Comparison of these two types of fibers in samples made with the same epoxy has enabled the effects of different interactions to be distinguished.

A three-dimensional linear elastic stress model is used to compare the experimental data with their theoretical values. The model has been developed by Whitney et al. [1]. For a single fiber fragment, stress distributions and critical lengths are predicted by the model.

A direct observation of the aramid-epoxy interface is carried out by microtoming the single-fiber samples and examining them by transmission electron microscopy.

### **BACKGROUND**

### **Composite Interphase**

The mechanical behavior of composite materials reflects the interactions between their various constituents. When a load is applied to a fiber reinforced composite, the load is transferred between matrix and fiber through their interphase.

A strong interphase promotes greater involvement of the fibers, thus contributing to the composite strength. The fiber-matrix interphase also determines the failure mode of the composite. At high levels of adhesion, the failure would start with matrix cracks, but at lower adhesion levels, failure occurs along the fiber-matrix interphase.

For continuous fiber-reinforced composites, the fiber-matrix interphase is symmetric along the fiber longitudinal axsis, and is commonly referred to as the fiber-matrix—"interface".

Composite behavior is significantly affected by the condition of its interface [2]. In particular, off-axis properties such as interlaminar shear and transverse strength can be improved by increasing interfacial bonding. Improved interfacial—adhesion also enhances the environmental stability of polymeric composites by reducing the formation of weak boundary layers. However, for some applications such as fracture toughness, a low level of fiber-matrix adhesion is desirable. In general, the optimum condition for interfacial strength depends on the particular application and its expected loads.

In elementary treatments of the composite tensile properties, the effects of the interface are usually ignored [3]. In practice, the interfacial properties have moderate to critical influences on many mechanical or thermal properties of the composite. Studies by Drzal et al. [4] and Owen [5] on carbon fibers with different surface properties have demonstrated the significance of interfacial properties on fiber-dominated composite properties. Peters et al. [6] have shown that the mechanical properties of the composite are affected more by the interfacial condition of the fiber-matrix than by the degree of the cure of the matrix. Such observations suggest that the curing cycles of the resin should be optimized with respect to the desired fiber-matrix adhesion rather than optimum matrix mechanical properties.

At low levels of fiber-matrix adhesion, fracture toughness and impact resistance of the composites usually increase. A report by Chang et al. [7] on carbon-epoxy composites with controlled interfaces has shown an inverse relation between interlaminar shear strength and impact resistance of the composite. Similar works by Mai et al. [8], on fracture toughness of Kevlar-epoxy composites has demonstrated a 200% to 300% greater fracture toughness for Estapol-7008 coated fiber composites than uncoated fiber composites. The above studies has shown that a very high level of fiber-matrix adhesion can be detrimental to fracture toughness and impact resistance of the composites.

### **Polyaramid Fibers**

At molecular levels, the strength of organic polymers is related to the rupture of their carbon-carbon bonds. In theory, the material strength can be calculated from the carbon-carbon bond dissociation energy (~ 83 kcal/mole) and the packing of the polymers [9]. However, for most solid materials, the measured strength of the bulk is several orders of magnitude smaller than the theoretical values. The main reason is the existence of flaws or defects in the structure of the material. Misalignment in

the orientation of the polymer chains, broken chain ends, and slippage of the chains can lead to stress concentrations on a few bonds which cause chain rupture and catastrophic failures. To reach high material strengths, certain highly ordered polymer morphologies are required. Polymer chain packing, orientation, and extension significantly affect the material strength. The distribution of flaws and cracks which are detrimental to the strength and must also be minimized.

During the past two decades, considerable progress has been made in the production of high performance synthetic fibers [10,11]. These fibers have high degrees of crystallinity and their ultimate properties approach their theoretical maximums. The most successful high performance organic fibers have been prepared from wholly aromatic polymers [12]. These fibers have high modulus, high strength, and are not brittle. Preston [13] has reviewed the development of aromatic polymer fibers.

To date, the most successful high-performance organic fibers have been polyaramid fibers. E.I. du Pont is the major manufacturer of one type of aramid fiber which is marketed under the trade name Kevlar. Three types of Kevlar fibers are available for specific applications: (1) High modulus Kevlar 49 for composite reinforcement, (2) intermediate modulus Kevlar 29 for ropes and fabrics, and (3) tire cord Kevlar. Since its introduction in 1971, Kevlar has become the major reinforcing fiber for applications where toughness and impact resistance is required [14].

Kevlar fibers consist of extended chains of highly oriented rod-like molecules [15,16] formed into fibers with a nominal diameter of 12 μm. The aramid monomer is para-Phenylene Terephthalamide (PPTA) and its chemical structure is shown in Figure 2. The polymer chains are oriented in the fiber longitudinal direction and are hydrogen bonded to each other. The structure of Kevlar fibers is not well documented, but some conclusions about their morphology can be made.

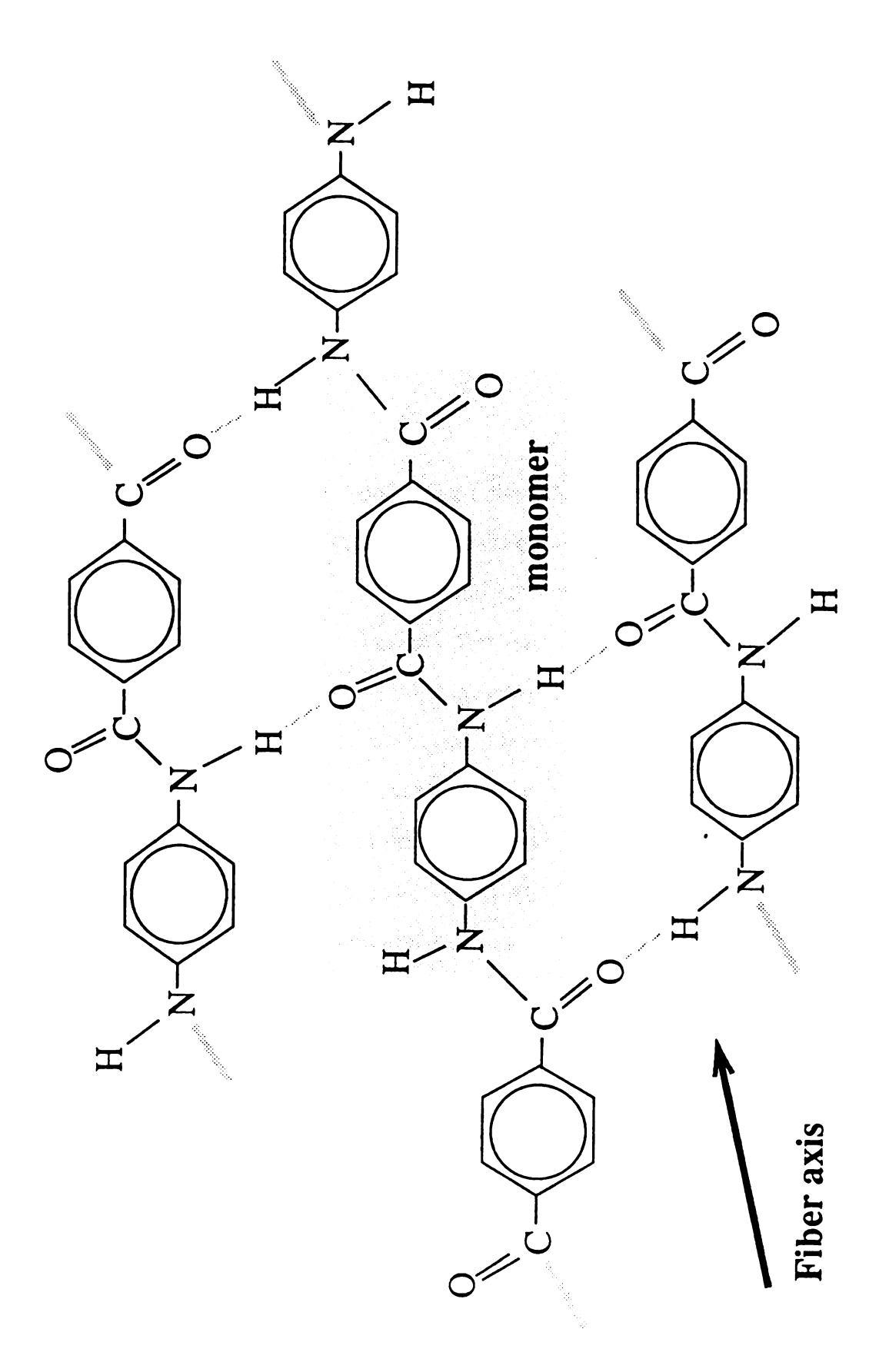


Figure 2 - Structure of polyaramid PPTA monomer

Dobb et al. [17], using electron diffraction and electron microscope dark-field image studies, have reported that the structure of Kevlar 49 fiber consists of sheets of polymer chains radially arranged and held together by hydrogen bonding (Figure 3). These sheets are regularly pleated along the axial direction of the fiber, with a pleat angle of about 170°. Over small transitional sections between the pleated sheets, the PPTA polymers are parallel to the axial plane; this feature eliminates the possibility of rotational molecular orientation. Dobb has observed two main types of 500 nm and 250 nm periodicities in the fibers, but near the edges of the fiber he has reported evidence of marked changes in the spacing.

Morgan et al. [18] have studied the relation between Kevlar fibers failure process and its structure. While not disputing the pleat morphology of the fiber, they have suggested that the primary structural factor affecting the deformation and failure of the fiber is the concentration and distribution of the supermolecular chain ends within the fiber. Based on the fiber fabrication procedure, structure of the PPTA crystals, microscopic deformation, and fracture topography studies, they have proposed a model of chain-end distribution. In this model shown in Figure 4, chainend distributions are random in the fiber exterior, but progressively more aligned and clustered in the interior. Morgan's model suggests a skin-core morphology for the fiber with random chain distribution at the skin and periodic weak planes at the core. The periodicity of the weak planes is about 200 nm, which is the suggested average length of a PPTA micromolecule rod. Morgan further suggests that PPTA macromolecules are clustered into cylindrical crystals with 60 nm diameter and 200 nm length. A large percentage of macromolecules transverse the weak plane, keeping the continuity of the crystals in the axial fiber direction. It can be inferred from Morgan's model that crack propagation can readily occur parallel to the rods and across the weak planes, leading to fiber fibrillations.

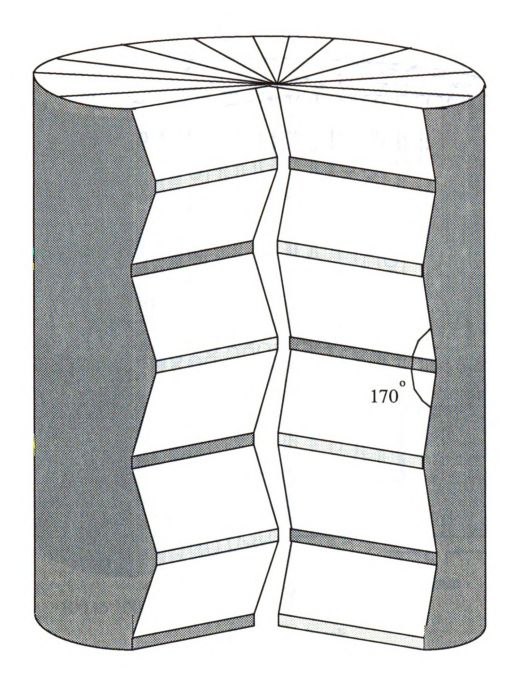


Figure 3 - Dobb and Johnson model for the aramid fiber structure. The diagram shows a system of radially pleated polymer planes.

A small vertical section is located between each pleat.

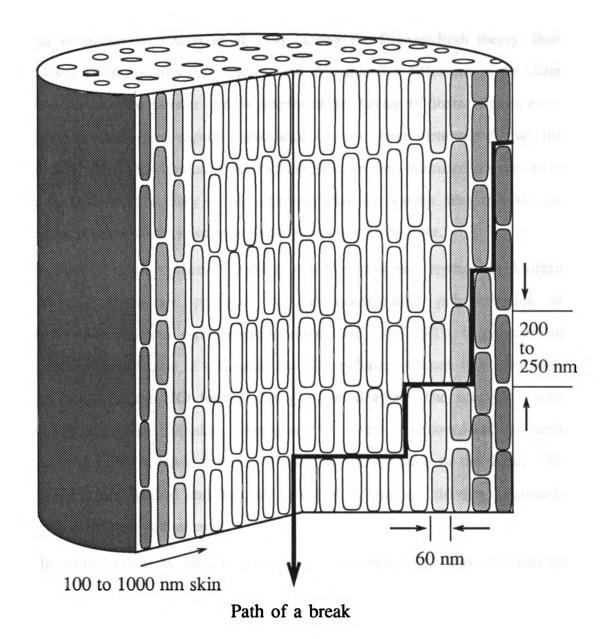


Figure 4 - An exaggerated model of aramid fiber morphology proposed by

Morgan. The PPTA chains are ramdomly distributed in the fiber
exterior and progressively more clustered at the interior. Such
a sturcture results in skin-core difference in the fiber.

Morgan's suggested skin-core morphology and chain-end distribution model has been implied by other workers. Skin-core morphology of the fibers has been suggested in studies by Chatzi et al. [19]. Using the Dignam-Roth theory, their photoacoustic FTIR spectroscopic studies have determined a difference in the chain orientation between the exterior and the interior of the Kevlar 49 fibers. Brown et al. [20], using electron paramagnetic resonance studies, have determined that the concentration of the stress-induced free radicals is more than estimated concentration for the fracture surface. They have suggested that the excess free radicals are produced by polymer chain scission at weak planes within the fiber.

A fiber fabrication process for the aramid fibers has been reported by Morgan [21]. Aramid fibers are produced by the condensation polymerization of terephthaloyl chloride and p-phenylene diamine [22]. The PPTA is polymerized using a stoichiometric ratio of the reactants. The polymer solution is washed with NaOH to neutralize the HCl formed during polymerization. The solution is then extruded into hot walled cylinders, whereupon the solvent is removed and the shear forces cause the PPTA liquid crystals to orient in the direction of the shear. The resulting yarns are washed and the subsequent stretching and drawing treatments increase their stiffness and strength.

In another report by Morgan et al. [23], the chemical impurities in Kevlar 49 fibers have been investigated. They have determined that there are ~ 0.7% of Na<sub>2</sub>SO<sub>4</sub> impurities within the fiber, which are the result of sulfuric acid neutralization step. Similar impurity concentrations have been reported by Penn et al. [24]. Morgan has suggested that Na<sub>2</sub>SO<sub>4</sub> residues in the interfibrillar regions are paths for moisture diffusion, which during fiber fabrication can generate microvoids in the fiber. Ashbee et al. [25] have proposed a chemical volume expansion model to describe the hydration expansion which can result in fiber fracture. Based on "salt-weathering" mechanisms in geology, Whalley et al. [26] have confirmed the

possibility of a Na<sub>2</sub>SO<sub>4</sub> hydration fracture mechanism. Small angle X-ray scattering studies by Lee *et al.* [27] have suggested that failure of *Kevlar 49* fibers is due to increases in the volume fraction of microvoids and their enlargement along the fiber axis direction.

### **Mechanical Properties of Aramid Fibers**

Chiao et al. have documented the common properties of aramid fibers and their composites [28]. Table 1 lists the mechanical properties of Kevlar 49 relevant to this study.

Kompaniets et al. [29] have examined the statistical aspects of aramid fiber tensile strength. They have reported that for both monofilament and yarns, the tensile strength decreases with an increase in gage length, but the tensile strength of the unidirectional composites was found to be unaffected by the gage length. Their tensile strength data were also independent of the deformation rate (1 to 20 mm/min). Many investigators have attempted to model the strength and modulus behavior of the *Kevlar* fibers. Knoff [30] has proposed a modified weakest-link model to describe the tensile strength of the fibers as a function of test length. His experimental results have suggested that for aramid fibers below 1 cm gage length, the tensile strength only slightly increases with decreasing length, but above 1 cm the tensile strength is strongly dependent on the gage length. Their model can be considered to describe the aramid fibers as a series of approximately 1 cm uniform strength links.

Table 1 - Material properties of Kevlar 49 and AS-4 fibers

Property	Ref.	Kevlar 49	AS-4
E <sub>1f</sub> (GPa)	[83]	119	231
E <sub>2f</sub> (GPa)	[1]	6.9	21
$ m v_{12f}$	[1]	0.35	0.25
G <sub>2f</sub> (GPa)	[1]	2.6	8.3
α <sub>1f</sub> ppm/°C	[79],[1]	-5.72	-2
α <sub>2f</sub> ppm/°C	[79],[1]	65	8.5
σ <sub>uf</sub> (GPa)	[83]	3.31	5.86
$\mathbf{\epsilon}_{\mathrm{uf}}$ (%)	[83]	2.5	1.4

Compressive buckling of aramid fibers has been modeled by DeTeresa et al.

[31]. They have suggested that the compressive strength of the fibers should be proportional to either the shear modulus or the shear strength of the fibers. Another report by DeTeresa et al. [32], describes a new technique to determine the compressive and torsional behavior of the Kevlar 49 fibers. A torsional pendulum has been developed and ratios of (5:1) tensile-to-compressive strength, (17:1) tensile-to-shear strength, and (70:1) tensile-to-shear moduli have been reported. White et al. [33] have proposed an interesting mechanical model to describe compressive buckling of the aramid fiber. Their model involves the classical mechanics spring, dashpot, and rigid rods elements. This model can describe both the compressive buckling and the stress-strain characteristic under tensile loading after the buckling.

Fatigue, creep, and failure behavior of aramid fibers have been studied by several workers. Wagner et al. [34] have investigated the creep-rupture statistics of the Kevlar 49 fibers. They have observed that for a given stress level, fibers with 7% lower tensile strength show an order of magnitude lower rupture lifetime. Wagner et al. have suggested a power law dependence for the creep behavior, with different regions of power-law exponents. Lafitte et al. [35] have reported similar multi-region power law creep behavior for Kevlar 29 fibers. In another fatigue study by Lafitte et al. [36] the tensile strength variability of Kevlar 29 fibers has been attributed to the distribution of defects in the fibers. Cook [37] has suggested a kinetic model for Kevlar 49 creep-failure behavior that allows prediction of its rupture lifetime.

Several techniques for determining the failure mode of aramid fibers has been reported. Fracto-emission studies by Dickinson et al. [38] have indicated a correlation between total emission of electron and positive ions with the extend of fibrillation in a Kevlar fiber. Acoustic emission (AE) techniques on Kevlar 49 fibers by Hamstad et al. [39] have been less fruitful. The load at which the failure of a

single fiber occurred was not directly correlatable with the AE event peak amplitude.

An interesting model for longitudinal splitting from surface defects has been set forth by Wagner [40] which allows the prediction of onset and growth of the cracks from surface flaws.

### **Carbon Fibers**

Carbon fibers are the most widely used high-performance reinforcing fibers. Carbon fibers have distinctly different properties from aramid fibers. This study has concentrated on the adhesion properties of the aramid fibers, but comparing aramid and carbon fibers is helpful in highlighting the interfacial interactions. The morphology and the surface properties of carbon fibers will be described briefly. Additional details and more extended discussions on carbon fibers and composites are provided in a review article by Riggs *et al.* [41] and the reference book by Donnet and Bansal [42].

In a carbon fiber, the carbon atoms form hexagonal rings which are extended by covalent bonds to form a plane of carbon rings called "basal planes". These planes stack and form layers which are held together by weak van der Waal forces; however, there is little alignment between equivalent carbon atoms in adjacent planes. This crystallographic structure of carbon is referred to as "turbostratic graphite". In the plane of the rings, the tensile moduli is very high (910 GPa), but normal to the rings, the moduli is considerably reduced (30 Gpa). The graphite crystals form ribbon-like structures along their basal planes. The general orientation of the ribbons is along the fiber axis. There is a large number of microvoids existing between the ribbons. As the number of microvoids decreases and the ribbons are more aligned, the tensile modulus and strength of the fiber increases. Diefendorf and Tokarsky [43] have shown that the orientation of the ribbons varies from the surface to the center; with more alignment closest to the surface. This morphology shown in

Figure 5, results in a fiber with more load-carrying capacity on the surface than in its core.

Carbon fibers are usually surface treated in order to enhance their adhesion — properties. Comparison of composite properties of surface treated AS-4 and untreated AU-4 carbon fibers by Drzal et al. [4] has demonstrated the improvement of interface sensitive properties. Most surface treatments tend to modify the interphase by creating fiber surface porosity and increasing the fiber-matrix contact areas. These treatments also improve the reactivity of the surface by forming reactive functional groups, mostly carbonyl and carboxylate. Drzal et al. [44] have demonstrated that another effect of surface treatment is the removal of weak structural layers from the fiber surface which can be a source of interfacial failure. It is usually difficult to assess the relative importance of each mechanism on the improvement of the carbon fiber adhesion.

Mechanical properties of carbon fibers vary significantly among different brands due to different precursors and production techniques available. Table 1 includes some of the mechanical properties of the AS-4 carbon fibers utilized in this study. More detailed discussions of the mechanical properties of carbon fibers are available elsewhere [41,42]. A discussion of statistical aspects of carbon fiber strength distributions has been presented by Phani [45].

### **Epoxy Matrices**

Epoxy resins are the most common resins used in high-performance composites. Epoxies are thermoset resins with a wide range of viscosities and can be reacted with a variety of curing agents to obtain a spectrum of mechanical properties. The chemical reaction between epoxy and the curing agent is referred to as "curing". The reaction forms a three-dimensional crosslinked solid structure. The curing mechanisms and kinetics of epoxy systems have been discussed extensively in

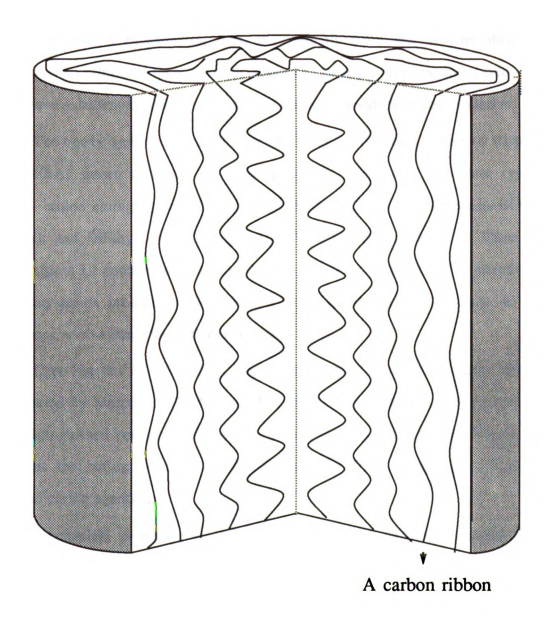


Figure 5 - An exaggerated model of carbon fiber ribbon structure.

The amplitude and wavelength of the ribbons vary from the core to the surface with increasing alignment near the surface.

the literature [46,47]. The mechanical properties of various epoxy systems have been documented by Lee and Neville [48]. Curing reactions of epoxies do not release any volatiles or excess by-products, thus, they usually have low volume shrinkage. Epoxy resins exhibit a high level of adhesion among polymers and cured epoxy resins have excellent chemical resistance and provide good electrical insulation.

The epoxy system used in the present study is Diglycidyl Ether of Bisphenol A (DGEBA) shown in Figure 6. This epoxy has been cured with three types of primary amine curing agents: DiEthyleneTriAmine (DETA); M-PhenyleneDiAmine (MPDA); and DiEthylTolueneDiAmine (DETDA) shown in Figure 7. These three curing agents all contain two similar primary amines at each end. The chemistry of the epoxy-amine crosslinking is identical in all three systems, but due to steric hindrances, each system has different kinetics.

Cure kinetics of the DEGBA epoxy with other aromatic diamines has been investigated by Moroni et al. [49]. In their study, using thermal analysis data, they have distinguished between different kinetic mechanisms. A report by Wiggins [50] compares the curing behavior of DGEBA and DETDA curing agent with other aromatic curing agents.

Mechanical properties of DGEBA systems cured with amine curing agents have been investigated by several workers. For the DGEBA/MPDA system, Gupta et al. [51] have reported the dependence of the mechanical properties on temperature, composition, and the relaxation process. Their results have suggested that, in the glassy state, the tensile modulus is dependent on the intermolecular packing, but in the rubbery state, the crosslinking density is the important factor. The effect of crosslinking density on the glass transition of several amine-cured epoxies has also been examined by Bellenger et al. [52]. Another report by Gupta et al. [53] have examined the free volume and its effect on moisture transport in DGEBA/MPDA system. They have determined that below the glass transition, there is no covalent

# DiGlycidyl Ether of Bisphenol A (DGEBA)

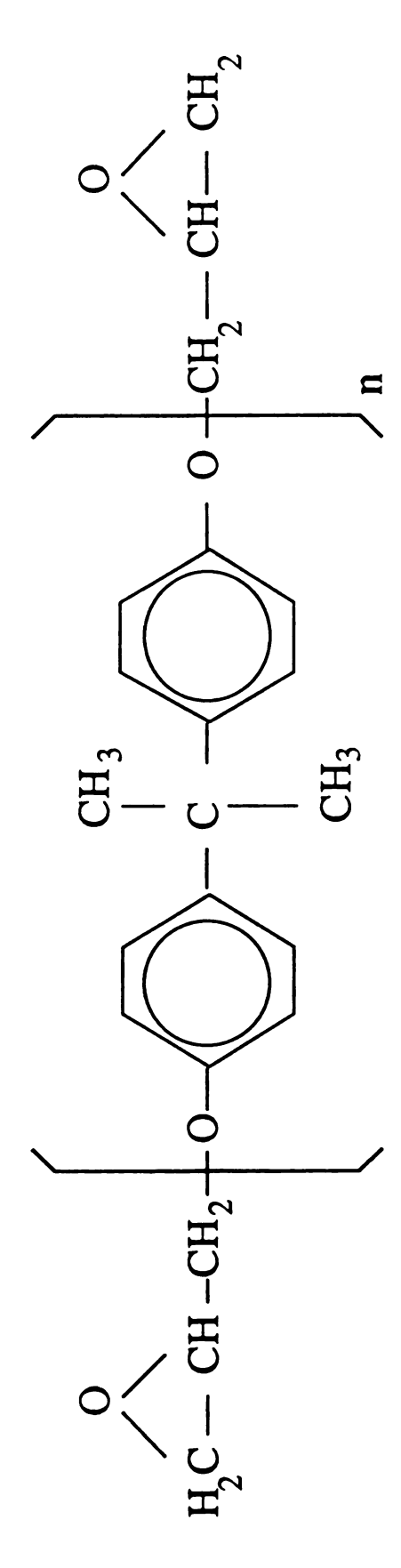
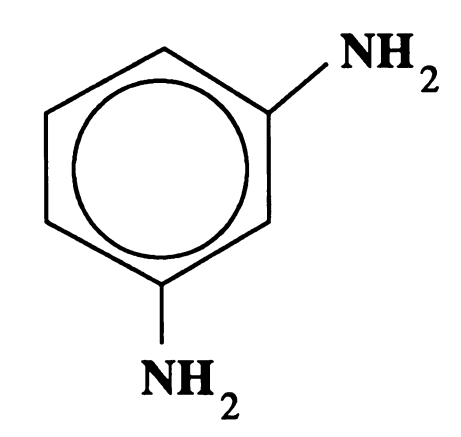


Figure 6 - Structure of DGEBA epoxy.

### DiEthyleneTriAmine (DETA)

$$\begin{array}{c|c} \mathbf{H} \\ | \\ \mathbf{H_2N-CH_2-CH_2-N-CH_2-CH_2-NH_2} \end{array}$$

### m-PhenyleneDiAmine (MPDA)



### DiEthylTolueneDiAmine (DETDA)

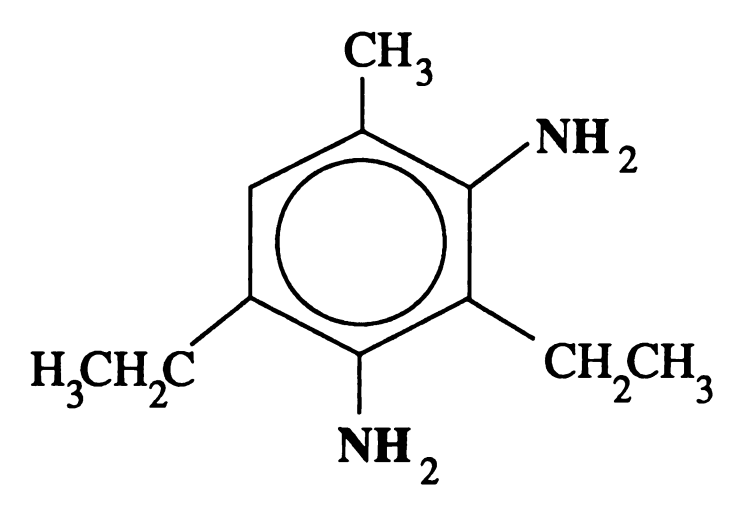


Figure 7 - Structure of DETA, MPDA, and DETDA curing agents.

bond formation with water, but at higher temperatures there would be reactions that can have adverse effects on the modulus of the matrix. Jean et al. [54] have examined the free volume of four epoxy matrices with different crosslinking densities using positron annihilation spectroscopy. Their study has shown that the transitions in free volume coincide with the glass transitions and crosslink density of the polymers. Lee [55] has examined a molecular model to described the plastic deformation of various amine and anhydride cured DGEBA resins and has related his model parameters to the known chemical structures of the resin.

### **Aramid-Epoxy Adhesion**

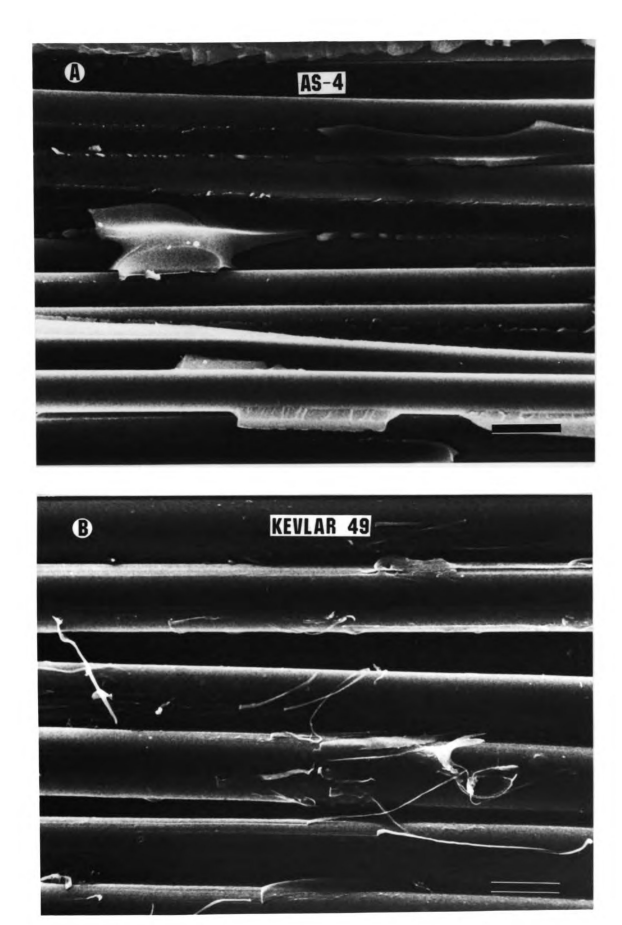
Separation of aramid fibers from an epoxy matrix is characterized by bare fibers with little resin adhering to them. Figure 8 illustrates the fracture surface of unidirectional *Kevlar 49*-epoxy and *AS-4*-epoxy composites. The failure modes of the aramid-epoxy composites are generally interfacial [56,57], with some surface fibrillation. Significant amounts of research have been devoted to the interfacial properties of glass and carbon fibers and many surface treatment techniques and coupling agents have been developed. For glass and carbon fibers these surface treatment techniques can increase the interface strength two or three times [41,58,59]. Development of similar improvement with interfacial treatment methods for the aramid reinforced composites has been difficult.

Cooke [60], Morgan and Allred [21] have documented various attempts on the development of surface treatment techniques for the aramid fibers. Despite many efforts, promising coupling agents have not been developed [61]. Surface treatments such as surface oxidation techniques can improve adhesion but are usually accompanied by loses in fiber tensile strength [62]. More promising approaches have suggested forming chemical active groups on the fiber surface which can then react with epoxy to produce covalent chemical bonds at the fiber-matrix interface.

Figure 8 - SEM micrographs of fracture surfaces of unidirectional composites.

- (A) AS-4/epoxy composite.
- (B) Kevlar 49/epoxy composite.

 $bar = 10 \ \mu m$ 



Two main types of surface chemical modifications have been attempted; chemical plasma treatments and wet chemical reactions. Kevlar 49 plasma treatment has been reported by Allred et al. [63]. Using a RF plasma in the presence of ammonia gas, Allred has reported a two-fold increase in the interlaminar peel strength of treated Kevlar 49-epoxy composites and failure mode changes from interface failure to mixtures of fiber and matrix failure. In the wet chemical reaction approach, Wu et al. [64] have been able to incorporate amine functional groups on the fiber surface by bromination followed by ammonolysis, nitration, and reduction. They have reported results similar to those of Allred.

# **Aramid-Epoxy Interface**

An understanding of the interfacial interactions between fiber and matrix is critical for improving their adhesion. There are two approaches to the investigation of fiber-resin interface. One approach deals with the microstructural aspects of bond forming and concentrates on the chemistry and physics of the interface. The other approach deals with the macrostructural aspects and mechanical analysis of the interface. The two approaches must be combined for a viable explanation of the aramid adhesion. The present study consider concepts from both approaches to develop a practical understanding of the aramid-epoxy adhesion. A brief review of the main concepts of both approaches and their implications on the aramid-epoxy interface follows.

Microstructural aspects of polymer-polymer adhesion have been discussed by Allen [65]. He has explained several mechanisms for polymer-polymer bonding, each involving combinations of physical and chemical interactions. These mechanisms are: mechanical interlocking, adsorption interactions, electrostatic interactions, and interdiffusion of the polymer chain segments.

#### 1. Mechanical Interlocking

Mechanical interlocking of two adhering surfaces is a result of surface irregularities of the two phases. These surface irregularities can act as mechanical anchors, and high bond strengths can be obtained even though other interactions may be weak. This mechanism has a profound influence on the adhesion of porous materials such as wood, paper, and textiles, but for the relatively smooth surfaces of aramid fibers, mechanical interlocking is not expected to be significant.

### 2. Adsorption Interactions

Adsorption interactions refer to processes whereby the molecules of one phase are attracted to specific sites on the other phase. These attractive forces originate from basic chemical interactions, such as covalent chemical bonds and secondary chemical interactions. Covalent bonds involve sharing of electrons among atoms, and are the primary form of chemical interactions (39-111 kcal/mole). Secondary interactions involve electron correlation between molecules and are much weaker chemical interactions (2-6 kcal/mole). Secondary interactions include nonpolar dispersion forces (Van der Waals forces), polar dipole interactions, and polar Lewis acid/base interactions (including hydrogen bonding). All types of adsorption interactions require intimate physical contact between the molecules of the two phases [66], but secondary interactions are effective over greater atomic distances than covalent interactions and are a prerequisite for covalent interactions. To achieve a stable interface, formation of covalent bonds at the interface is very desirable.

The reported results by Allred et al. [63] and Wu et al. [64] on a two fold increase in interlaminar peel strength of aramid composites by forming chemical active groups on the fiber surface can be attributed to the formation of covalent bonds. Timm et al. [67] have put forth the possibility of chemical reactivity of the secondary aromatic amines in Kevlar 49, especially in anhydride cured epoxies.

Using FT-IR techniques, Garton [68] has examined the interface of a model PPTA surface with both anhydride and amine cured DGEBA epoxy. For the aromatic amine cured epoxy, no significant effect from PPTA on the crosslinking was observed; however, for the anhydride cured epoxy the effect of the aramid surface was significant. Garton determined that the changes in the anhydride system were due to reactions with the adsorbed water on the aramid coating. He has not rejected the possibility that the amide functionality of the aramid may play a more significant role at high temperatures. Using photoacoustic FTIR spectroscopy, Chatzi [69] et al. have determined that 30% of the N-H groups in Kevlar 49 fibers may be accessible for possible reactions, but the other 70% are sterically inaccessible.

#### 3. Electrostatic Attractions

Electrostatic attraction can result from the transfer of electrons across the interface, which creates positive and negative charges that attract each other. Electrostatic interactions are usually significant in metal-polymer and fine particle adhesion, but for the polymers at close distances the electrostatic forces are usually small compared to other types of interactions. Inverse gas chromatography studies by Chappell [70], have indicated that there is ~ 62% increase in the dispersive component of *Kevlar 49* surface free energy when the anti-static coating of the fibers is extracted. In the absence of perturbation from other types of interactions, the electrostatic interactions could become significant at the aramid-epoxy interface.

## 4. Polymer Interdiffusion

The contribution of interdiffusion in polymer-polymer adhesion has long been recognized [71]. The extent of diffusion of one polymer phase into another phase depends on their mutual molecular affinities. For aramid-epoxy adhesion, polymer interdiffusion is not possible, but macroscopic diffusion of the liquid epoxy polymers

into the fiber skin and between or within fibrils is possible.

Macrostructural properties of the adhering phases have pronounced effects on the bond strength of their interface. Mechanisms of adhesion are influenced by bulk and surface properties such as mechanical interactions, wetting, and weak boundary layers. These properties do not directly create interfacial bonding, but they can enhance or weaken any of the possible adhesion mechanisms.

#### 1. Mechanical Interactions

Mechanical interactions have several origins including surface topography, thermal stresses, and Poisson contraction.

Surface topography of contacting solids is very important to their adhesion. Solid surfaces are generally rough on a microscale. When two solid surfaces are in direct contact, the actual area of molecular contact is limited a to relatively few high points on each surface. A low contact area results in limited interactions and a weak adhesion. In liquid-solid adhesion, for low-viscosity liquids that can conform to the surface of the solid, the increase in the surface area due to the surface roughness improve all adhesion mechanisms. Conversely, when the liquid has high viscosity or high surface tension, it can form bridges over the rough surfaces and create voids. The presence of voids or bubbles at the fiber matrix interface is generally detrimental to good adhesion.

The effects of surface topography can be analyzed in terms of frictional forces. Both adhesion and deformation contribute to the friction. The adhesion contribution is due to rupture of molecular bonds that takes place during friction and involves local motions of order of 1 nm. The deformation contribution is due to mechanical interactions of the two surfaces and involves motions exceeding 1  $\mu$ m. Friction from surface deformations is always present even when there is no

adhesion. For instance, when an inert lubricant is interposed between the two surfaces, the adhesion friction is eliminated, but there are still deformation frictions.

Additional details and discussions on friction are presented by Cherry [72].

Pull-out techniques to determine the interfacial adhesion either explicitly or implicitly include the effects of friction. Piggott et al. [73] have reported on pull-out experiments with carbon and glass fibers. Their results suggest that the normal pressures and coefficients of interfacial friction are more dependent on the state of cure than the type of resin used. Their reported values for the coefficient of friction of carbon fibers vary from 0.42-0.58, with the higher value corresponding to the higher curing temperature. The reported values for aramid fibers [74] vary from 0.41 to 0.46, which suggests the similarity of its surface topography to carbon. The presence of coating on fiber can significantly affect the friction by modifying the surface topography. The comparison of pull-out properties of coated Kevlar fibers by Mai et al. [75] has demonstrated that shearing rate and interfacial viscosity can significantly affect the interfacial friction of the coated fibers.

Reedy [76] has reported on a finite element analysis of stress concentrations at the *Kevlar*-epoxy interface. Comparing computed frictional stresses with the experimental data, Reedy has suggested that for *Kevlar 49* fiber the friction due to deformation has a magnitude of roughly 50% of that due to adhesion. Reedy has also suggested that when debonding occurs, the results of a linear elastic, perfectly bonded fiber-matrix model are no longer applicable.

Shih et al. [77] have presented a theoretical model to describe the effects of the interface on the tensile strength of unidirectional composites. Their model suggests that for an interface strong in adhesive interactions, an increase in bonding has only a marginal effect on the tensile strength of the composite, but for an interface with low friction an increase in adhesive would significantly enhance the tensile strength.

Thermal stresses are caused by dimensional shrinkage of the resin around the fiber. Cooling, solvent removal, and chemical reactions can cause shrinkage. Thermal stresses can increase surface contact and enhance frictional interactions, but they can also cause elastic strains, which upon debonding, act as a locus of failure. For composites, the thermal stresses are mainly due to the difference in the thermal expansion properties of the fibers and the matrix. Anisotropic aramid and carbon fibers have different thermal expansion coefficients in their axial and radial directions. During cool-down from high curing temperatures, the mismatch between the matrix and fiber shrinkage can result in radial and axial stresses. Nairn et al. [78] have discussed the effects of thermal stresses on Kevlar and carbon composites made with epoxies, amorphous thermoplastics, and semi-crystalline thermoplastics. They suggest that generally, any matrix-dependent composite property is affected by the thermal stresses.

Rojstaczer et al. [79] have reported on the thermal expansion properties of aramid fibers. For Kevlar 49 fibers, they have reported an axial thermal expansion coefficient of -5.7 ppm/°C, which is different from the -2 ppm/°C value reported by the manufacturer [74]. A negative thermal expansion coefficient indicates shrinkage with increasing temperature. The off-axis mechanical properties of the fibers are very difficult to determine and they are often back-calculated from the composite properties. These calculations usually ignore the effects of the fiber-matrix interface on the thermomechanical properties. Based on a matrix thermal expansion of 65 ppm/°C and a Poisson's ratio of 0.35 for both matrix and fibers, Rojstaczer et al. have reported a value of 66.3 ppm/°C for the radial coefficient of thermal expansion of Kevlar.

For carbon fibers, the reported thermal expansion coefficients are -0.1 to -0.5 / ppm/°C for axial and 7 to 12 ppm/°C for the radial expansions [80]. We can infer from the values of the thermal expansion coefficients that along the radial directions,

the thermal shrinkage mismatch between fiber and matrix is much larger for carbon fibers than for aramid fibers. Comparing carbon and aramid fibers, Penn et al. [81] have suggested the lower level of thermal stresses in aramid composites as an important reason for their relatively weaker interfacial adhesion.

Poisson's ratio differences between fibers and matrix can result in conditions similar to thermal stresses. When a fiber has a lower axial Poisson's ratio than the matrix, upon application of axial tension to the composite the matrix shrinks to a greater extent than the fiber, resulting in radial compressive strains referred to as "Poisson contraction". This compressive load can increase the interfacial surface contacts and bonding. Conversely, upon compression, the Poisson contraction can contribute to the debonding of the fiber matrix.

Axial Poisson's ratio of the polyaramid fibers has been back-calculated from their composite properties [82] and is determined to be the close to neat resin values (0.33 to 0.35). Composite measurements do not yield accurate determination of fiber Poisson's ratio. Direct measurement of the fiber Poisson's ratio are not reported in literature. For carbon fibers, the reported values of axial Poisson's ratios is 0.22 to 0.25 [82]. The mismatch of Poisson's ratio between fiber and matrix is much greater for carbon fibers than aramid fibers, suggesting greater normal compressive stresses for the carbon composite under tension. Drzal [83], in comparing the interfacial behavior of aramid and carbon composite, has suggested that both the lower thermal and Poisson's ratio mismatch of aramid-epoxy are adversely affecting their adhesion.

#### 2. Wetting

Adequate wetting of the fiber surface by liquid resin is a prerequisite for good bonding. The importance of wetting in adhesion has been dramatically demonstrated by Sharpe [84]. When liquid epoxy was cured on solid polyethylene, the adhesion was low, however, solidification of molten polyethylene on the cured epoxy produced a much stronger adhesion. In the first case, the liquid epoxy with high surface tension did not wet the solid polyethylene with low surface tension; but in the second case, liquid polyethylene with low surface tension could spread over high surface tension solid epoxy.

Using contact angle analysis, Penn et al. [81] have determined that the surface energies of carbon and aramid fibers are very similar. Li et al. [85] have studied the wettability of carbon and aramid fibers by both the Wihelmy and the solidification front techniques. Wihelmy technique yielded 42.4 mN/m and 43.7 mN/m values for carbon and aramid fibers surface energies, respectively. Solidification front measurement resulted in 41.8 mN/m and 46.4 mN/m for carbon and aramid fibers, respectively. A report by Wesson et al. [86] has shown that surface energies of aramid fibers and liquid DGEBA resin are similar. From these results, both carbon and aramid fibers are expected to have similar "good" wetting with liquid epoxies.

#### 3. Weak Boundary Layers

Weak boundary layers refer to surface layers at the interphase with lower cohesive or adhesive properties than their bulk substrates. Weak boundary layers can be due to entrapped gas, contaminants, and structural anomalies of the substrates. They are usually detrimental to adhesion and can prevent the formation of strong adhesion even though extensive interfacial contact might be present.

There are two types of weak boundary layers, adhesive and cohesive. In an adhesive weak boundary layer only the interface is affected and there is little damage in either fiber or matrix, but in a cohesive weak boundary layer, one or both are damaged. In an fiber-matrix adhesive failure there is clean fiber and matrix separation, but in a cohesive failure there is substantial structural damage to either fiber or matrix. Both types of weak boundary layers could coexist, but depending on the mechanical state of stresses, the effect of one can mask the other.

Existence of cohesive weak boundary layers for untreated carbon fibers has been demonstrated by Drzal et al. [44]. Their study has shown that untreated carbon fibers possess a weak structural layer that can not support high shear loads. Surface treatment of the fiber removes the defect layer and substantially improves adhesion.

For aramid fibers, the possibility of cohesive weak boundary layers exists. Examination of Morgan's model of aramid's skin-core morphology indicates that the PPTA monomers are more randomly dispersed on the fiber exterior but are progressively more clustered towards the core. A reduced degree of crystallinity on the skin could result in weaker properties in the surface region. Upon application of shear to the fiber surface, cracks could be generated in the skin region producing an inefficient fiber-matrix load transfer.

There are numerous indications that surface treatments that do not affect the aramid surface morphology are ineffective in improving its epoxy adhesion. Fiber pull-out experiments by Miller et al. [87] do not suggest any difference between bond strength of "as received" and "acetone washed" aramid fibers. As received fibers have a sizing on them which should introduce an adhesive weak boundary layer, yet the fiber-matrix bond strength is unaffected. Penn et al. [61], have applied various coupling agents to promote aramid-epoxy adhesion and have reported no significant changes in the fiber-matrix bond strength. In a more recent study by Penn et al. [88], flexible reactive pendent groups have been covalently attached to the

aramid fiber surface, but no mechanical improvement of interfacial bonding was observed. Penn has attributed this observation to a lack of bonding between the pendent groups and the matrix; however, failure in a cohesive weak boundary layer could be another explanation. Data by Kompaniets *et al.* [29] have demonstrated that for the aramid fibers the fiber tensile strength is the gage length dependent, but for the unidirectional composites the tensile strength is independent of the gage length. This observation suggests a different failure mode for the embedded fibers which experience shear load transfer.

# Theory

#### **Interfacial Shear Characterization**

Single fiber techniques to examine fiber-matrix interaction are inherently less complex than multi-fiber composite techniques. Coupling of various fiber-matrix interactions in a composite, complicates the examination of it fiber-matrix interface. In this study, a single fiber testing method has been utilized. The technique involves embedding a single fiber in a resin matrix tensile dogbone coupon. The sample is subjected to a tensile load and the transfer of the load through shear at the interface causes fiber fragmentation. The fiber fragmentation process continues until the remaining fragments are too small to transfer enough load to cause another fiber fracture. This final length of fiber is twice a dimensional limit called the *critical length* ( $l_c$ ). Critical length is characteristic of the level of fiber-matrix adhesion as well as the fiber and matrix properties. For a system consisting of a fiber fragment surrounded by an unbounded matrix, a relation between ( $l_c$ ) and interfacial shear strength ( $\tau_u$ ) was first demonstrated by Kelly and Tyson [89]:

$$\overline{\tau}_{u} = \frac{\sigma_{uf}}{2} (\frac{R}{l_{c}}) \tag{1}$$

where  $\sigma_{uf}$  is the fiber tensile strength and R is the fiber radius.

For this system, load transfer to the fiber takes place by shear forces, therefore,  $\overline{\tau}_{u}$  by equation (1) provides a good characterization of the shear strength of the interface. The value of  $\overline{\tau}_{u}$  obtained by equation (1) is the average shear over the fragment.

The shear force at the fiber-matrix interface is the combined result of all the stresses acting at the interface, however, equation (1) does not explicitly specify these forces. To analyze the fiber-matrix interaction a more rigorous model is required. An analytical model of the three-dimensional stress distribution around an isolated fiber fragment has been proposed by Whitney *et al.* [1]. Whitney's model proposes an approximate solution using linear elasticity equations. The main assumptions of the Whitney's model are:

- a) The system is axisymmetric.
- b) Both fiber and matrix undergo elastic deformations.
- c) Fiber is transversely isotropic.
- d) Fiber and matrix strains match at their interface, i.e. perfect bonding.

Complete solutions of Whitney's model are presented in Appendix A, but of particular concerns to this study are the shear  $(\tau_{xr})$  and normal stresses  $(\sigma_r)$  produced at the interface. The interfacial shear and the normal stresses are given by following equations:

$$\tau_{xr}(\overline{x},R) = 4.75 \phi A_1 \varepsilon_0 \overline{x} e^{-4.75\overline{x}}$$
 (2)

$$\sigma_r(\overline{x},R) = \left(A_2 - \phi^2 A_1 \left(1 - 4.75\overline{x}\right) e^{-4.75\overline{x}}\right) \varepsilon_0 \tag{3}$$

where  $\bar{x} = \frac{x}{l_c}$  is a dimensionless length along the fiber axis and  $\varepsilon_0$  is the far field axial strain. Whitney has described  $\varepsilon_0$  as the strain at the onset of observed fiber breakage. Since the testing jig is not very accurate for strain measurements, we

propose another definition:

$$\varepsilon_0 = \varepsilon_{uf} - \alpha_m \Delta T \tag{4}$$

where  $\varepsilon_{uf}$  is fracture strain of the fiber,  $\alpha_m$  is thermal expansion coefficient of the matrix, and  $\Delta T$  is temperature difference between ambient temperature (25°C) and curing temperature. This definition should be close to actual strain at the critical length. Other material property constants  $\phi$ ,  $A_1$ ,  $A_2$ , and  $K_f$  are define by:

$$\phi = \left(\frac{G_m}{E_{1f} - 4v_{12f}G_m}\right)^{\frac{1}{2}} \tag{5}$$

$$A_1 = E_{1f}(1 - \frac{\overline{\varepsilon}_{1f}}{\varepsilon_0}) + \frac{4K_f G_m v_{12f}}{K_f + G_m}$$

$$\times \left[ \mathbf{v}_{12f} - \mathbf{v}_m + \frac{(1 + \mathbf{v}_m) \,\overline{\varepsilon}_m - \overline{\varepsilon}_{2f} - \mathbf{v}_{12f} \overline{\varepsilon}_{1f}}{\varepsilon_0} \right] \tag{6}$$

$$K_{f} = \frac{E_{m}}{2\left[2 - \frac{E_{2f}}{2G_{2f}} - \frac{2v_{2f}E_{2f}}{E_{1f}}\right]}$$
(7)

$$A_2 = \frac{2 K_f G_m}{K_f + G_m} \left[ v_{12f} - v_m + \frac{(1 + v_m)\overline{\varepsilon}_m - \overline{\varepsilon}_{2f} - v_{12f} \overline{\varepsilon}_{1f}}{\varepsilon_0} \right]$$
(8)

Whitney has defined the critical length  $l_c$  such that 95% of the applied axial load is transferred to the fragment. The model permits the calculation of the critical length:

$$l_c = \frac{2.375R}{\Phi} \tag{9}$$

which depends explicitly on fiber and matrix material properties, but not on temperature.

Average values of shear and normal stresses are obtained by integrating equations (2) and (3) with respect to  $\overline{x}$  and then dividing by the fragment length *i.e.* 

$$\overline{\tau}_{xr} = \frac{\int_{0}^{\overline{x}} \tau_{xr}(\overline{x},R) d\overline{x}}{\overline{x}}$$
 (10)

$$\overline{\sigma}_{r} = \frac{\int_{0}^{\overline{x}} \sigma_{r}(\overline{x}, R) \ d\overline{x}}{\overline{x}}$$
 (11)

After some manipulation the following results are obtained

$$\overline{\tau}_{xr} = \frac{\phi A_1 \varepsilon_0 \left( 1 - e^{-4.75\overline{x}} \left( 4.75\overline{x} + 1 \right) \right)}{4.75 \ \overline{x}} \tag{12}$$

$$\overline{\sigma}_r = (A_2 - A_1 \phi^2 e^{-4.75\overline{x}}) \varepsilon_0$$
 (13)

The theoretical average values are evaluated at at  $\overline{x} = 1$  resulting:

$$\tau_{rr}(theo) \approx 0.200 \,\phi \,A_1 \,\varepsilon_0 \tag{14}$$

$$\overline{\sigma}_r(theo) \approx (A_2 - 0.00865 A_1 \phi^2) \varepsilon_0 \tag{15}$$

# **Experimental**

Aramid fibers utilized in this study were *Kevlar 49* supplied by *E.I. du Pont* (lot # 123481, 7200 denier). The fibers were supplied with a sizing. To eliminate possible interferences by fiber sizing, the fibers were washed by absolute ethanol. The washing procedure involved the following steps:

- Removal of the exposed surface layer of the fibers from the spool and a careful selection of a ~ 10 inch fiber tow.
- 2) Three successive washes in absolute ethanol with six hours soaks between each wash.
- 3) Two hours drying of the fibers in a vented oven at 125°C.
- 4) Storage of the tow in clean aluminum foils inside a dedicated desiccation chamber.

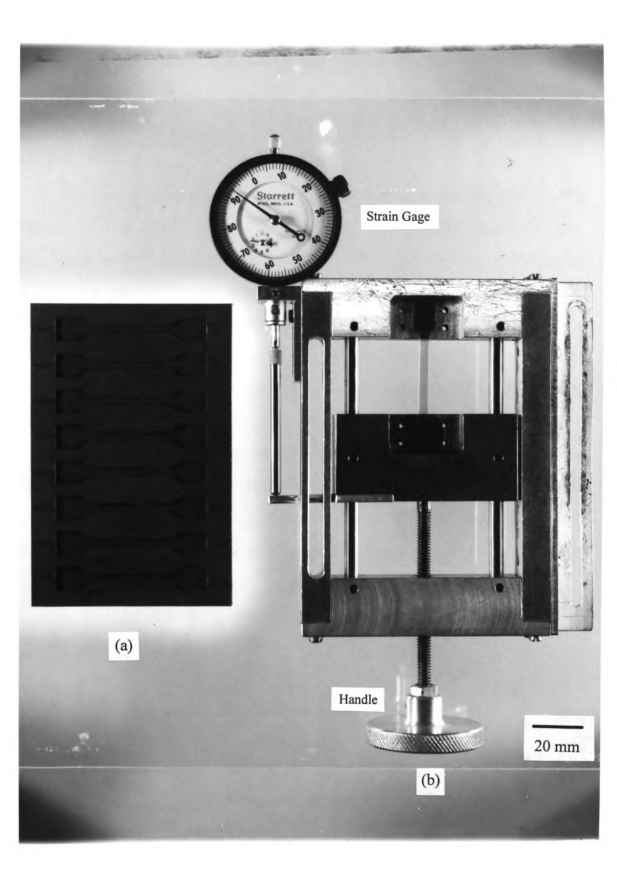
Carbon fibers in this study were AS-4 fiber, supplied by Hercules (lot # 708-4C, 12000 denier). These carbon fibers had no sizing and did not require any washing. They were carefully selected and stored in clean aluminum foils.

This resin is a Diglycidyl Ether of Bisphenol A (DGEBA) epoxy. The curing agents for this study were DiEthyleneTriAmine (DETA) and a mixture of two curing agents M-PhenyleneDiAmine (MPDA) and DiEthylTolueneDiAmine (DETDA). The D.E.R.331/DETA system contained a 11.0/100 mass ratio of curing agent to epoxy. The mixture was degassed in a vacuum oven for 15 minutes at -29 in.Hg (gauge pressure). DETA is highly reactive and its epoxy mixture was degassed only at room temperature to avoid gelling. For D.E.R.331/MPDA/DETDA system, a 7.25/100 mass ratio of MPDA and a 11.75/100 mass ratio of DETDA were combined; this system is referred as (50/50) mixture. The (50/50) mixture was degassed in a vacuum oven at 75°C for 5 minutes at -29 in.Hg to reduce the viscosity of the solution as well as removing entrapped bubbles.

Characterization of the interfacial adhesion was obtained by a critical length measurement technique. The sample was a cured resin dogbone with a single fiber embedded along its center. For the fabrication of the dogbone specimen, a single fiber was carefully hand separated from a tow. The fiber was then mounted in a silicone mold and held in place with a small amount of rubber cement. The mold was left exposed to air for 30 minutes permitting the cement to dry. Subsequently, the mold was placed inside a ventilating oven at 150°C for 1 hour to allow the fibers to desorbe moisture gained during the air exposure. An epoxy resin was then poured into the mold and the fibers were slightly pulled to straighten them. The mold was placed in an oven and the appropriate curing schedules were executed.

A cured dogbone sample was subjected to a tensile load using a tensile testing jig (Figure 9). The load transfer to the fiber through shear at the interface causes the fiber to fragment. The fiber fragmentation process was continued until the fragments reached their critical length  $(l_c)$ . The resin matrix was transparent and the fragmentation process was monitored under an optical microscope at 150X

Figure 9 - A sample mold and the tensile jig for the critical length technique.



magnification. For the carbon fibers the critical lengths were directly measured using a motorized stage with a displacement readout. For aramid fibers, the failure process was by fibrillation and did not have well defined edges. The average critical lengths of the aramid fibers were obtained by counting number of failed regions within a 22 mm fiber length.

Four ranges of curing temperatures ( $T_c$ ) were selected for this study, 25°C, 75°C, 125°C, and 175°C. For the 25°C and 75°C curing temperatures, the DETA curing agent was chosen. DETA is one of the most reactive amine curing agents available, however, at low curing temperatures its epoxy system was still too brittle for the critical length testing. Subsequent post-curing of the DETA systems was required to increase its fracture strain. The post-curing time and temperatures were determined by the glass transition ( $T_g$ ) of the matrix. During the post-cure, the oven temperature was maintained below the  $T_g$  of the matrix. This was to avoid building up thermal stresses. At each post-curing temperature, initially the  $T_g$  was only a few degrees above the oven temperature. After a certain time the glass transition temperature was increased allowing the oven temperature to be raised in steps of 10°C. For the DETA systems, the following curing schedules were selected:

25°C for 48 hours, followed by 4 hours post-curing at 40°C, 50°C, 60°C, 70°C, and 80°C.

75°C for 8 hours, followed by 4 hours post-curing at 85°C.

For 125°C and 175°C curing temperatures, the mixture of MPDA/DETDA (50/50) curing agents was utilized. This system required no post-curing and the following curing schedules were selected:

125°C for 24 hours

175°C, for 3 hours

Thermal expansion and glass transition of the matrix were determined by a du Pont thermal mechanical analyzer (TMA model 943). A 18×4×4 mm sample mold was used to ensure consistent sample geometry. Appendix C includes TMA plots for the thermal expansions and glass transitions of the resin systems. Initial curing times were estimated by differential scanning calorimetry (DSC) performed at isothermal temperatures.

The elastic modulus of the epoxy matrices at the ambient temperatures were determined by a dynamic mechanical analyzer (DMA), ran isothermally at 1 Hz fixed frequency for 5 minutes. To obtain reproducibility in the results, five samples for each curing temperature were tested.

Direct observation of fiber-matrix interface was obtained by transmission electron microscopy (TEM). Ultrathin sections of fiber embedded matrix were microtomed using a diamond knife. The microtoming technique is described in details in appendix D. The sections were examined with a JEOL CX100 TEM with magnifications up to  $320,000\times$ . Some sections were stained with  $OsO_4$  to enhance some particular features.

# **Results and Discussion**

#### Thermal Stresses

Cooling of a composite from oven temperature to ambient temperatures results in thermal shrinkage of the fiber and the matrix. To examine effects of thermal stresses on fiber-matrix adhesion, samples of epoxy dogbones were cured at ambient (nominally 25°C), 75°C, 125°C, and 175°C curing temperatures. Figure 10 illustrates the TMA results for the thermal expansion of these epoxy systems which corresponds to  $70 \pm 6$  ppm/°C thermal expansion coefficient. The epoxy system cured at 175°C has the  $T_g \approx 160$ °C and for this system the thermal stresses are expected to initiate from 160°C. The epoxy system cured at the room temperature was subjected to an extensive post-curing which resulted in  $\sim 0.10$  % post-curing shrinkage. The 75°C cured epoxy was also post-cured to increase its fracture strain. Post-curing temperatures were selected so that oven temperatures was always lower than glass transition of the resin. Such a post-curing scheme has minimized the alteration of the initial thermal stresses. Appendix C contains the TMA plots for the thermal expansions of the epoxies and the post-curing schedules for the 75°C and room cured epoxies.

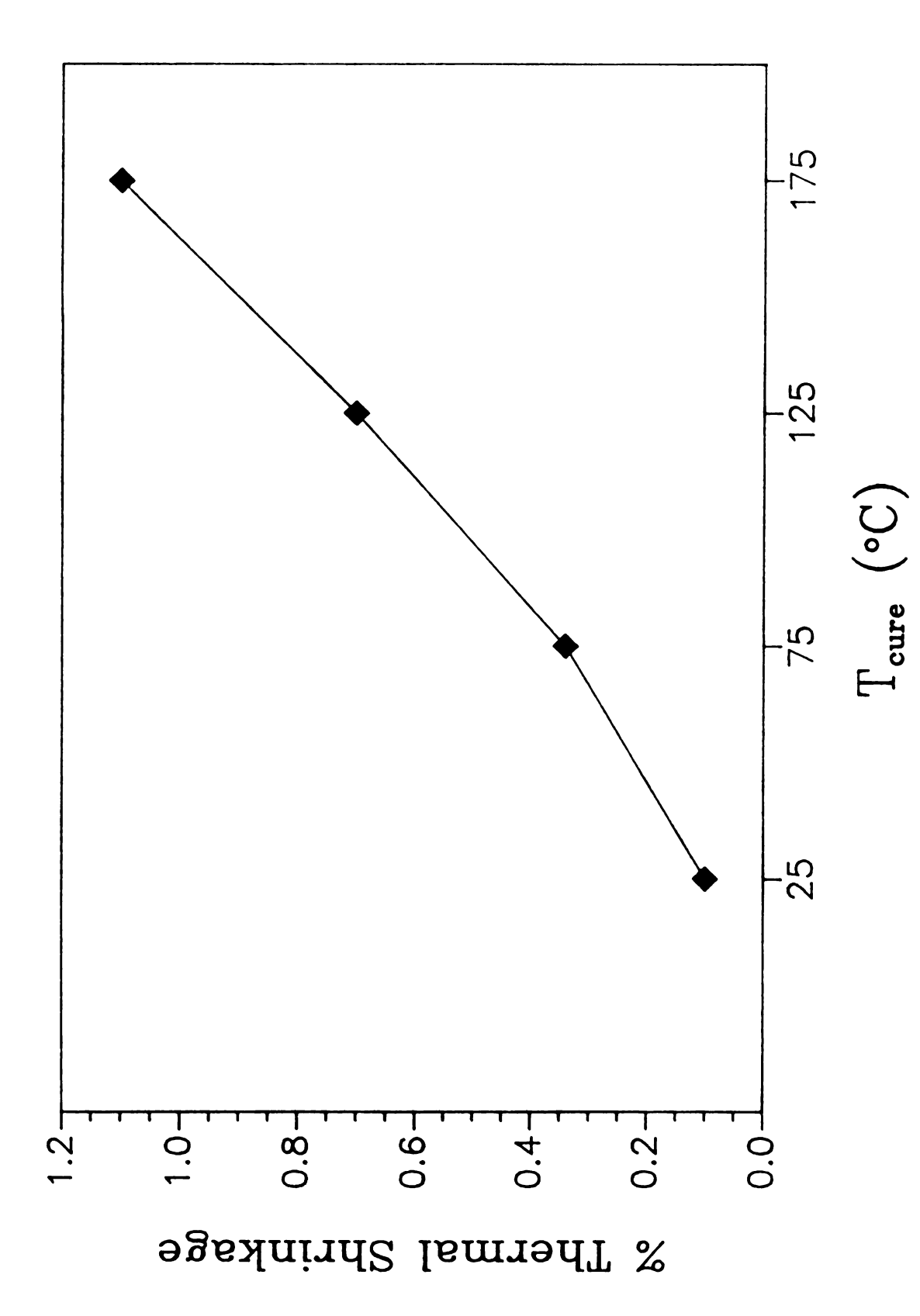


Figure 10 - Plot of % thermal shrinkage of the epoxy matrices cured at different temperatures.

The experimental carbon fiber data has been analyzed by a Weibull model, but a normal distribution has been used for the aramid data. The brittle fracture of the carbon fiber permits the measurement of the individual fragments and with its short critical lengths, a large number of fragments were measured for each sample dogbone. The Weibull model is a two parameter model that is often used to describe unsymmetric failure distributions. The large data population of the carbon samples should provide a good estimation of the Weibull constants, however, the carbon fiber is very flaw sensitive and has a large tensile properties variations which results in large intrinsic variations in the critical length distribution. For the aramid fibers, the individual fragments could not be accurately measured because of the fibrillation that occurs at its failed regions. The average aramid critical lengths were determined by dividing the length of the fiber by the total number of observed failed regions. The experimental aramid critical lengths are much longer than the carbon critical lengths, but the aramid data have relatively small variations. With a smaller aramid data population the Weibull constants can not be accurately estimated so a normal distribution is used instead.

In the following results, the carbon fiber data indicate much larger error bars than the aramid fiber data. The larger carbon data variation is due the intrinsic variation in the carbon fiber tensile properties rather than the experimental variations. For example, 500 and 1000 data populations for the gold coated 125°C cured carbon samples both have similar mean and variations. The mean values of the carbon data populations are very consistant and the large error bars should not prevent us from making valid judgements on the possible correlations.

Experimental interfacial shear strength  $(\tau_u)$  values of untreated aramid-epoxy and carbon-epoxy systems at different curing temperatures are presented in Figure 11. For the examined curing temperatures, the aramid samples exhibit 3.5 to 5 times lower  $\tau_u$  than the carbon samples. The carbon samples indicate increased fiber-

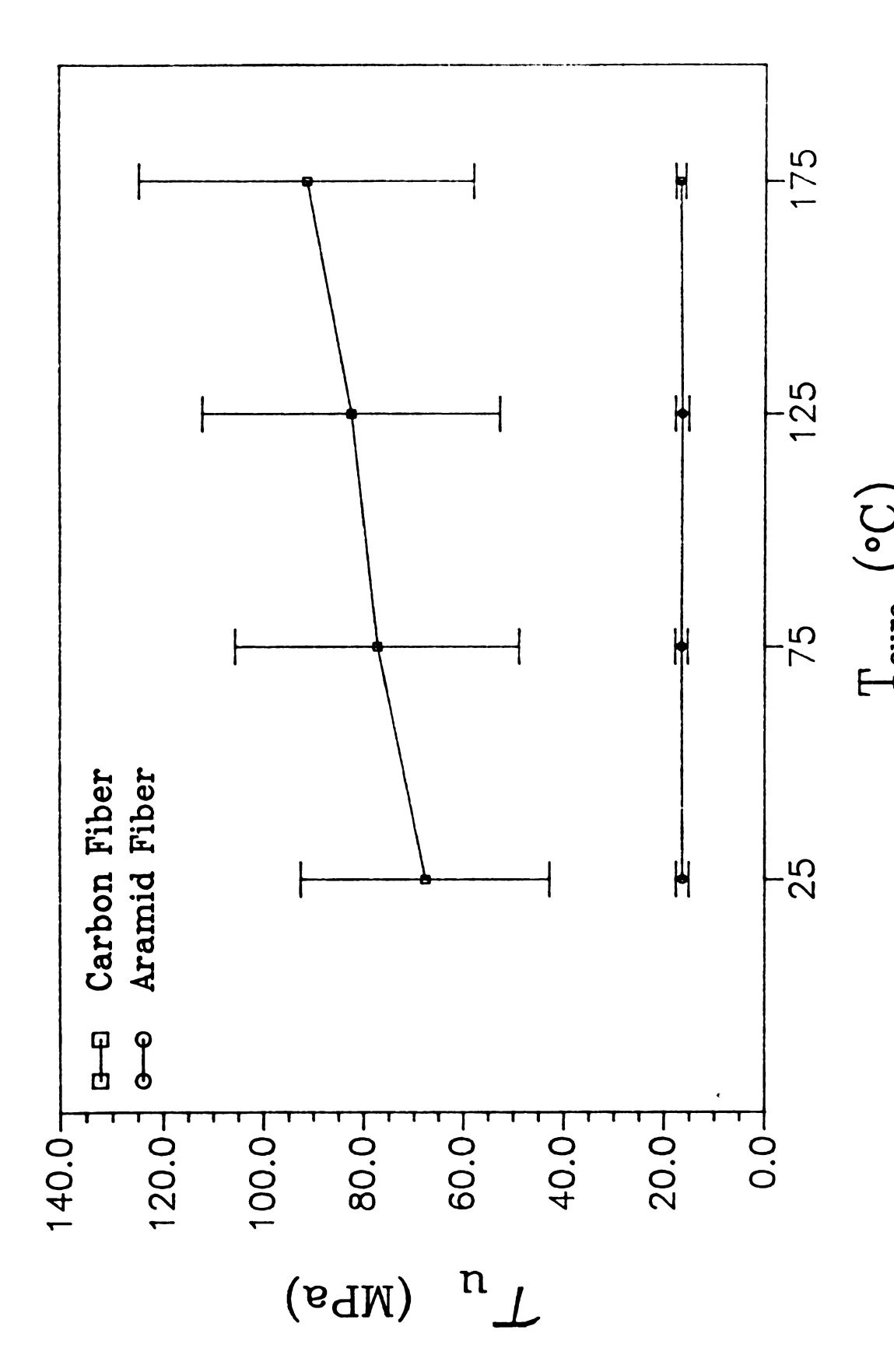


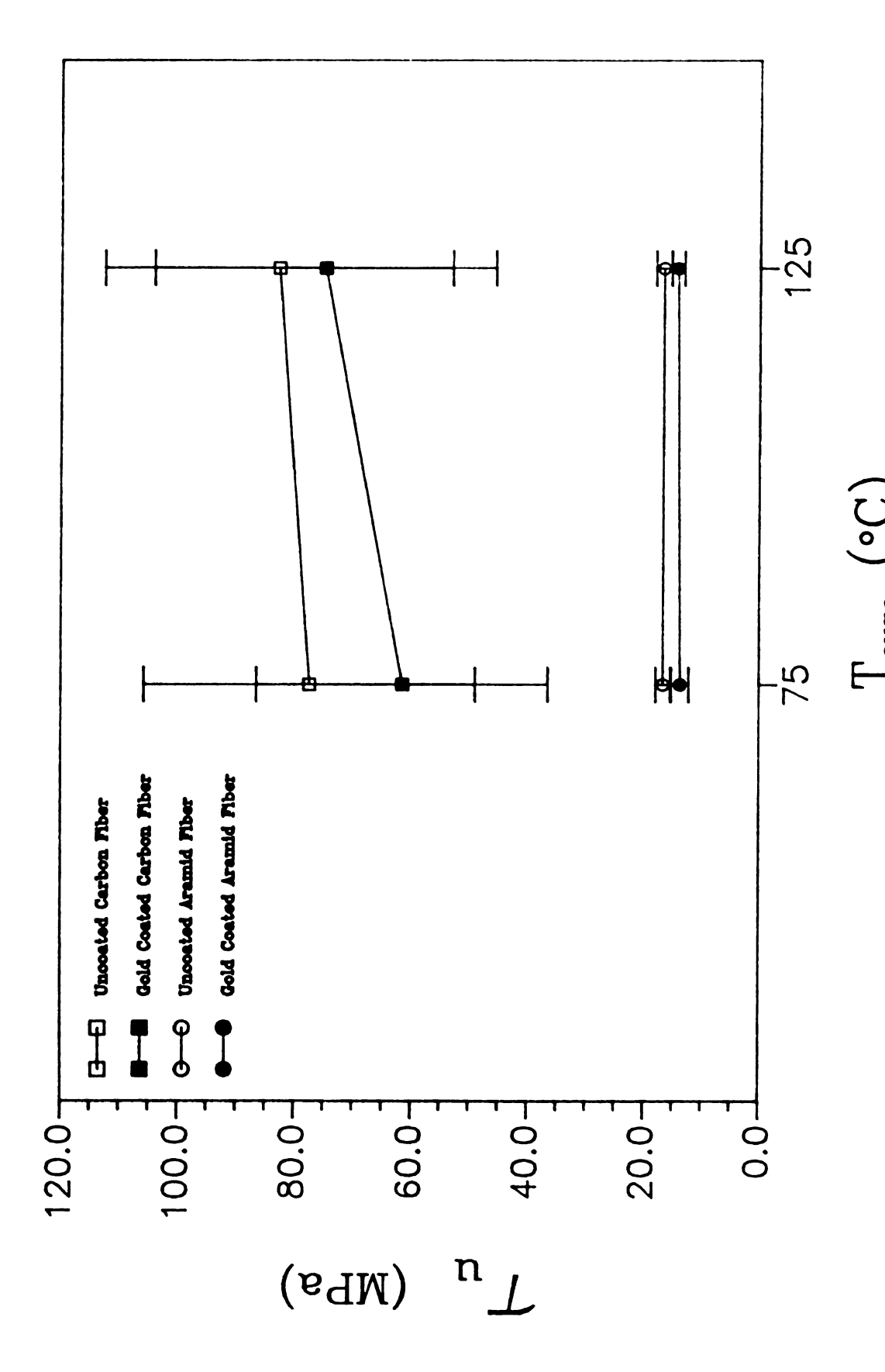
Figure 11 - Plot of experimental interfacial shear strength of untreated carbon and aranid fibers with epoxy matrices cured at different temperatures.

matrix adhesion with increasing curing temperatures, but the aramid samples seems to be unaffected by the curing temperature. During cool down from oven temperature to ambient conditions the isotropic matrix shrinks uniformly, but the orthotropic fiber undergoes longitudinal expansion and radial shrinkage. The overall radial thermal stress at the fiber-matrix interface is due to both radial thermal shrinkage of fiber and matrix and the Poisson contraction resulted from the fiber longitudinal strains. The temperature independence of the aramid-epoxy adhesion can be attributed to the close match between the Poisson's ratio and the radial thermal expansion coefficient of the aramid fiber and the epoxy matrices.

# **Chemical Bonding**

Coating the fibers by an inert material such as gold eliminates all possible covalent bonds at the fiber-matrix interface. The coating also introduces a weak boundary layer, but for relative comparisons the effect of the layer should be constant. Figure 12 demonstrates the effect of the two different epoxy systems on the interfacial shear strengths of gold coated and uncoated fibers. The uncoated carbon samples exhibit smaller changes between the 75°C cured DETA system and 125°C cured MPDA/DETDA system than the corresponding gold coated carbon fibers. For the aramid adhesion no trends with the curing temperature or epoxy system for either coated and uncoated fibers are observed.

At the two curing temperatures, the difference in the gold coated samples should be mainly due to thermal stresses and Poisson contractions. From 125°C to 75°C curing temperatures, the uncoated carbon fibers show a lower reduction in adhesion than the gold coated samples. This observation can be attributed to the compensation of the lower thermal stress at 75°C curing temperature by the greater chemical reactivity of its resin. The DETA curing agent is chemically more active than the MPDA/DETDA curing agents which increases the extent of possible



carbon and aramid samples made with 75°C and 125°C cured epoxy matrices. Figure 12 - Plot of experimental interfacial shear strength of untreated and gold coated

chemical bondings at the fiber-matrix interface. For the aramid fibers, both coated and uncoated fibers exhibit the same levels of adhesion at the two curing temperatures. The relative adhesion reduction for the gold coated aramid samples is less than the corresponding carbon samples. The aramid observations suggests that the difference in the chemical reactivity of the resins does not affects the aramidepoxy adhesion.

#### **Poisson Contraction**

The Poisson contraction refers to the stresses due to the contraction of the matrix when a load is applied to the composite. Figure 13 compares the interfacial shear strength of gold coated, silicone coated, and uncoated aramid and carbon samples made with the room temperature cured epoxy. The carbon samples generally exhibit higher  $\overline{\tau}_{\mu}$  values than the aramid fibers for both coated and uncoated fibers. The room cured matrix has a very low thermal stress and the coated fibers have no covalent chemical bonding at their interface. For the coated fibers the main interfacial interactions present are the Poisson contraction, fiber-matrix wetting, and the effect of the weak boundary layer due to the coating. Both the gold coated and the silicone coated carbon fibers have  $\overline{\tau}_{\mu}$  values two and half times the values of corresponding aramid fibers. Since the coated aramid and carbon fibers have the same surface properties, the higher adhesion of the coated carbon fiber indicates the effect of Poisson contraction. Note that for the uncoated carbon fiber  $\overline{\tau}_{\mu}$  is about four times higher than the uncoated aramid fiber which can be attributed to the effect of the chemical bonding and removal of the coating weak boundary layer.

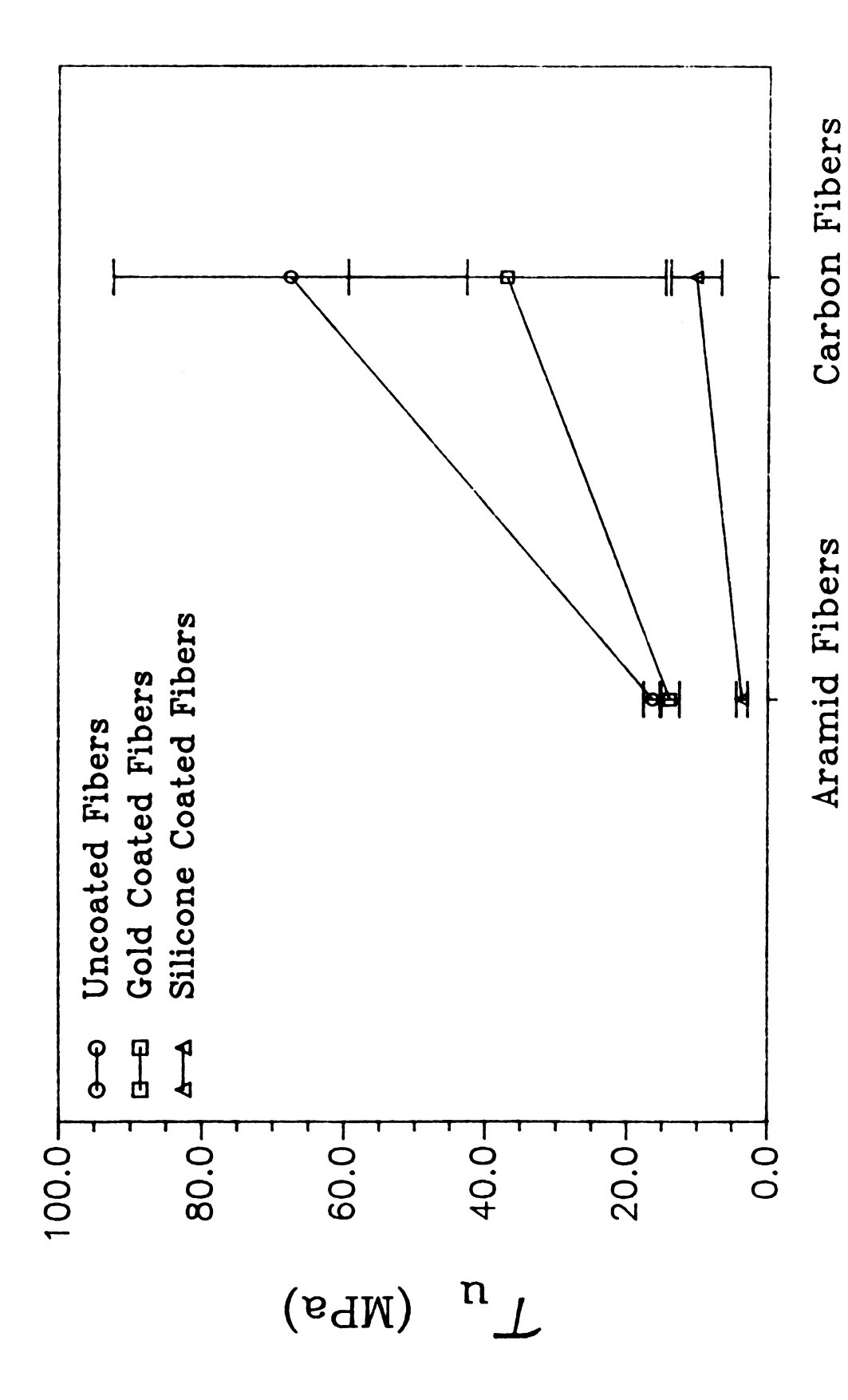


Figure 13 - Plot of experimental interfacial shear strength of untreated, gold coated, and silicone coated carbon and aramid samples made with the room cured epoxy.

## Fiber Wetting

Good wetting of the fiber by the liquid resin increases molecular interactions at the interface, which in turn enhances the load transfer to the fiber. Figure 14 compares the  $\overline{\tau}_u$  values of the coated and uncoated aramid fibers. Gold coated fibers give a ~ 15% reduction in  $\overline{\tau}_u$ , while, silicone coated fibers produce ~ 75% reduction. The metallic gold has a high surface tension, but the silicone is a mold release agent with very poor wetting properties. The drastic reduction of the silicone coated fibers clearly indicates the importance of achieving thermodynamic wetting as a precondition for adhesion.

### **Three Dimensional Stress Model**

The experimental values of the interfacial shear strengths have been determined by equation (1), however, the effects of the thermal stresses and Poisson contractions are not explicitly present in the equation. A three dimensional stress model proposed by Whitney was examined to acquire additional insights to the interfacial interactions. The material properties for fibers are presented in the Tables 1. The Poisson's ratio of 0.35 is assumed for the matrices. The ambient matrix elastic modulus have been determined by DMA and are plotted in Figure 15. The matrix thermal expansions are given in the Figure 10.

For the aramid and the carbon fibers, Figure 16 compares the theoretical critical lengths calculated by equation (9) with the experimental critical lengths for the uncoated fibers. The data indicate that the theoretical results for the carbon fibers are close to the experimental results, but for the aramid fibers there are factors of four differences. Due to model assumptions, the theoretical critical lengths do not show the same temperature trends as the experimental results. The model defines the critical length as the length required to recover 95% of the applied longitudinal stress on the composite and the resulting critical length equation is:

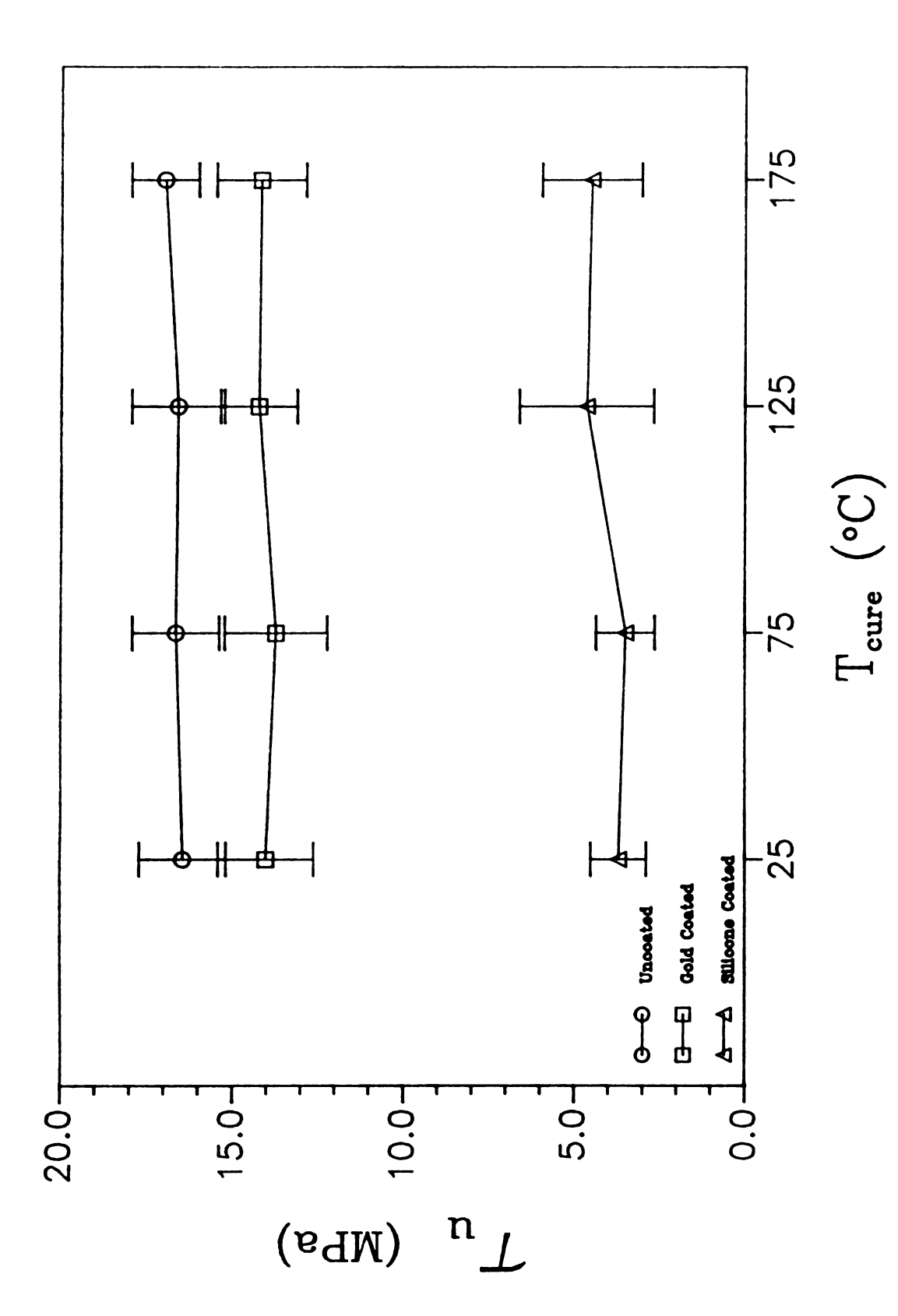


Figure 14 - Plot of experimental interfacial shear strength of untreated, gold coated, and silicone coated aramid made with epoxy matrices cured at different temperatures.

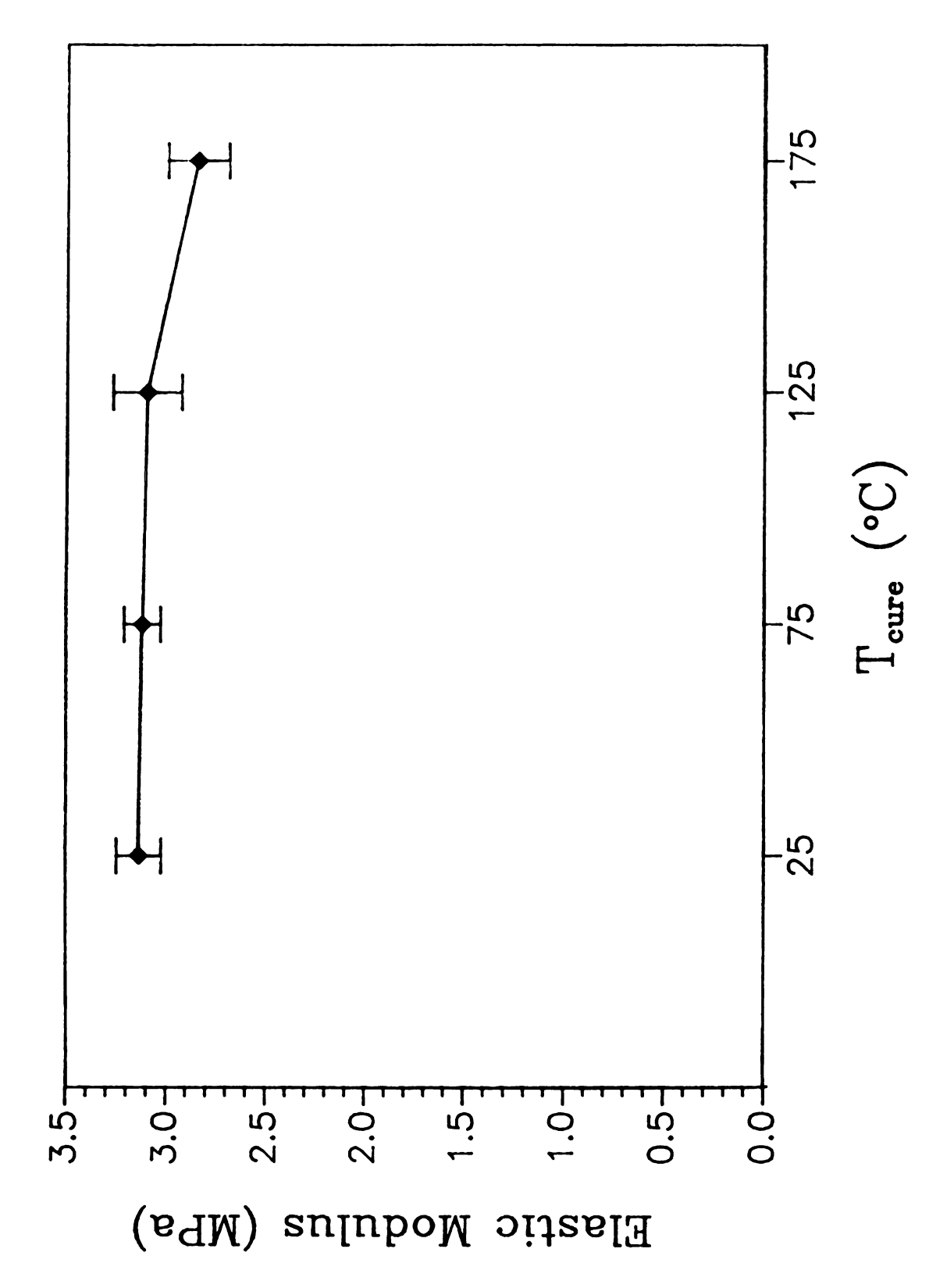


Figure 15 - Plot of elastic modulus of the epoxy matrices cured at different temperatures.

$$l_c = 2.375 R \left[ \frac{G_m}{E_{1f} - 4v_{12f}G_m} \right]^{\frac{1}{2}}$$
 (18)

which does not include any temperature term.

The model permits the evaluation of stress and displacement components. Figure 17 compares the experimental and the theoretical interfacial shear strengths calculated by equations (1) and (14). The experimental and the theoretical  $\overline{\tau}_u$  values for the carbon fiber show much smaller differences than the result for the aramid fiber. For both fibers, the theoretical results indicate increasing  $\overline{\tau}_u$  values for higher curing temperatures, although to a greater extent for the carbon fibers than for the aramid fibers. The model predicts good interfacial shear strength for both types of fibers.

To understand the discrepancies between the experimental and the theoretical results, the assumptions of the model needs to be closely examined. The model assume that both fiber and matrix undergo elastic deformations, however, the fiber fragments or matrix may actually behave nonelastically. Reedy [76] has suggested that when debonding occurs, the results of linear elastic, perfectly bonded fiber-matrix models are no longer applicable. Figures 18 show the optical micrographs of aramid and carbon fiber fragments under bright-field and cross-polarized lights. For the carbon fiber, the fiber-matrix failure is by a combination of interface slippage and matrix cracking, but the fragment and its surrounding matrix should behave elasticly. The carbon fragment shows no longitudinal failures and the cracked matrix may only display inelastic behavior near the crack regions which is only an small portion of the fragment length. Another assumption of the model, the matching strains at the fibermatrix interface may also not be valid for the fibers. Sometimes small gaps between carbon fragments are observed indicating interface slippage. For the aramid fragments it is difficult to assess the interfacial slippage. The low intensity and

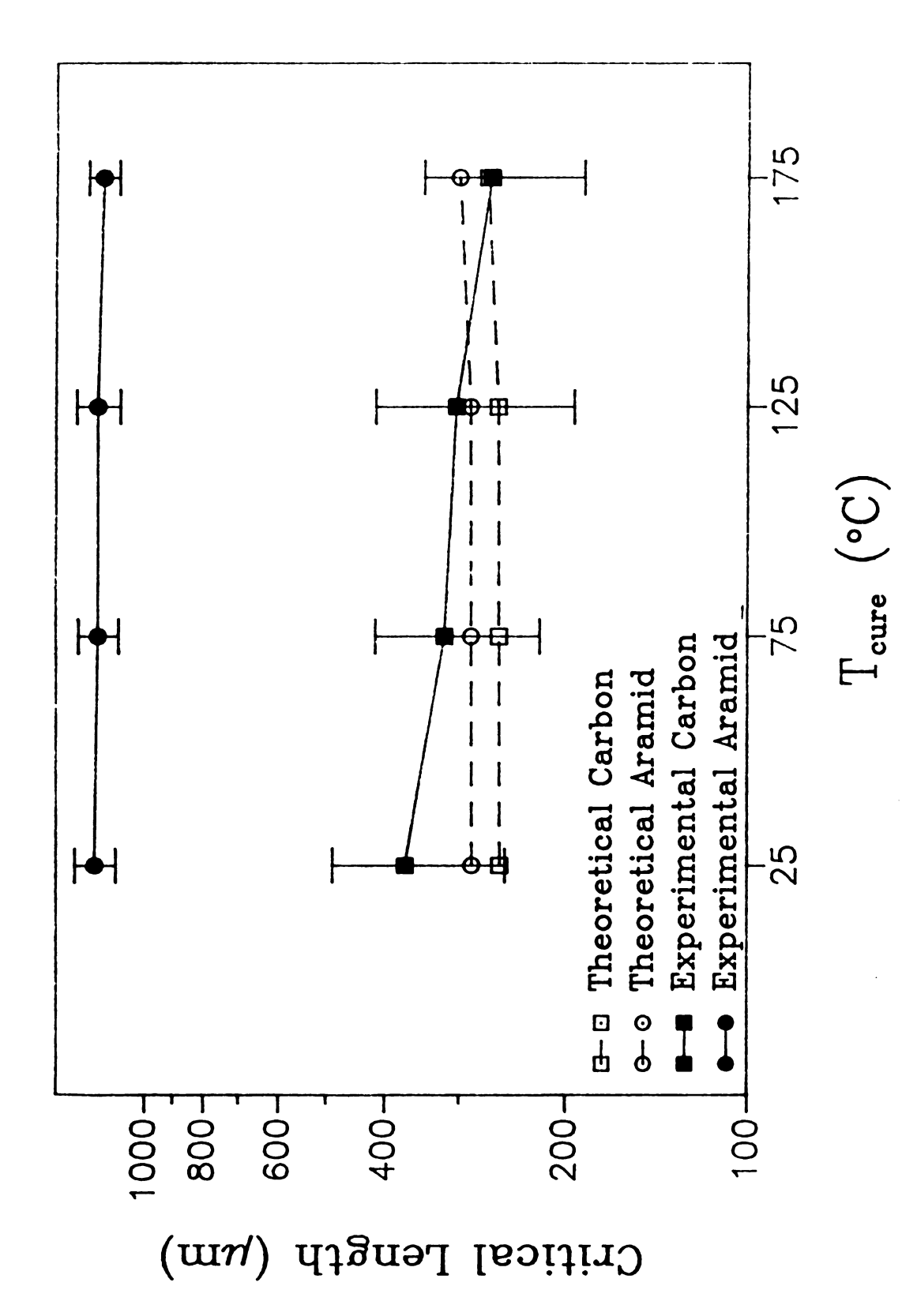
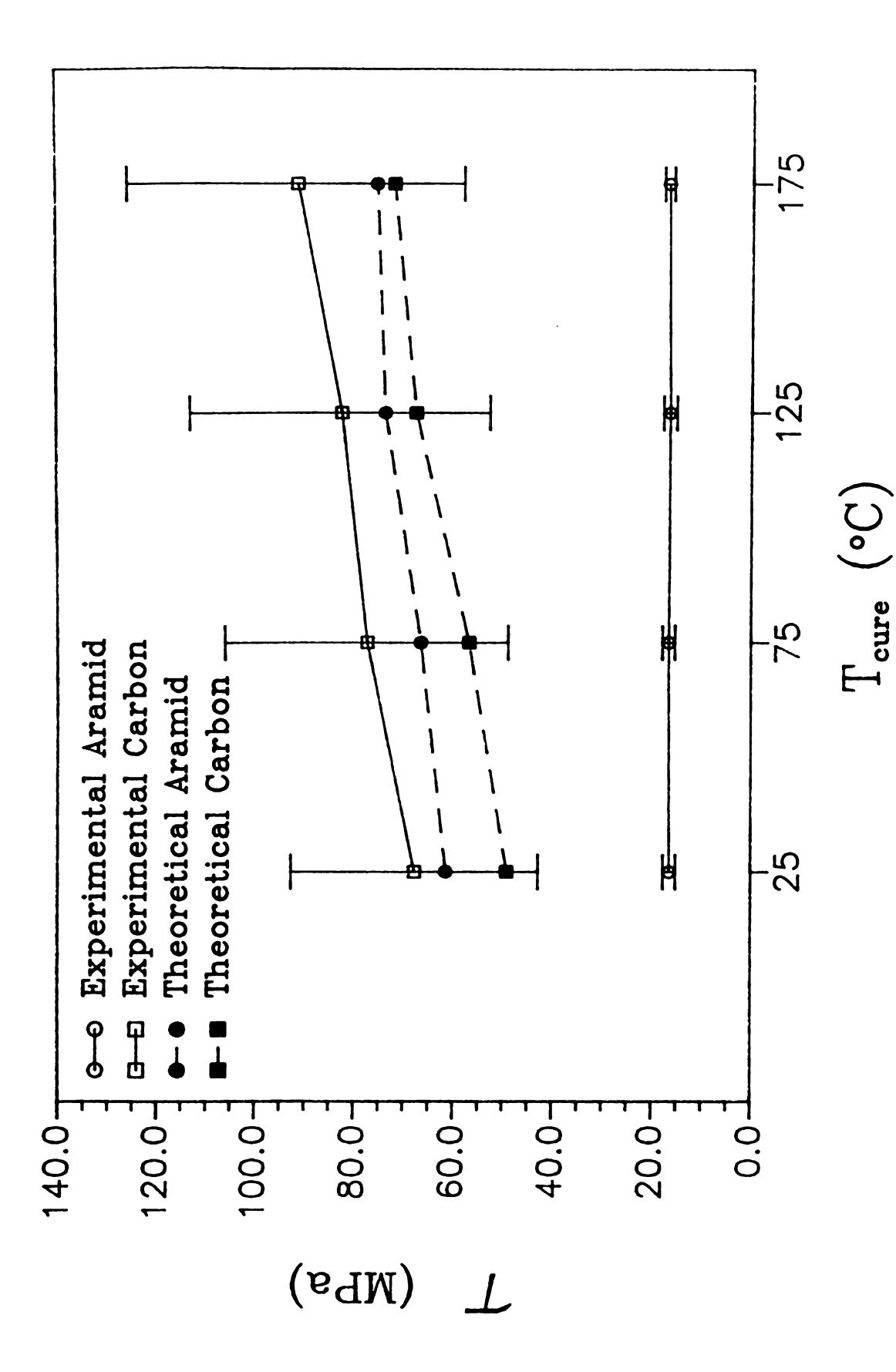


Figure 16 - Plot of theoretical and experimental critical lengths for aramid and carbon fibers with epoxy systems cured at different temperatures.



the critical lengths for aramid and carbon fibers with epoxy matrices cured Figure 17 - Plot of theoretical and experimental average interfacial shear stress over at different temperatures.

dispersed stress fringe patterns of the aramid-epoxy interface may be due to either interface slippage or internal fiber realignments due to surface to bulk fractures. Presence of a strong chemical covalent bond at the fiber-matrix interface should reduce the fiber-matrix slippage. Finally, the critical length equation which does not take into account the effects of thermal stresses may introduce some additional errors in the theoretical results.

The failure of the Whitney's model to reasonably predict the aramid interfacial interactions suggests the severity of the violation of model's assumptions. The inelastic longitudinal failure mode of the aramid fiber may be the principal reason for the model's deficiency. Upon the onset of the longitudinal cracks the fiber no longer behave elastically and in fact a substantial decrease in the fiber modulus are expected. Other fiber properties such as Poisson's ratio or thermal strains may also be altered by the fiber longitudinal fracture. The matrix is expected to maintain an elastic behavior since no matrix crack is observed. The failure of the perfect bonding assumption may also skew the result. Aramid fragment separation has not been observed, but internal fibril slippage is possible. The temperature independence of the critical length equation is not expected to introduce severe errors to the aramid results since the experimental results are also temperature independent.

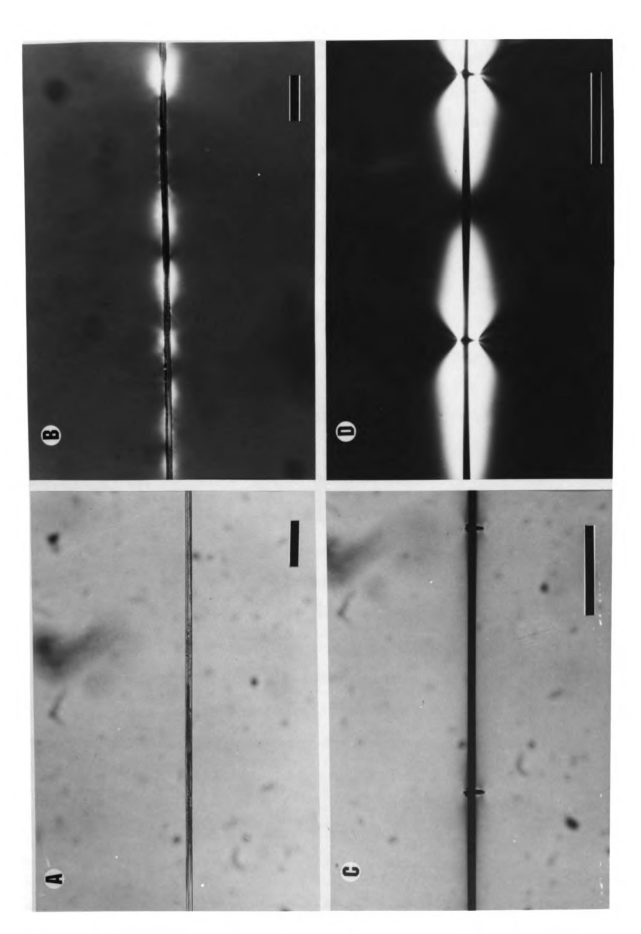
The interfacial radial stress is due to radial thermal strains and Poisson contractions. Since fiber and matrix are in series, these radial strains should be fully transferred despite any possible interfacial slippage. The fiber is embedded in a large matrix environment, thus, the matrix has greater displacements and its properties should dominate the fiber properties. The interfacial radial stress is therefore expected to be much less dependent on the extent of fiber-matrix bonding and moduli of the fiber than other stresses. Equation (15) represents the theoretical average radial stress:

$$\overline{\sigma}_r(theo) \approx (A_2 - 0.00865 A_1 \phi^2) \varepsilon_0 \tag{15}$$

Figure 18 - Optical micrographs of fiber fragments at their critical lengths.

- (A) Kevlar 49 under bright-field light.
- (B) Kevlar 49 under cross-polarized light.
- (C) AS-4 under bright-field light.
- (D) AS-4 under cross-polarized light.

 $bar = 100 \mu$ 



An inspection of the equation suggests that the equation is more dependent on the value of the  $A_2$  constant than the  $A_1$  constant. A numerical examination of the equation (15) shows that for the aramid fiber  $A_1$  term has at most 20% contribution to the  $\overline{\sigma}_r$  value and for the carbon fiber at most 4% contribution to the  $\overline{\sigma}_r$  value. Inspection of constant  $A_2$  reveals that it is mainly determined by the matrix elastic and shear modulus. The matrix modulus are expected to conform reasonably to elastic behavior, therefore, the magnitude of theoretical radial stresses should be approximately valid for both fiber systems.

Figure 19 compares the theoretical average radial stresses for both the aramid and the carbon systems. The carbon systems show three to five times higher radial stress values than the aramid system. The carbon system also shows higher  $\overline{\sigma}_r$  increases with curing temperature than the aramid system. The higher  $\overline{\sigma}_r$  value of the carbon system can be attribute to its higher thermal stresses and Poisson contractions. The temperature trend of the aramid system is mostly due to the Poisson contractions caused by its longitudinal thermal stresses.

The theoretical analysis for the aramid fibers indicates increasing radial stresses with increasing curing temperature, however, the experimental interfacial shear strengths are found to be independent of the curing temperatures. The theoretical interfacial shear stresses are also much greater than the experimental values. These observations suggests that the aramid-epoxy adhesion is substantially limited by a failure process which prevent the interfacial stresses from reaching their theoretical maximums. Altering and improving the aramid-epoxy failure process has the potential of increasing adhesion to levels comparable to carbon-epoxy adhesion.

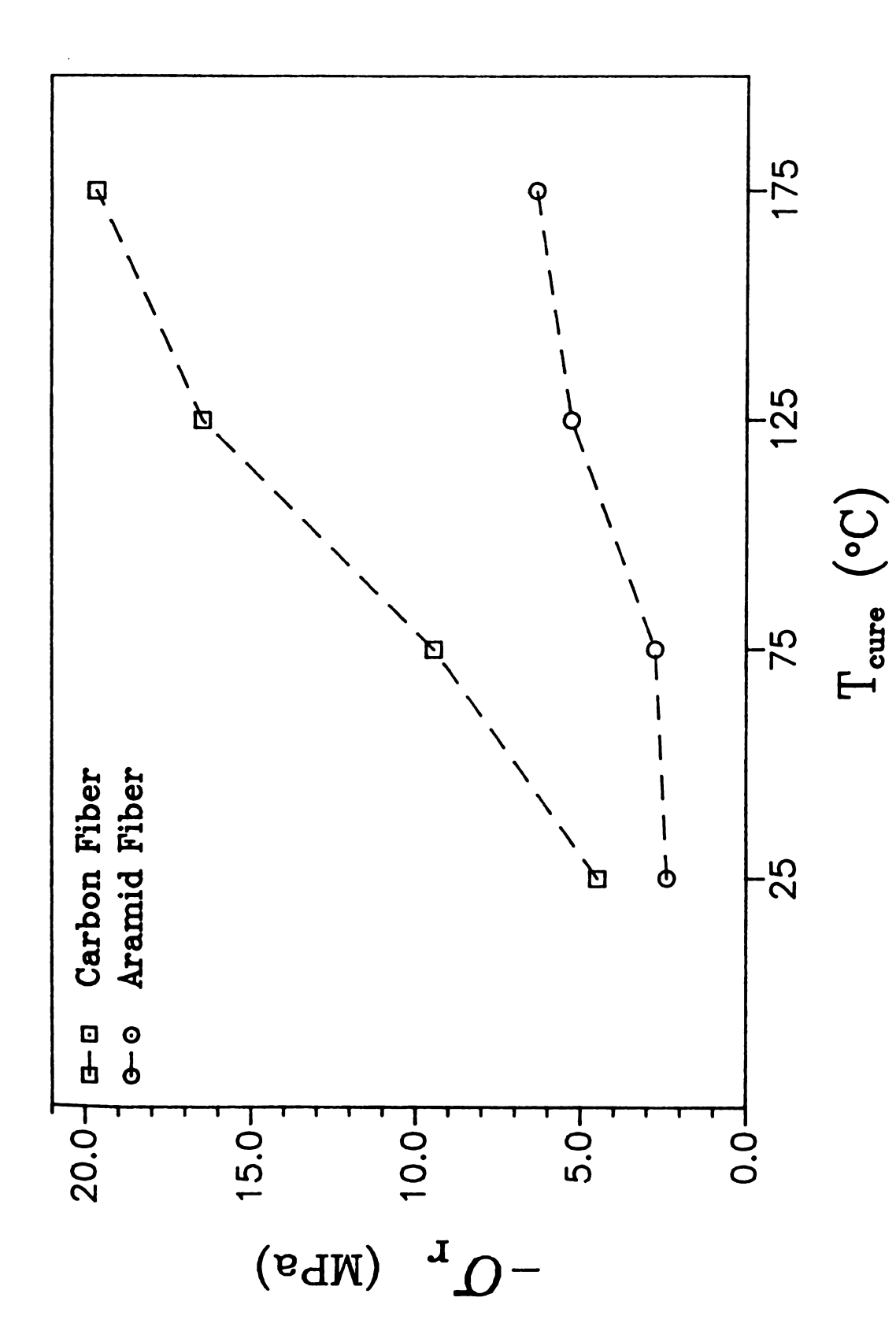


Figure 19 - Plot Theoretical average radial stresses for aramid and carbon fibers with epoxy matrices cured at different temperatures.

#### **Electron Microscopy**

Direct observations of the fiber-matrix interface is possible through transmission electron microscopy (TEM). The technique involves ultrathin sectioning of the composite and high-magnification transmission electron imaging of the fiber-matrix interface. The details of the sectioning technique are described in appendix D. Care must be taken in the interpretation of the images to avoid mistaking the sectioning artifacts for actual fiber-matrix interactions. During sectioning, the cutting knife exerts bending and compression on the sections which can result in fracture, thickness variation, and folding of the fibers at normal to the cutting direction. In the following micrographs, the direction of the sectioning is indicated by an arrow, fiber and matrix are identified by letters F and M respectively, and the designated magnifications are shown by scale bars with better than 10% accuracy.

An ultra-thin section of a aramid-epoxy composite cut parallel to the long axis of the fiber is shown in Figures 20. The aramid fiber ribbons generally show interfacial separations with some fibrils remain attached to the matrix. The aramid ribbons easily separated from the epoxy matrix and it was difficult to find sections where the fiber ribbon was still connected to the matrix. The ribbon shows repeated bands of knife marks along its width.

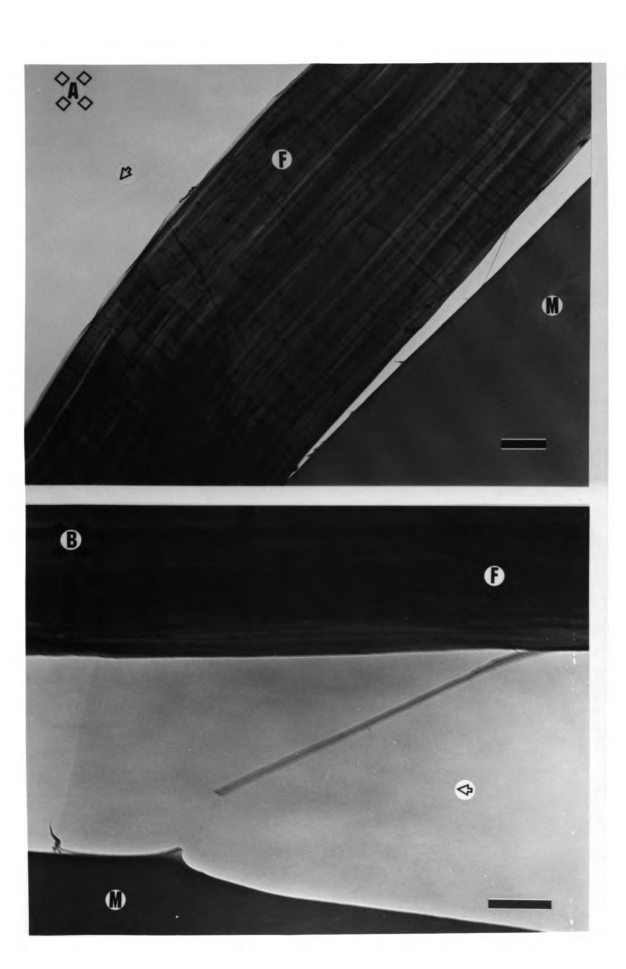
The aramid fiber was also sectioned normal to the fiber longitudinal direction. This sectioning direction exerts both tension and compression loads on the fiber-matrix interface which provides more insight to the fiber-matrix interactions. Figures 21 and 23 to 26 illustrate aramid-epoxy composite sections cut along the fiber radius. Figure 21 illustrates the fibrillation that takes place upon tearing of the fiber. Similar fibrillation are also seen at the aramid-epoxy interface (Figures 23 to 26). Aramid fibers sometimes display a torn skin in the form of helical ribbons as shown in Figure 22; radial cross-sections of such fibers are shown in Figures 23 and 24. The fiber-matrix separation again takes place through the fibrillation of the

aramid fiber. Figure 24 has concentrated on a portion of a skin-torn fiber that is suspected to be the region where the skin was originally located. The section in Figure 24 has been stained with  $OsO_4$  which reacts with the matrix and increases its contrast. A high magnification of this portion, shows some aramid fibrils which are still connected to the matrix. Finally, aramid fibers which have been damaged by the interfacial shear test have been examined. The cross-section of the longitudinal cracks which are the typical form of the aramid fracture can be seen in Figure 25. The longitudinal cracks had propagated to the fiber core dividing the fiber into pieces. Another damaged aramid section is shown in figure 26. A high magnification observation of the interface illustrates the uniformity of the aramid-epoxy interface suggesting a good fiber-matrix surface interactions.

The morphology of the aramid fibers can describe their observed mode of interfacial failure. The aramid fibers are constituted of large polymer macromolecules which only form hydrogen bonding with their adjacent molecules. Such structure tends to initially fail across the weak hydrogen bondings resulting in a failure by fibrillation. When the load transfer is by shear forces, the fiber exterior receives the load and distributes it to the rest of the fiber. For the aramid fibers, it is conceivable that the fiber exterior could be of lower strength and modulus than the fiber core and long critical lengths are required before the shear load is fully transferred to its core. Furthermore, the aramid fiber failure could be initiated by surface cracks which then propagate towards the fiber core.

Figure 20 - TEM micrographs of Kevlar 49 and MPDADETDA epoxy system cured at 175°C. The section is cut parallel to the long fiber axis.

- (A) bar =  $2 \mu m$
- (B) bar = 50 nm



		Fi

Figure 21 - TEM micrographs of Kevlar 49 and room-cured epoxy system.

The section is cut along the fiber radial direction.

- (A) bar =  $1 \mu m$
- (B) bar = 500 nm





Figure 22 - SEM micrographs of a single Kevlar 49 fiber.

- (A) bar =  $10 \mu m$
- (B) bar =  $5 \mu m$

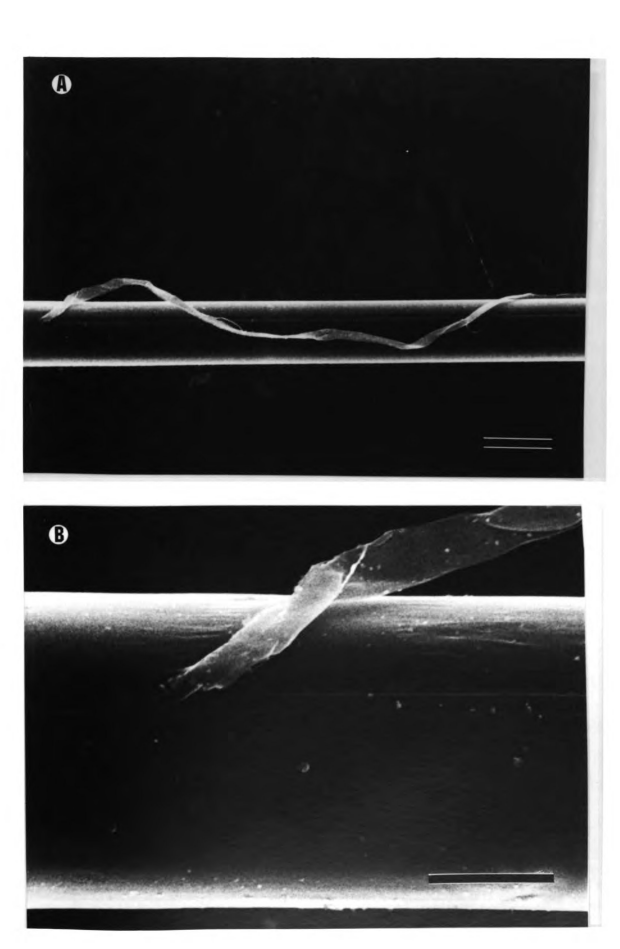
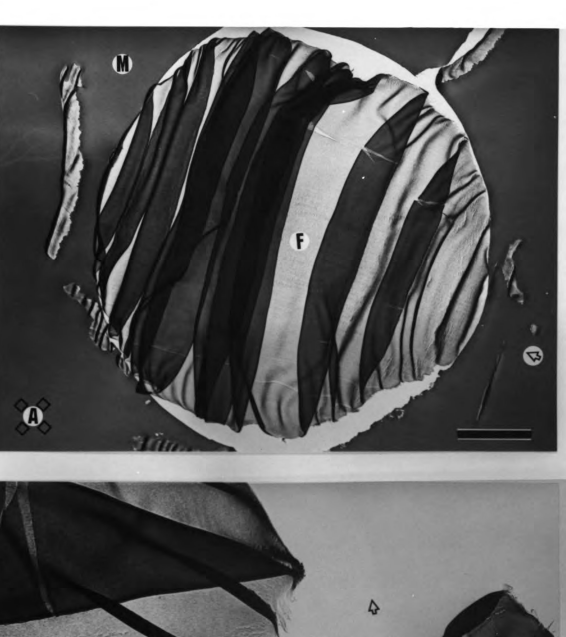


Figure 23 - TEM micrographs of a surface damaged Kevlar 49 and MPDADETDA epoxy system cured at 175°C. The section is cut along the fiber radial direction.

- (A) bar =  $2 \mu m$
- (B) bar = 500 nm



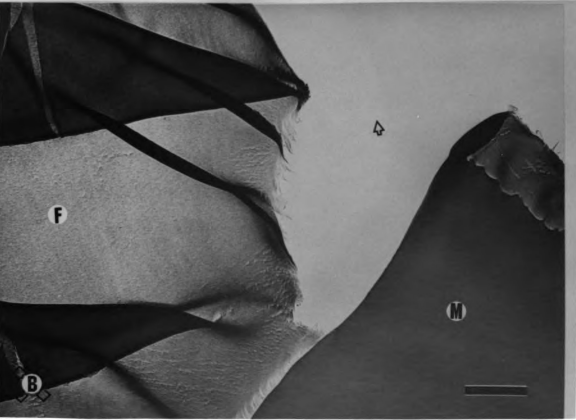


Figure 24 - TEM micrographs of a surface damaged Kevlar 49 and MPDADETDA epoxy system cured at 175°C. The section is stained with  $OsO_4$ . The section is cut along the fiber radial direction.

- (A) bar =  $1 \mu m$
- (B) bar = 100 nm

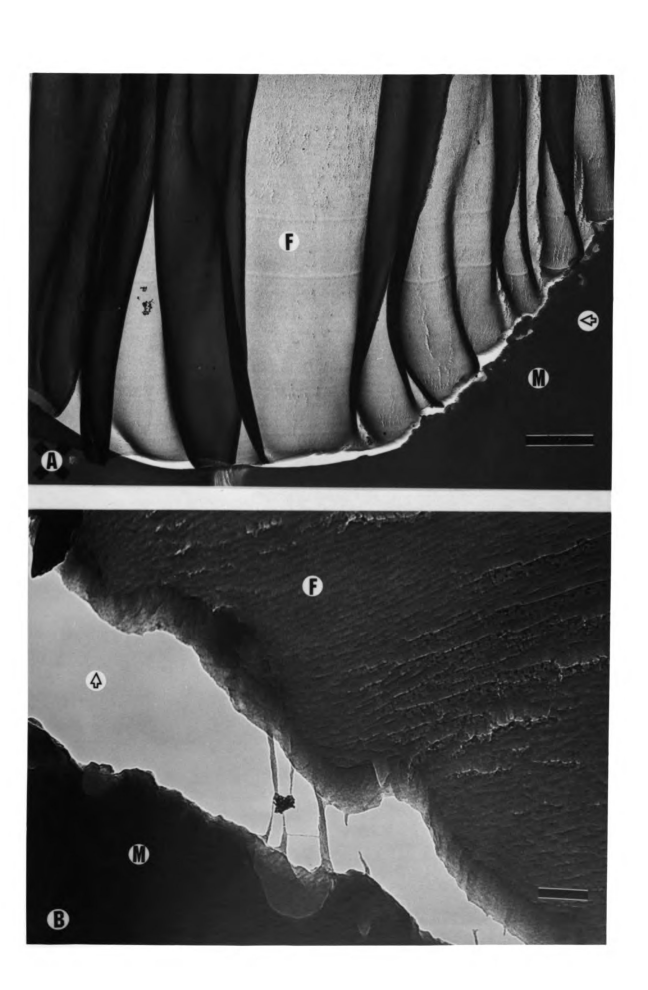


Figure 25 - TEM micrographs of a shear damaged Kevlar 49 and DETA epoxy system cured at 75°C. The section is cut along the fiber radial direction.

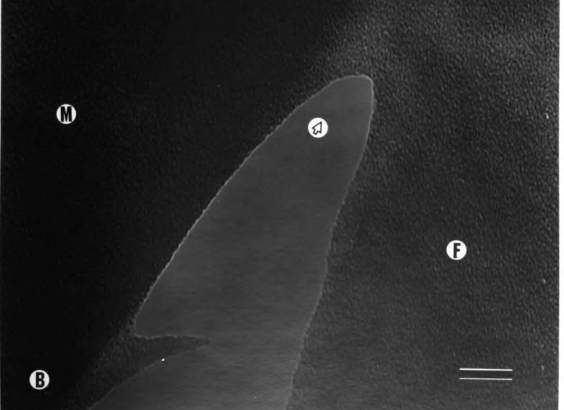
- (A) bar =  $1 \mu m$
- (B) bar = 500 nm



Figure 26 - TEM micrographs of a shear damaged Kevlar 49 and DETA epoxy system cured at 75°C. The section is cut along the fiber radial direction.

- (A) bar = 250 nm
- (B) bar = 25 nm





### **Conclusions & Recommendations**

The results of this study lead to some important conclusions on the aramidepoxy bonding mechanisms. The results also point out the potential approaches to improving aramid-epoxy adhesion. Some recommendations for further studies on aramid-epoxy bonding are presented.

### **Conclusions**

Resin shrinkage does not affect the adhesion of the aramid fibers to epoxy matrices. The predicted higher radial compressive thermal stress at higher curing temperatures is not observed experimentally, reflecting a curing temperature independent failure mode.

The close matching of aramid radial thermal expansion and its Poisson ratio to those of the matrix results in lower mechanical fiber-matrix interactions for the aramid-epoxy interface than for the carbon-epoxy interface. However, theoretically if the aramid-epoxy interfacial failure mode is altered, the aramid-epoxy adhesion has the potential of up to four times higher adhesion levels.

High magnification TEM aramid-epoxy interface observation along with coated fiber experiments have shown that the fiber is thermodynamically "wet" by the matrix. Increasing the aramid surface tension is not expected to improve its wetting since the interfacial contacts are already very efficient.

The aramid interfacial failure is made by fiber fibrillation of the outer surface. This observation suggests the presence of a cohesive fibrillar layer on the fiber exterior which fails at low shear levels resulting in inefficient fiber-matrix load and low values of interfacial shear strength.

Aramid fibers lack the interfacial chemical bonding present in carbon fibers, but formation of chemical covalent bonds that only affect the aramid surface are not expected to overcome the fiber surface structural limitations.

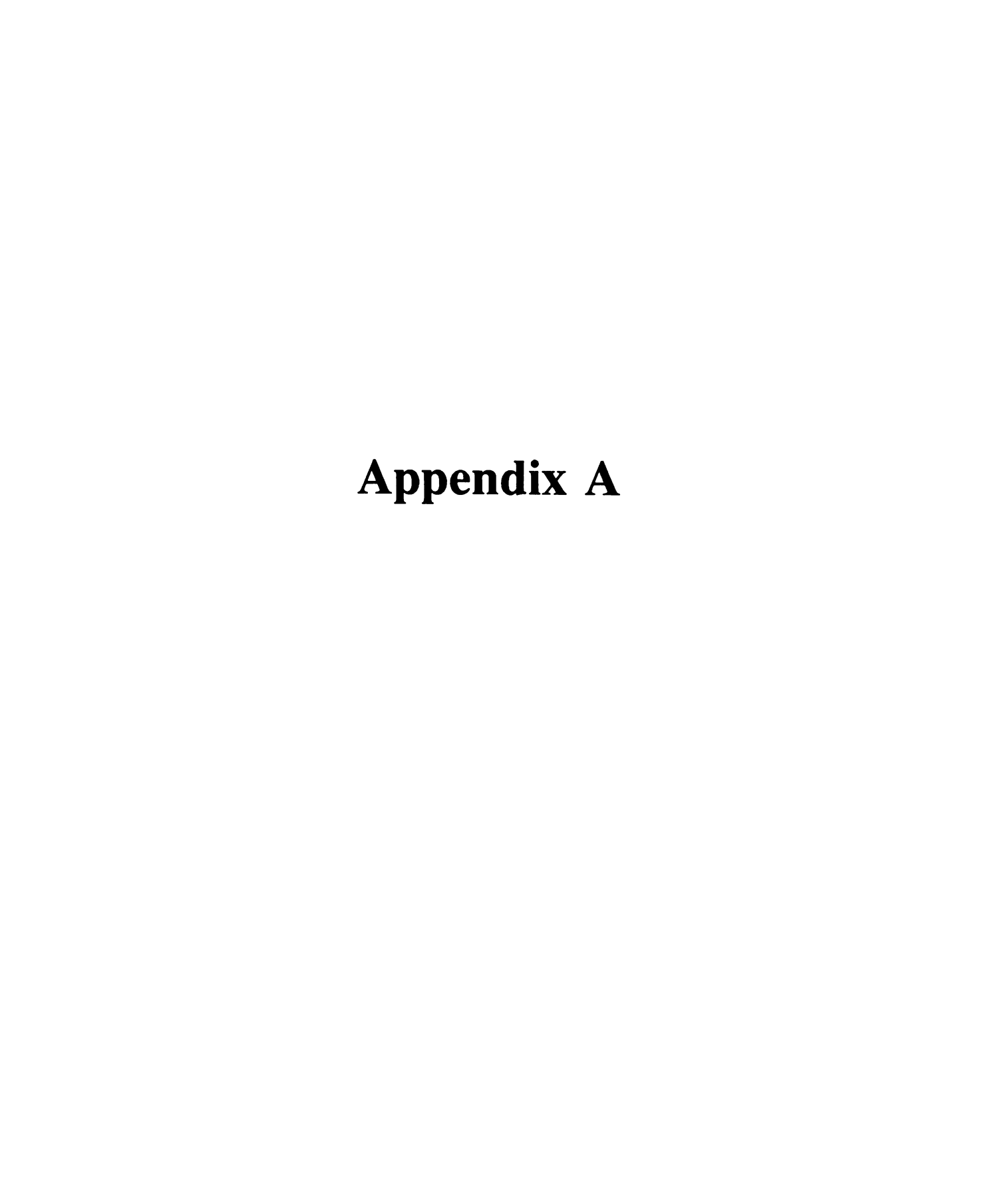
#### Recommendations

These conclusions explain the failure of some of previous attempts to improve the aramid-epoxy adhesion and suggest other potential approaches for improving the adhesion. Recommendations based on the results of the present study are suggested.

First, the aramid fiber exterior needs to be modified before significant adhesion improvements can be achieved. Although, fiber surface removal by etching techniques has been shown to improve the adhesion, but they are usually accompanied by losses in fiber tensile strength, possibly by inducing surface flaws. The fiber surface modification should not result in excessive losses of tensile strength. The fiber skin alteration can be done by changing of the fiber morphology during the manufacturing or through chemical crosslinking of the aramid polymer chains after the manufacturing. Morphological modifications during the fiber manufacturing are beyond the scope of the present study, but several ways to produce chain crosslinkings can be suggested.

The aramid polymers have amine functionalities available which could act as sites for chain crosslinking. Works by Chatzi [69] et al. has determined that 30% of the N-H groups in Kevlar 49 may be accessible for possible reactions. The hydrophilic nature of the aramid fibers permits penetration of water soluble reactants and wet chemical reactions are good possibilities. Plasma ion treatments can deposit chemical active sites within the fiber permitting epoxy crosslinking within the fiber exterior. Such matrix penetration could increase the efficiency of the shear load transfer to fiber. A novel chemical kinetic approach would be ion implantation. Metallic ions could act as catalyst for any number of chemical reactions.

Coupling agents that only react with the aramid surface are not expected to improve the aramid-epoxy adhesion since the cohesive weak boundary layer is not affected by the coupling agents. However, if the fiber skin failure is moderately improved then a coupling agent approach could have potentials.



# Appendix A

## Three-Dimensional Stress Model

Whitney et al. [1] has proposed a solutions for three-dimensional stress distribution around an isolated fiber fragment surrounded by an unbounded matrix.

Main assumptions of the Whitney's model are:

- a) The system is axisymmetric.
- b) Both fiber and matrix undergo elastic deformations.
- c) Fiber is transversely isotropic.
- d) Fiber and matrix strains match at their interface,

i.e. perfect bonding is assumed.

Complete solutions of the Whitney's model are followings:

$$\sigma_{xf}(\bar{x}) = \left(1 - (1 + 4.75\bar{x}) e^{-4.75\bar{x}}\right) A_1 \varepsilon_0$$
 (A-1)

$$\sigma_{rf}(\overline{x},r) = \left[ A_2 - A_1 \phi^2 \left( 2 - \frac{r^2}{R^2} \right) (1 - 4.75\overline{x}) e^{-4.75\overline{x}} \right] \epsilon_0$$
 (A-2)

$$\tau_{xrf}(\overline{x},r) = 4.75 \phi A_1 \varepsilon_0 \left(\frac{r}{R}\right) \overline{x} e^{-4.75\overline{x}}$$
(A-3)

$$u_{xrf}(\overline{x},r) = \begin{cases} 2.375 \ E_{1f}\overline{x} + A_1 \ \left[ 1 - \left(\frac{r}{R}\right)^2 \right] \end{cases}$$

$$+ 2.375 \, \overline{x} \, (1 + 4 v_{12} \phi^2) \, \bigg] \, e^{-4.75 \overline{x}} \bigg\} \, \frac{R \varepsilon_0}{\phi E_{1f}} \tag{A-4}$$

$$v_{rf}(r) = A_3 r \varepsilon_0 \tag{A-5}$$

$$\sigma_{xm}(\vec{x}) = \left[ E_m (1 - \frac{\overline{\varepsilon}_m}{\varepsilon_0}) - A_1 (\frac{R}{r}) (1 - 4.75 \vec{x}) e^{-4.75 \vec{x}} \right] \varepsilon_0 \tag{A-6}$$

$$\sigma_{rm}(\overline{x},r) = \left(A_2 - A_1 \phi^2 (1 - 4.75\overline{x}) e^{-4.75\overline{x}}\right) \left(\frac{r}{R}\right)^2 \varepsilon_0 \tag{A-7}$$

$$\tau_{xrm}(\overline{x},r) = 4.75 \,\phi(\frac{r}{R})^3 A_1 \,\overline{x} \,\varepsilon_0 \,e^{-4.75\overline{x}} \tag{A-8}$$

$$u_{xrm}(\overline{x},r) = 2.375 \frac{R\varepsilon_0}{\phi E_{1f}} \left[ E_{1f}\overline{x} + A_1 \left( 1 + 4v_{12f}\phi^2 \right) \left( \frac{r}{R} \right)^2 \overline{x} e^{-4.75\overline{x}} \right]$$
 (A-9)

$$v_{rm}(r) = (A_4 r + \frac{A_5}{r}) \epsilon_0$$
 (A-10)

Constants of these equations are:

$$A_{1} = E_{1f}(1 - \frac{\overline{\varepsilon}_{1f}}{\varepsilon_{0}}) + \frac{4K_{f}G_{m}v_{12f}}{K_{f} + G_{m}}$$

$$\times \left[v_{12f} - v_{m} + \frac{(1 + v_{m})\overline{\varepsilon}_{m} - \overline{\varepsilon}_{2f} - v_{12f}\overline{\varepsilon}_{1f}}{\varepsilon_{0}}\right]$$
(A-11)

$$A_2 = \frac{2 K_f G_m}{K_f + G_m} \left[ v_{12f} - v_m + \frac{(1 + v_m)\overline{\varepsilon}_m - \overline{\varepsilon}_{2f} - v_{12f}\overline{\varepsilon}_{1f}}{\varepsilon_0} \right]$$
(A-12)

$$A_{3} = \frac{-\left[K_{f} v_{12f} + v_{m} G_{m} - \frac{K_{f} (\overline{\varepsilon}_{2f} + v_{12f} \overline{\varepsilon}_{1f}) + G_{m} (1 + v_{m}) \overline{\varepsilon}_{m}}{\varepsilon_{0}}\right]}{(K_{f} + G_{m})}$$
(A-13)

$$A_4 = \frac{(1 + v_m) \,\overline{\varepsilon}_m}{\varepsilon_0} - v_m \tag{A-14}$$

74 Appendix A

$$A_5 = \frac{R^2 K_f}{K_f + G_m} \left[ v_m - v_{12f} + \frac{\overline{\varepsilon}_{2f} + v_{12f} \overline{\varepsilon}_{1f} - (1 + v_m)}{\varepsilon_0} \right]$$
 (A-15)

$$K_{f} = \frac{E_{m}}{2\left[2 - \frac{E_{2f}}{2G_{2f}} - \frac{2\nu_{21f}E_{2f}}{E_{1f}}\right]}$$
(A-16)

$$\phi = \left[ \frac{G_m}{E_{1f} - 4v_{12f}G_m} \right]^{\frac{1}{2}} \tag{A-17}$$

$$\overline{\varepsilon}_m \equiv \alpha_m \Delta T \tag{A-18}$$

$$\overline{\varepsilon}_{1f} \equiv \alpha_{1f} \Delta T \tag{A-19}$$

$$\overline{\varepsilon}_{2f} \equiv \alpha_{2f} \Delta T \tag{A-20}$$

$$\varepsilon_0 = \varepsilon_{uf} - \overline{\varepsilon}_m \tag{A-21}$$

$$\overline{x} = \frac{x}{l_c} \tag{A-22}$$

Note that  $\Delta T \leq 0$ .

Whitney has defined the critical length  $l_c$  such that 95% of the applied axial load is transferred to the fiber *i.e.* 

$$\sigma_{xf}(l_c) = 0.95 A_1 \varepsilon_0$$

The interfacial stress distribution obtained from the model are illustrated in the Figure 27.

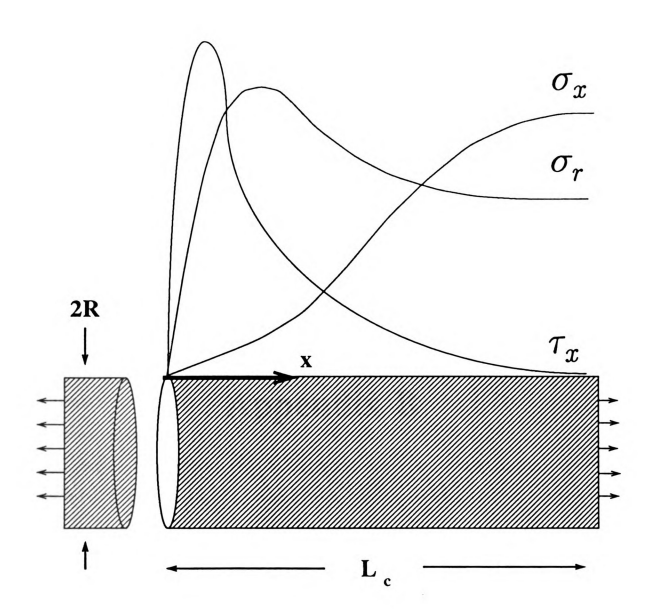


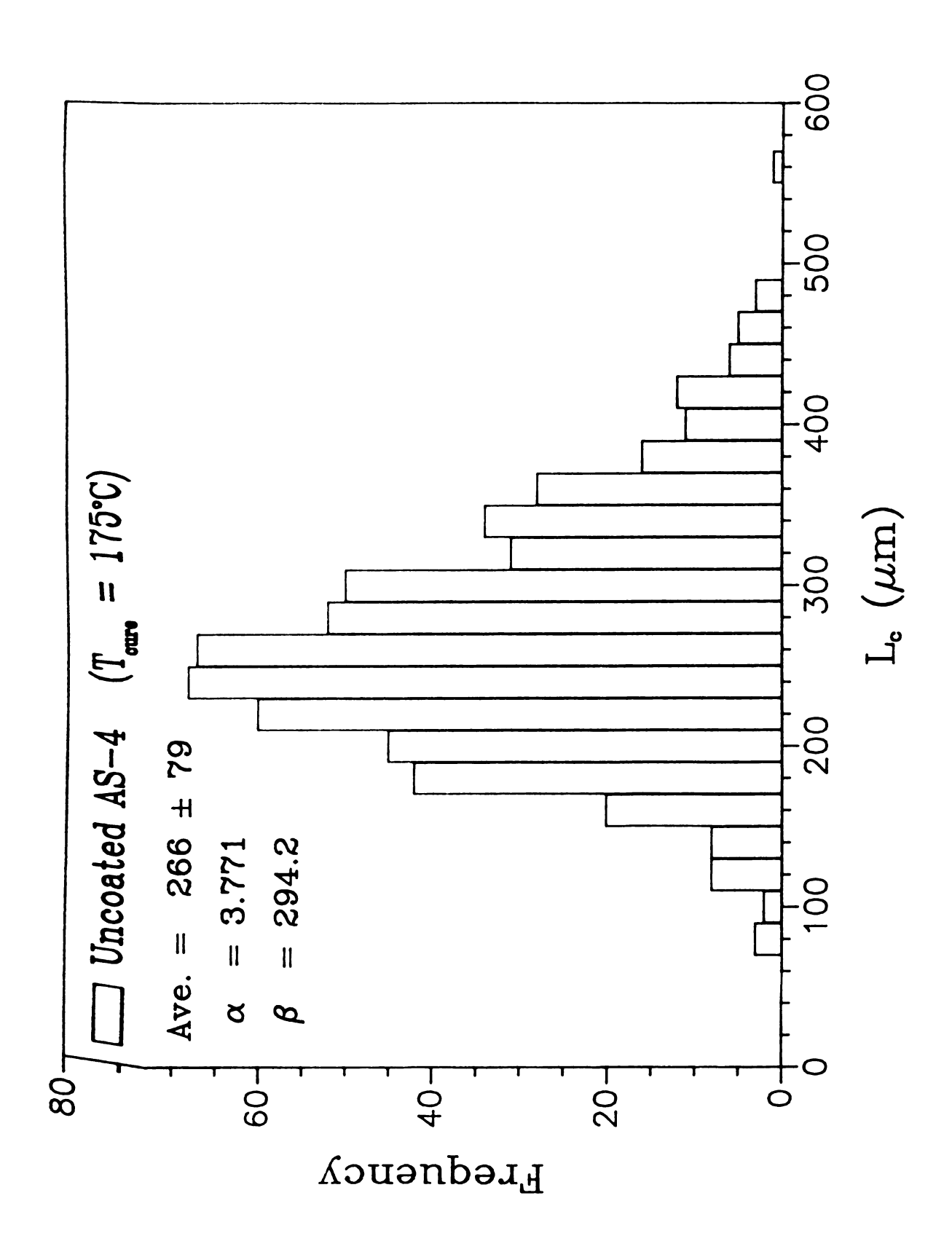
Figure 27 - An exaggerated diagram of the stress distributions around a fiber fragment. The stress magnitudes are arbitrary.

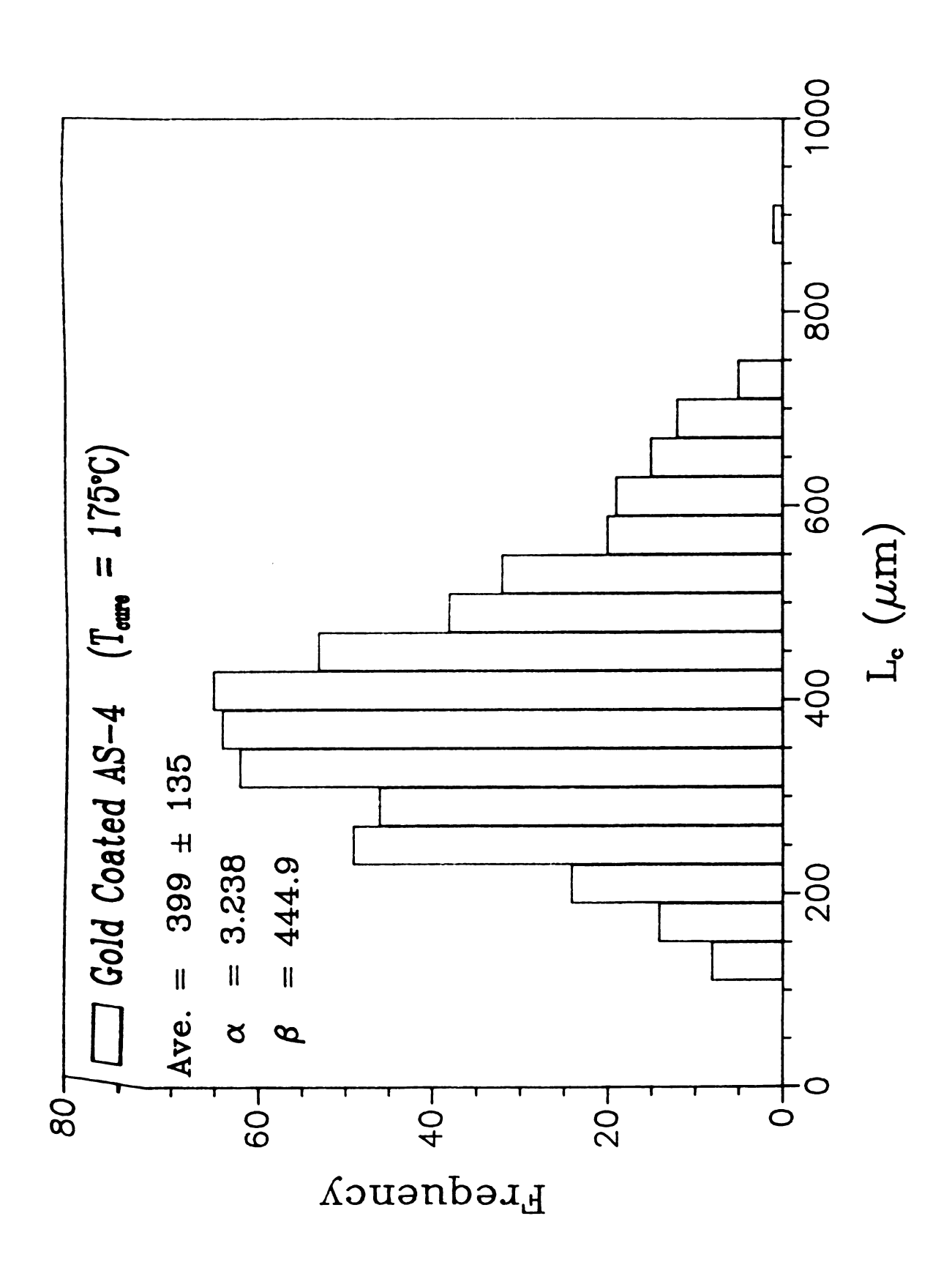


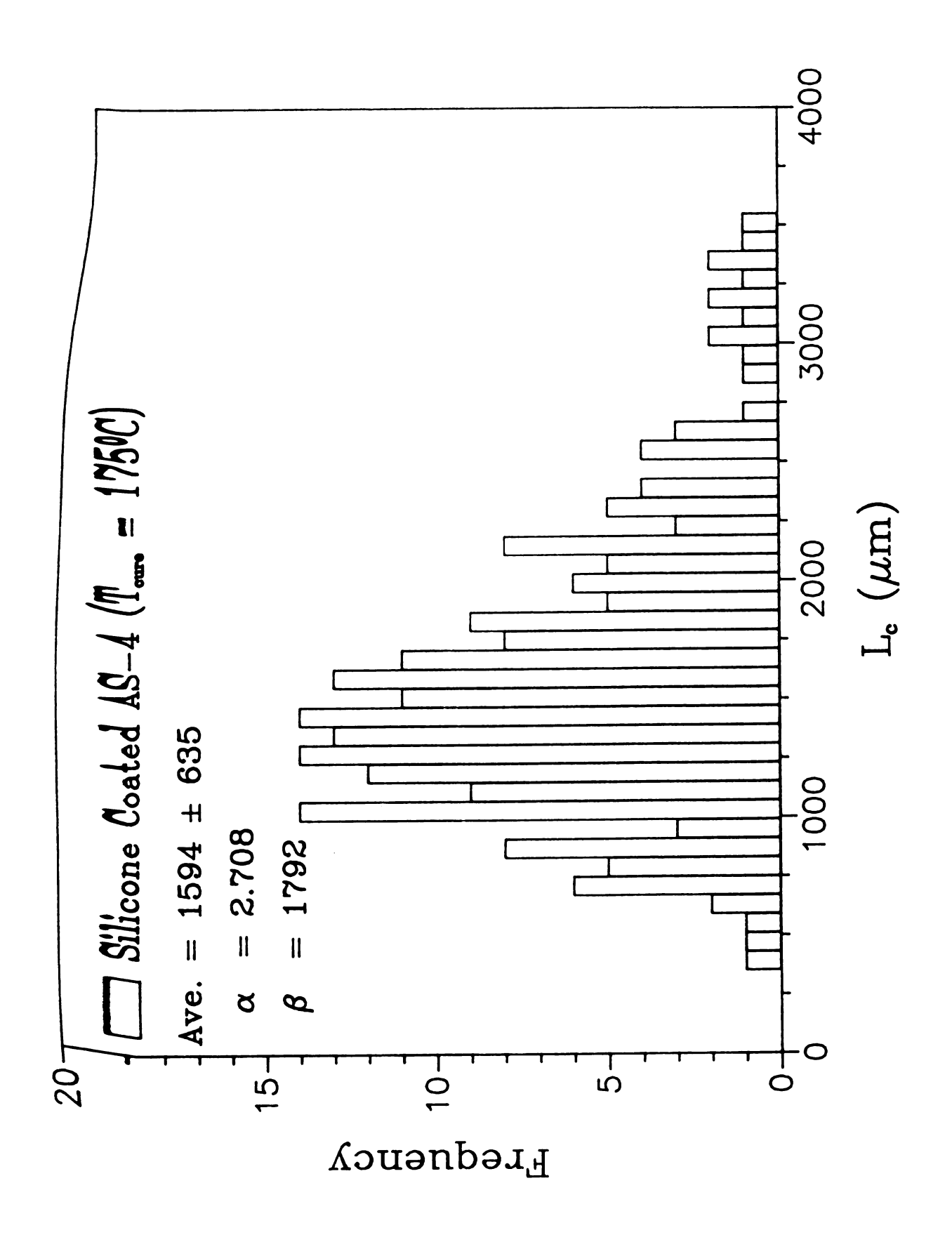
# Appendix B

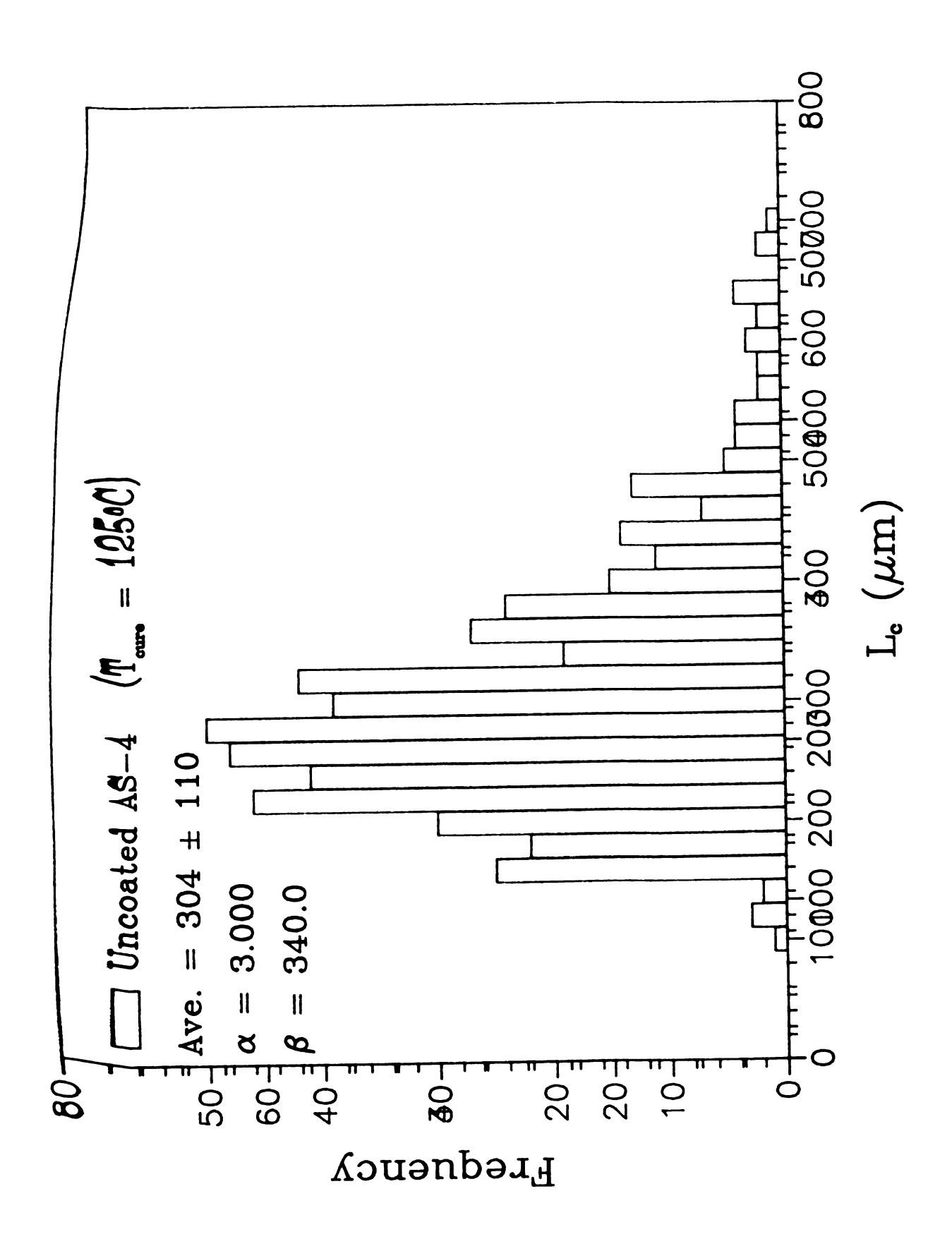
# Critical Length Distributions

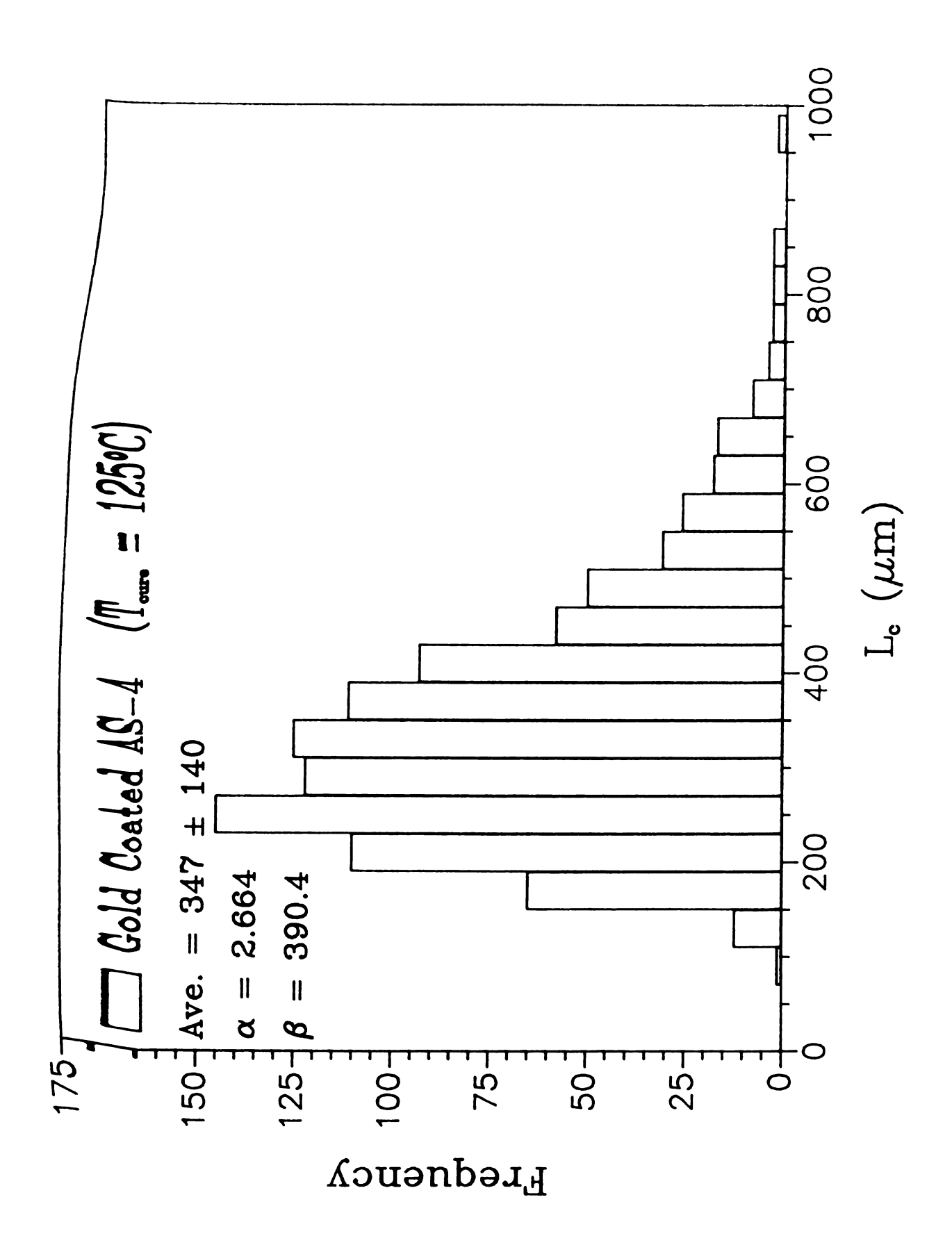
The following diagrams display the experimental critical length distributions for the coated and uncoated aramid (Kevlar 49) and carbon (AS-4) samples cured at different curing temperatures. The carbon fiber data have been modeled by Weibull distributions and their plots include the Weibull constants as well as their Weibull mean and standard deviations. For the aramid data a normal distribution has been utilized and their corresponding mean and standard distributions are listed.

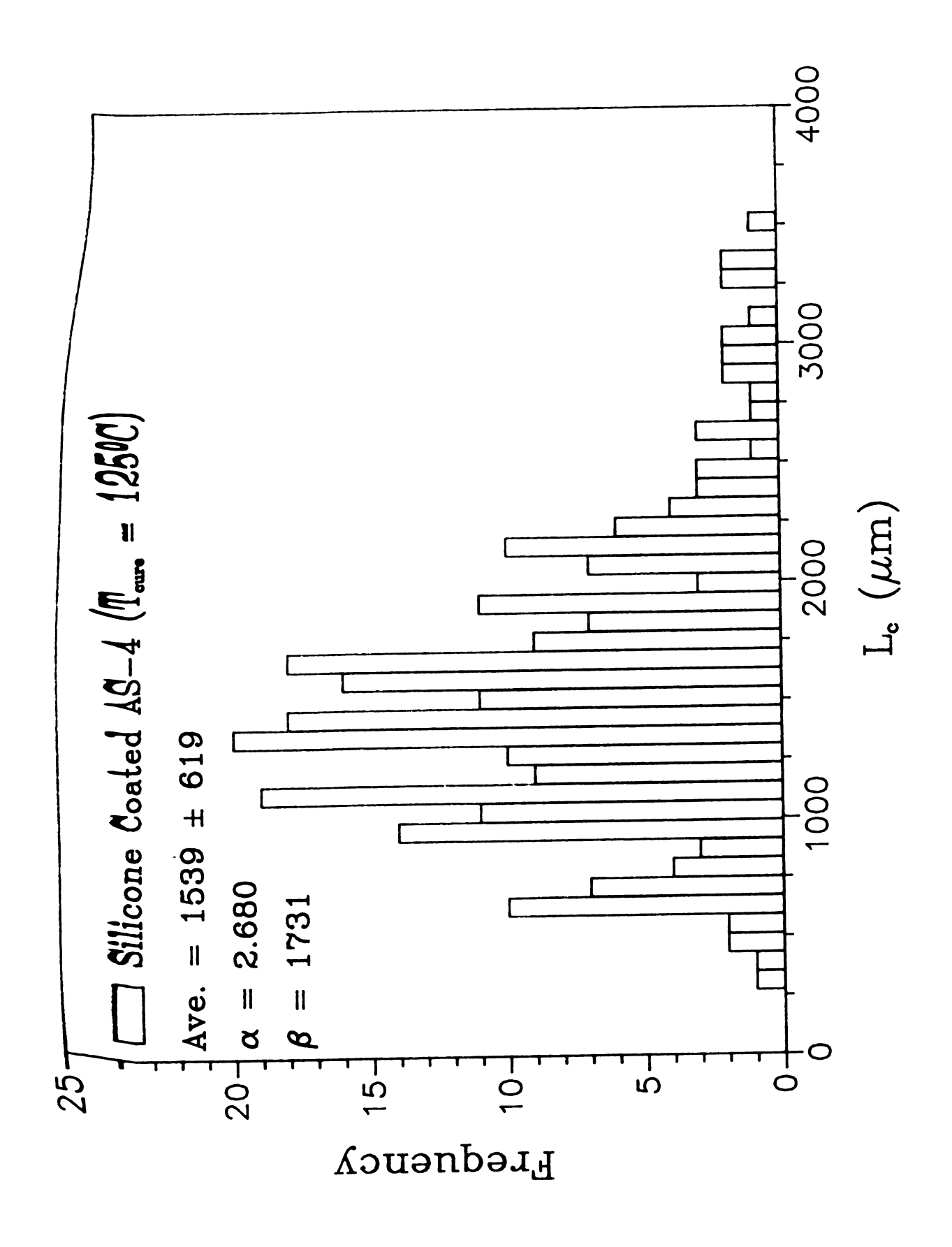


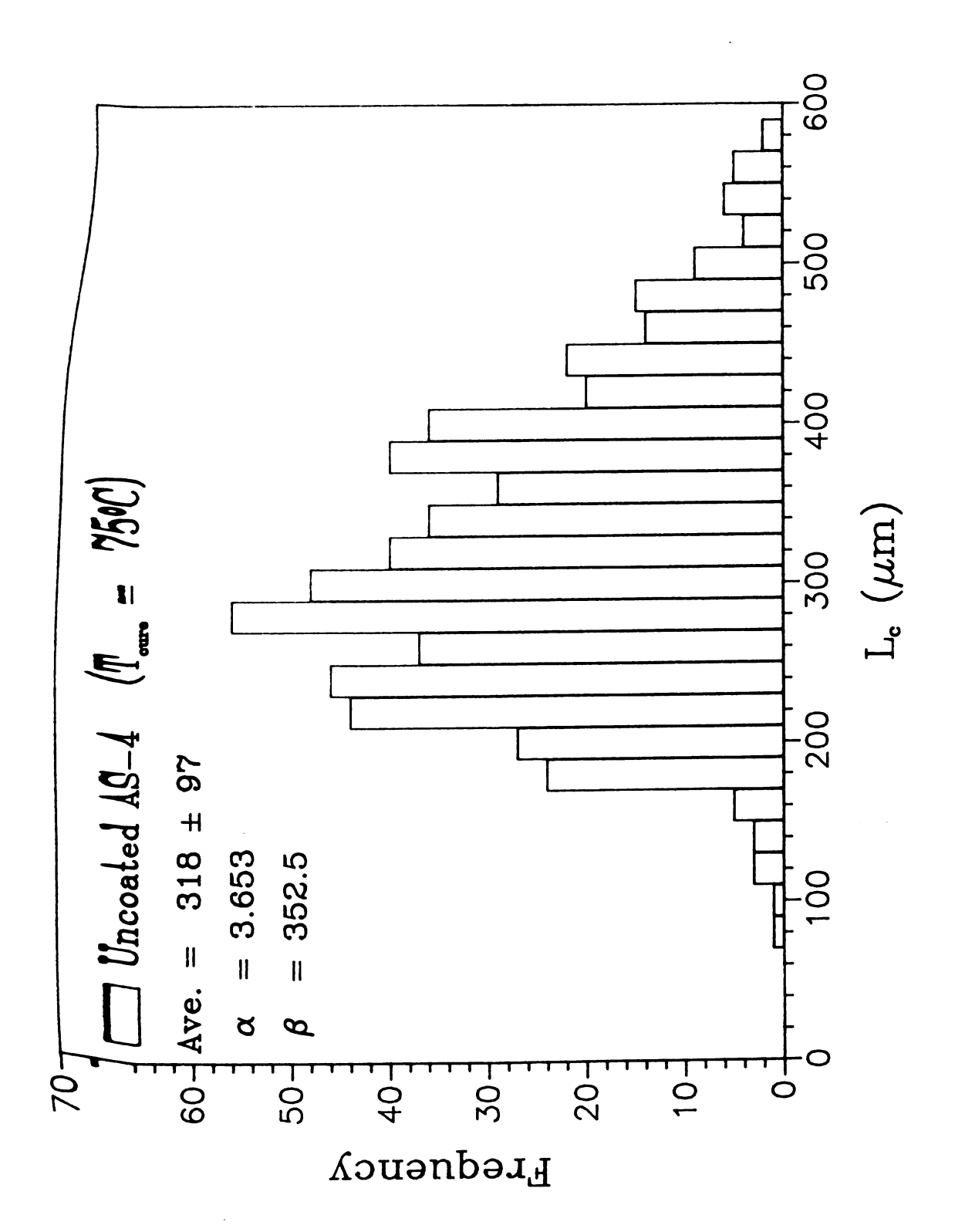


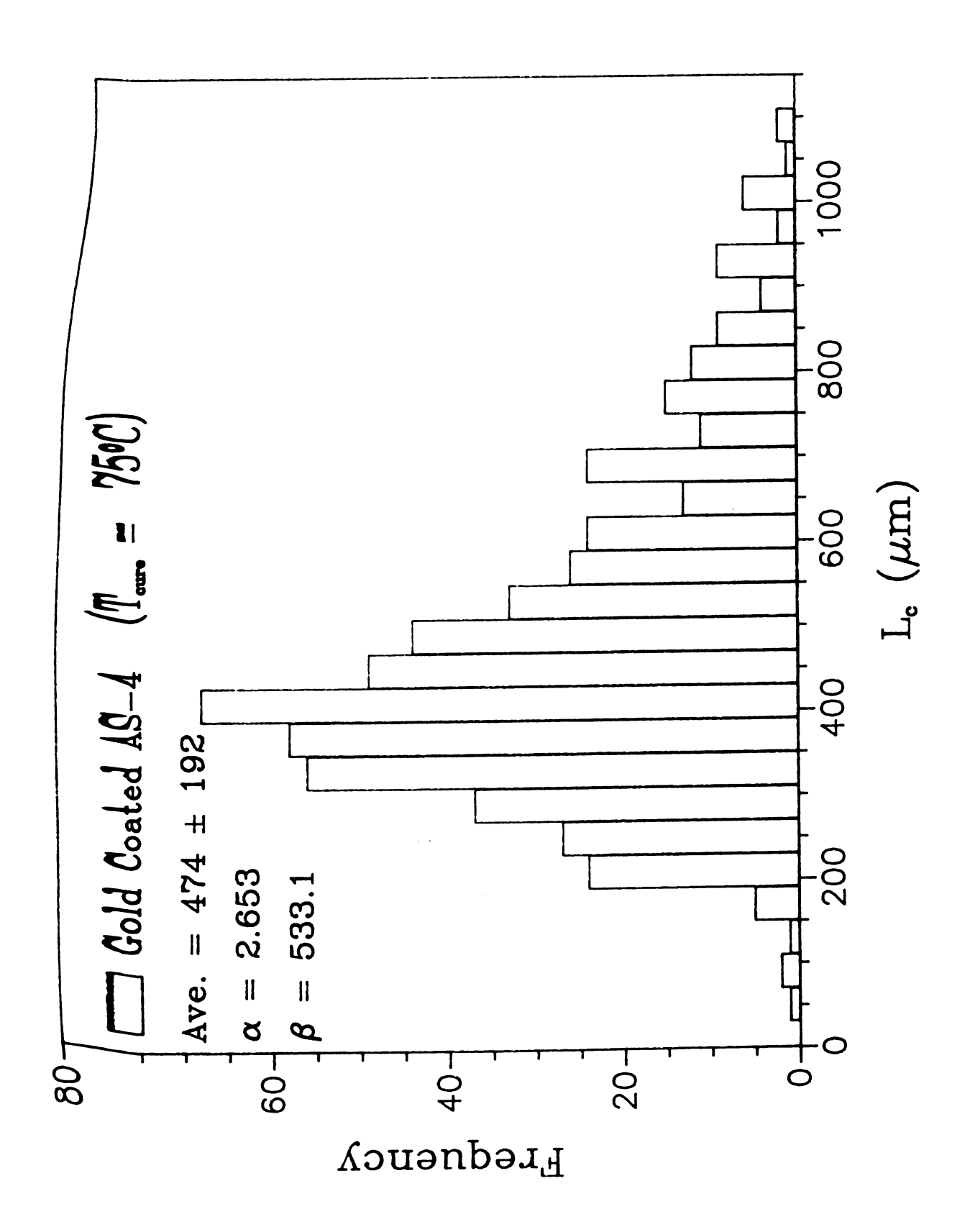


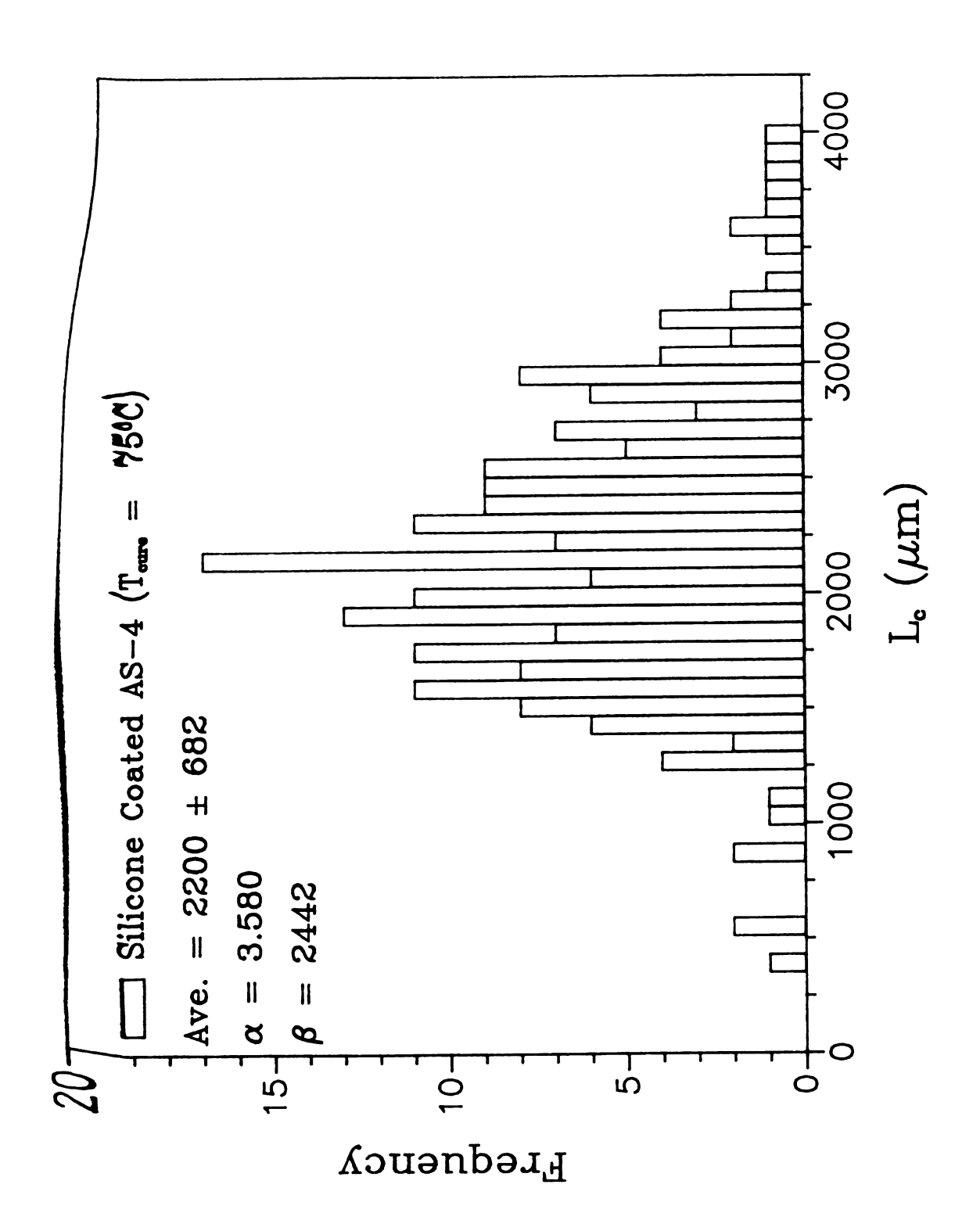




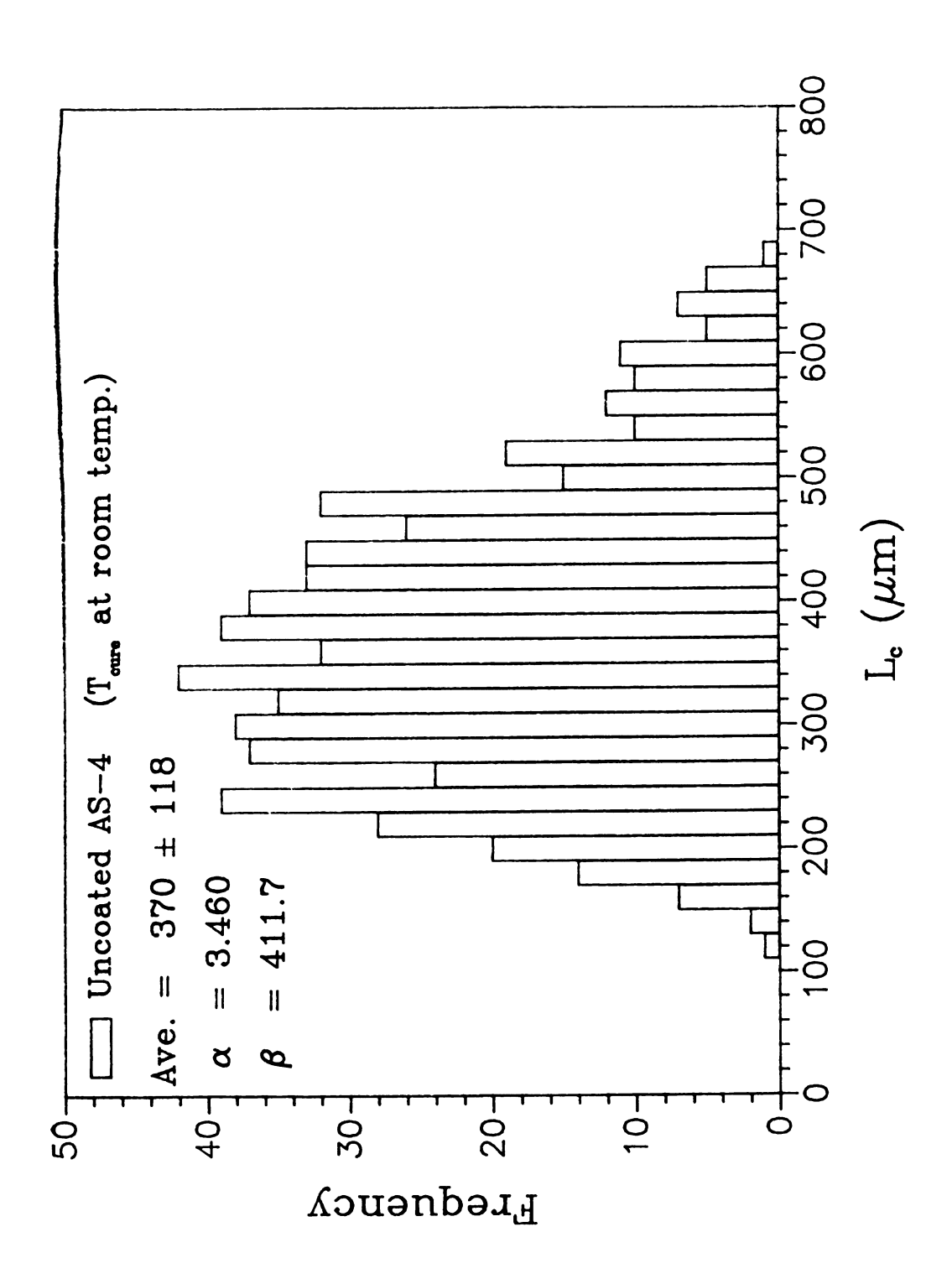


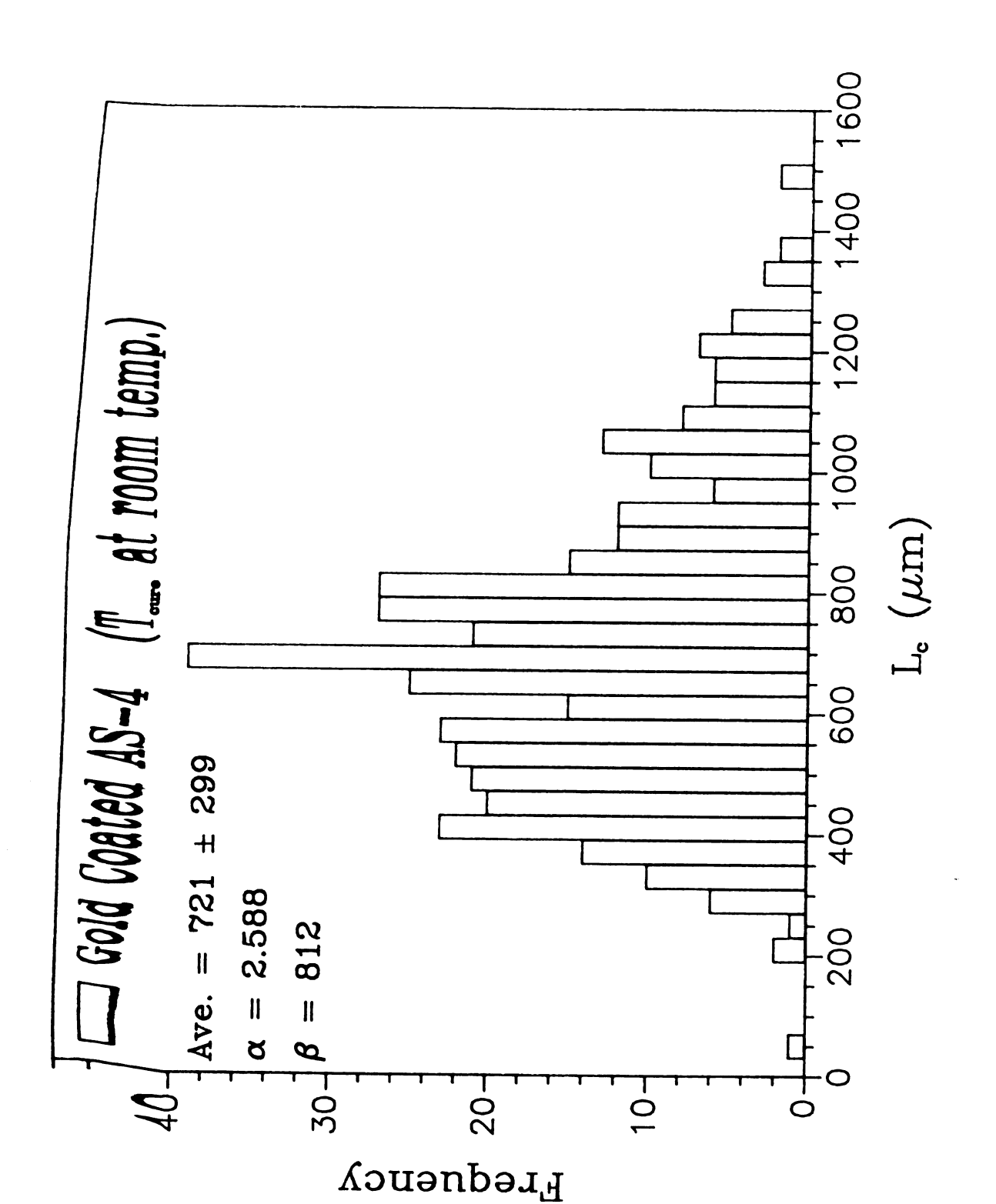


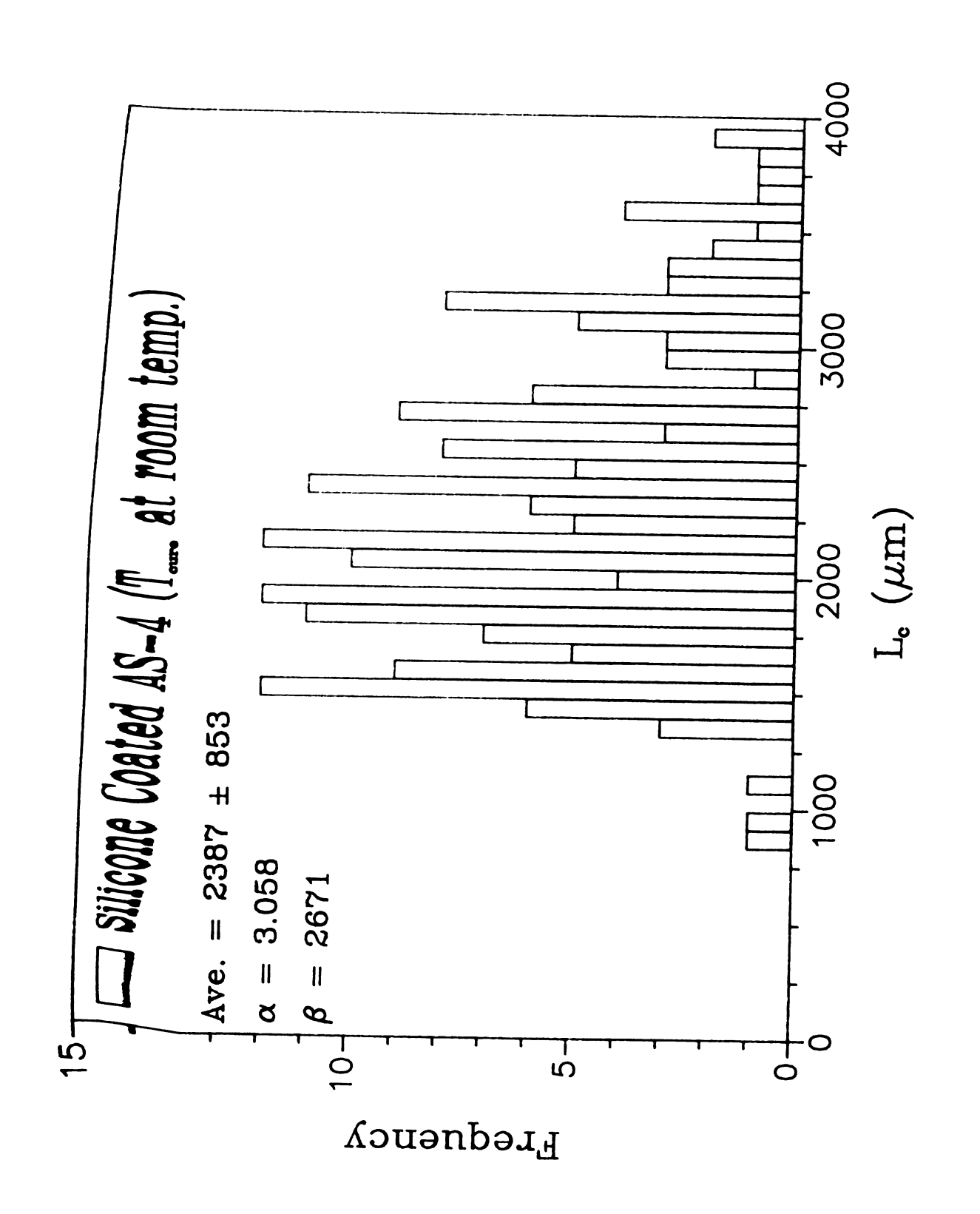


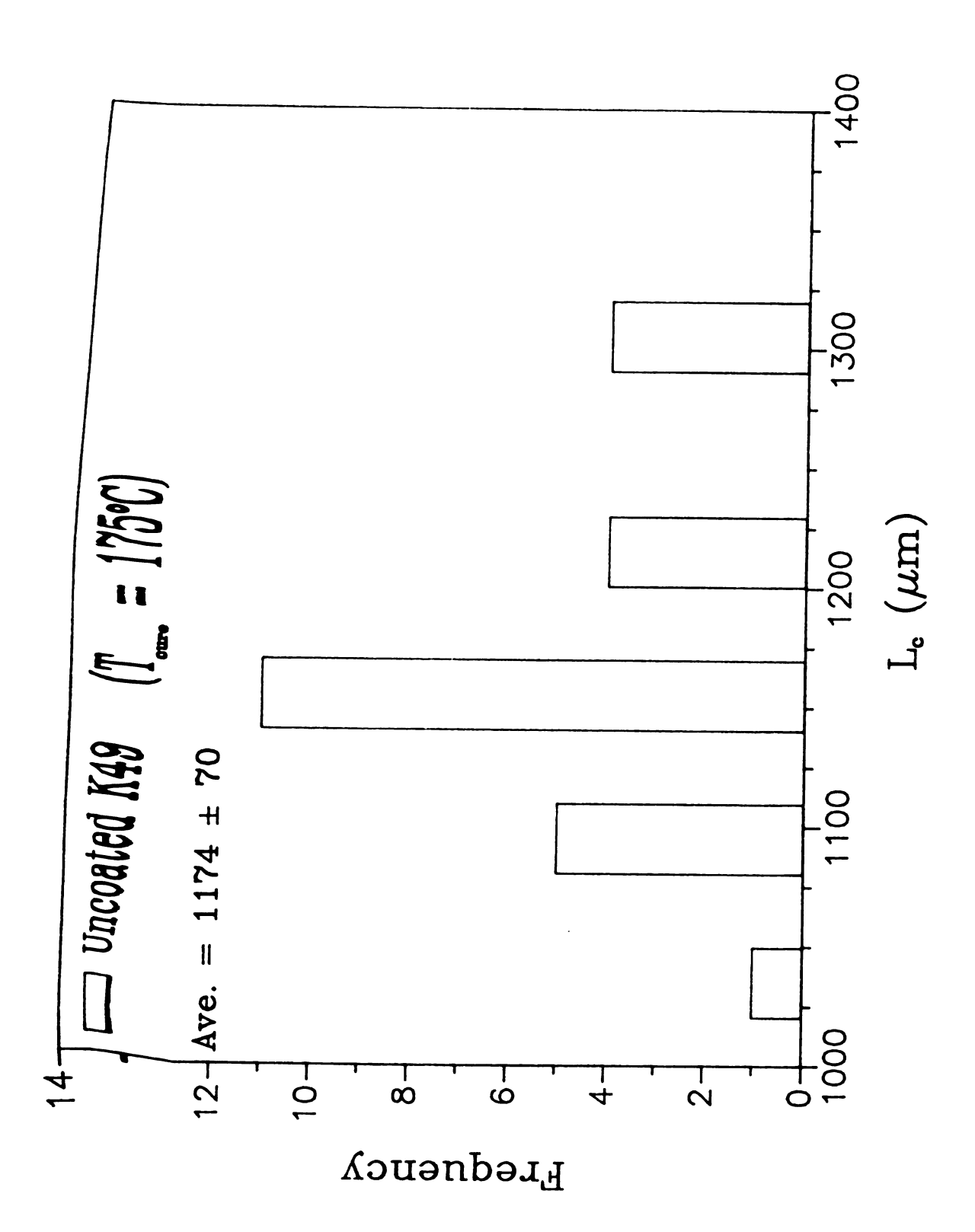


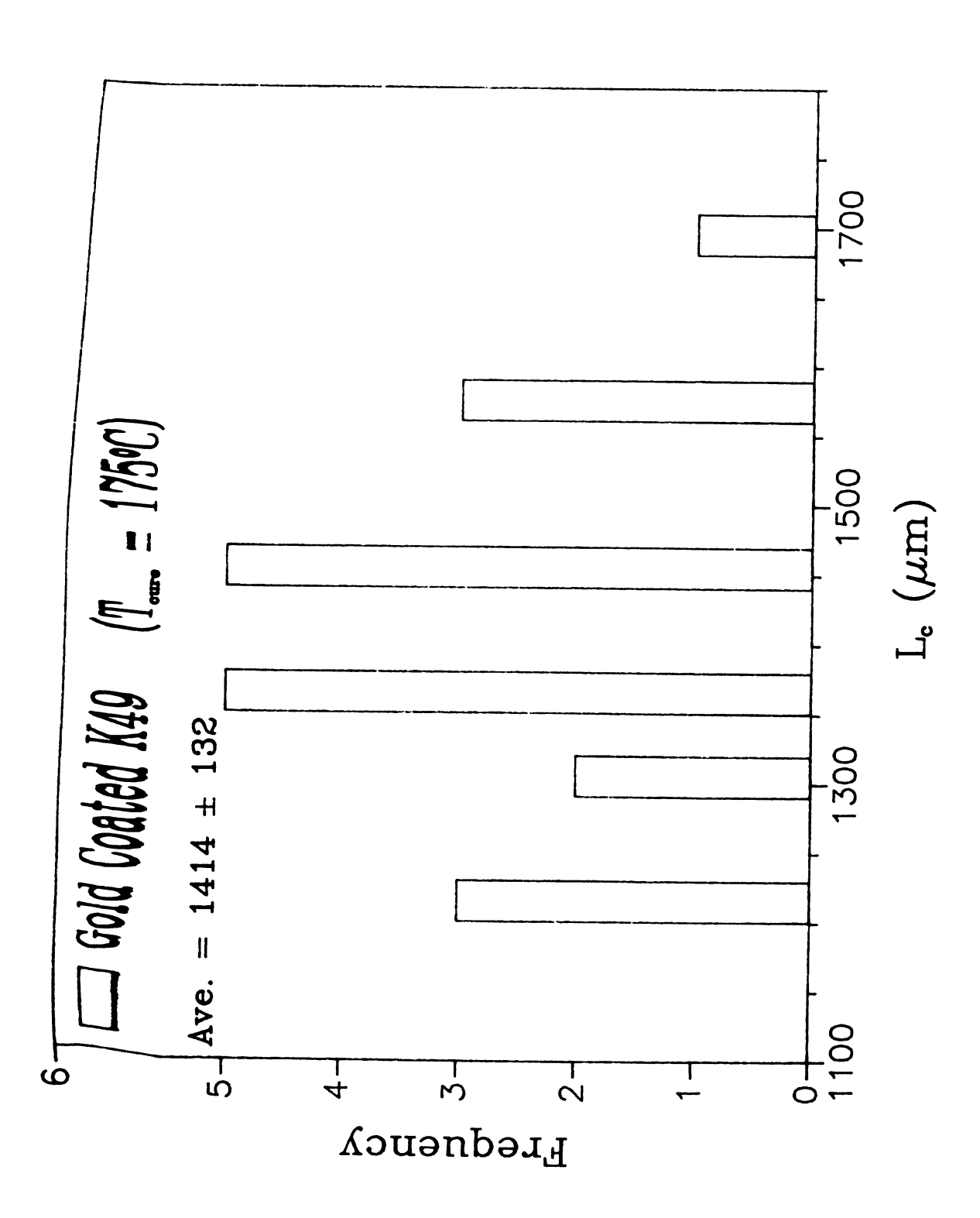


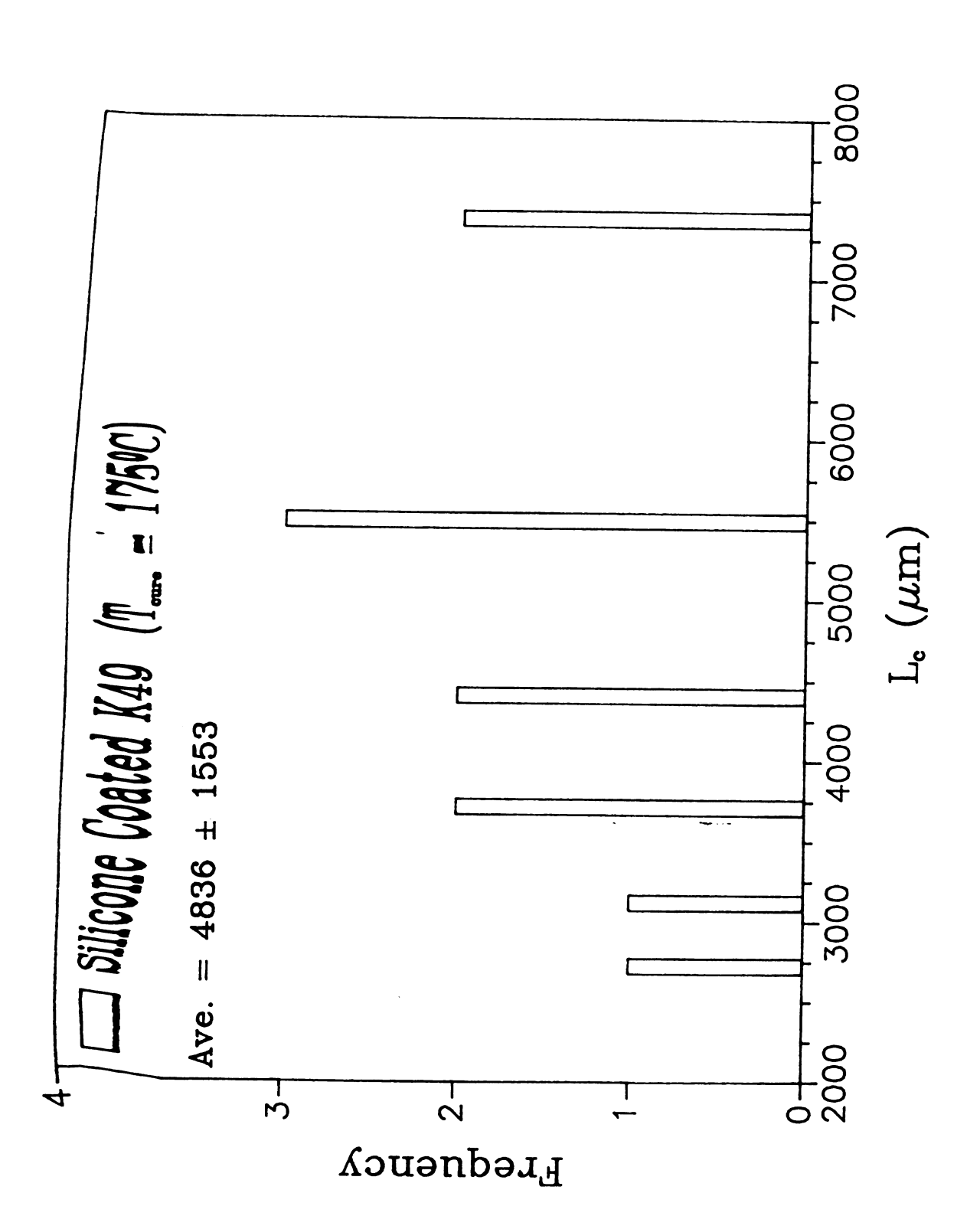


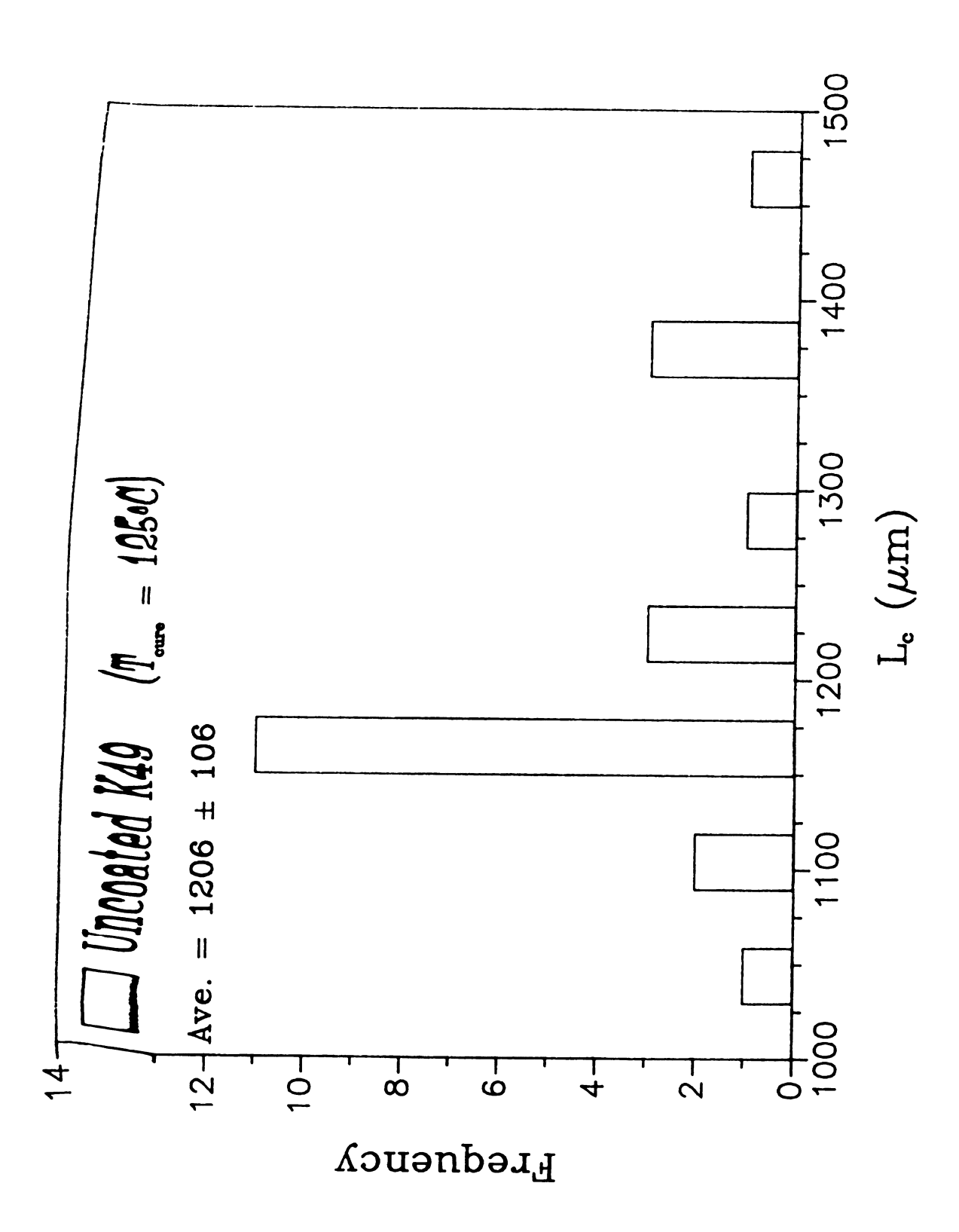


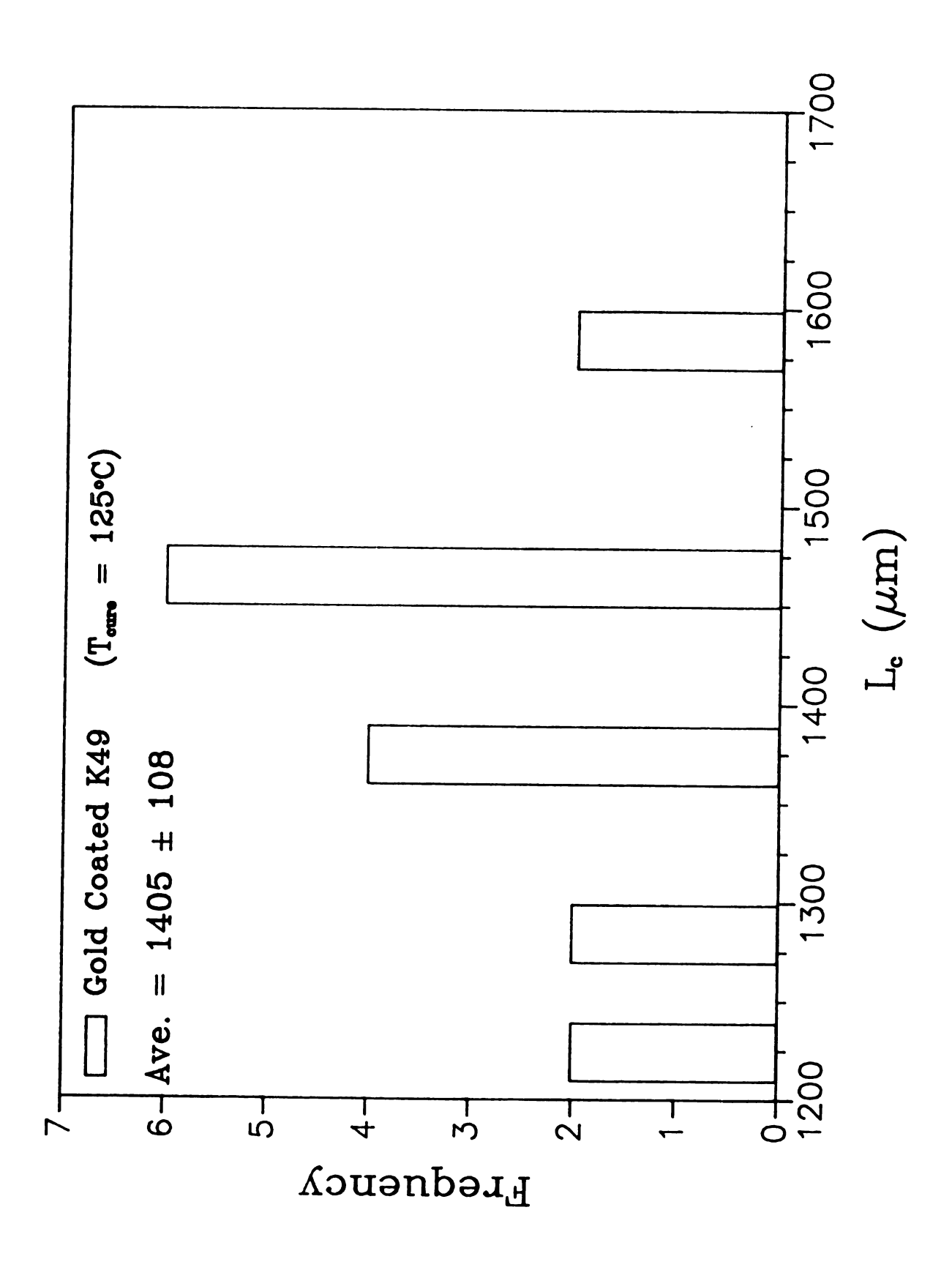


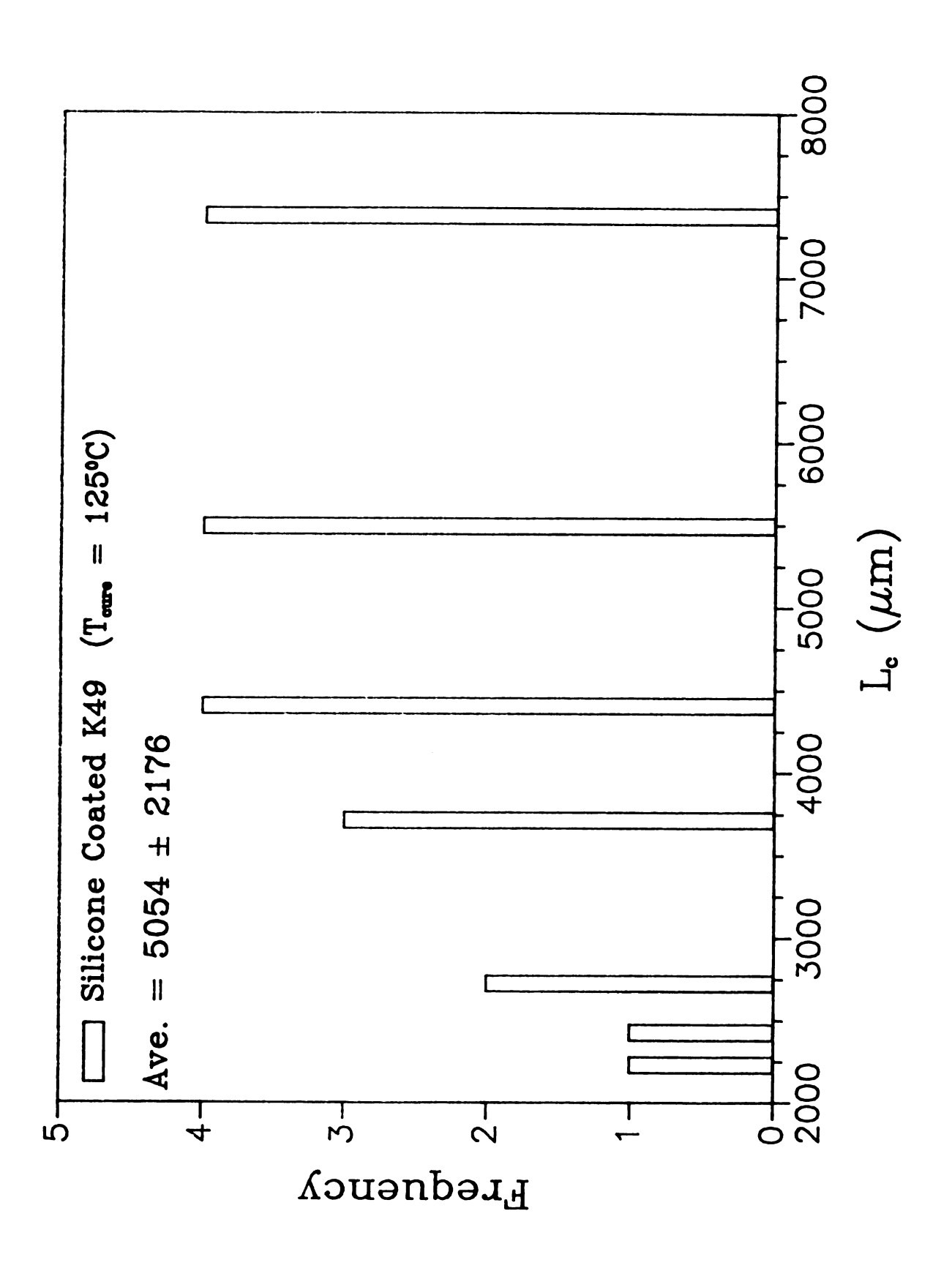


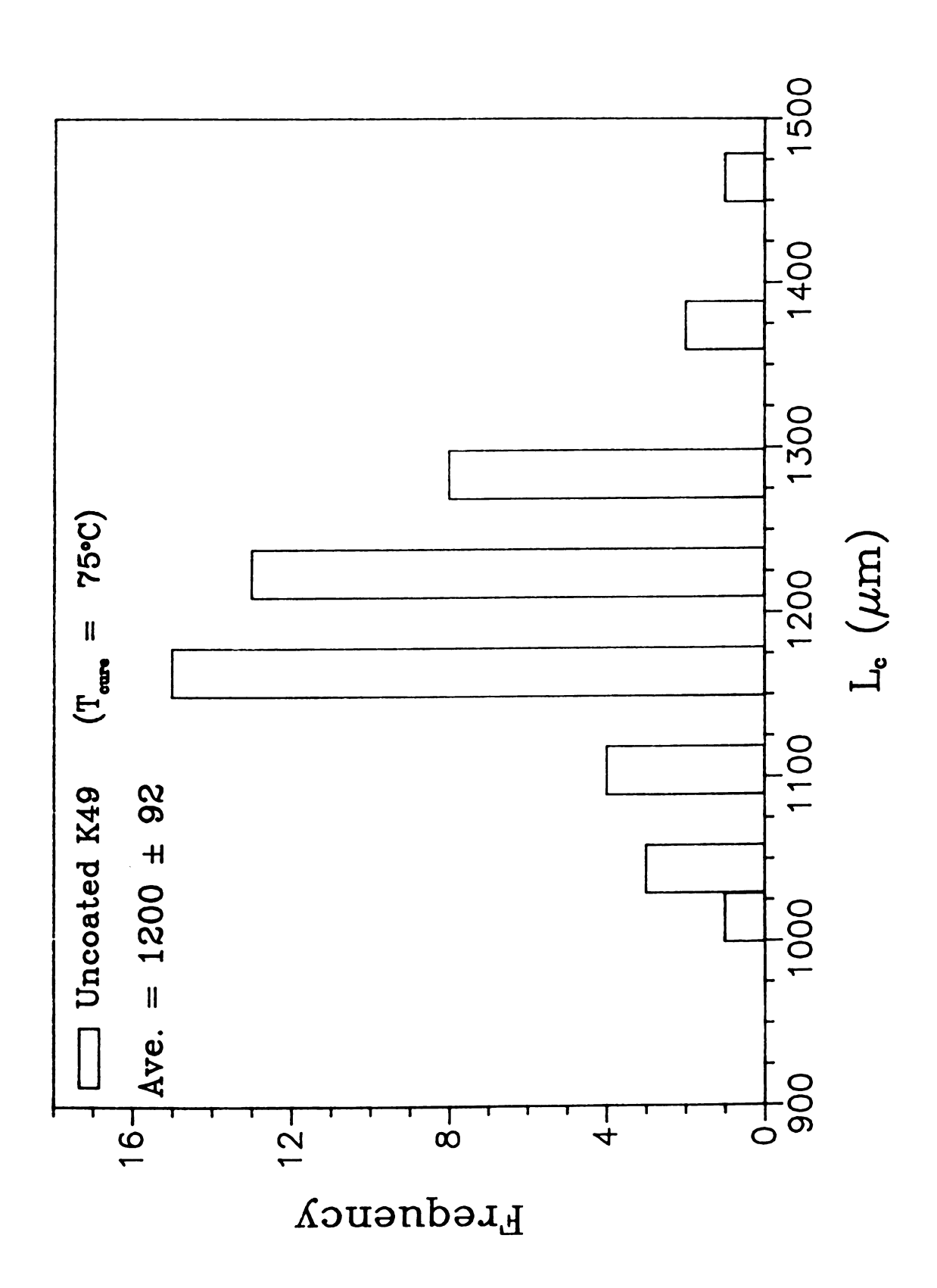


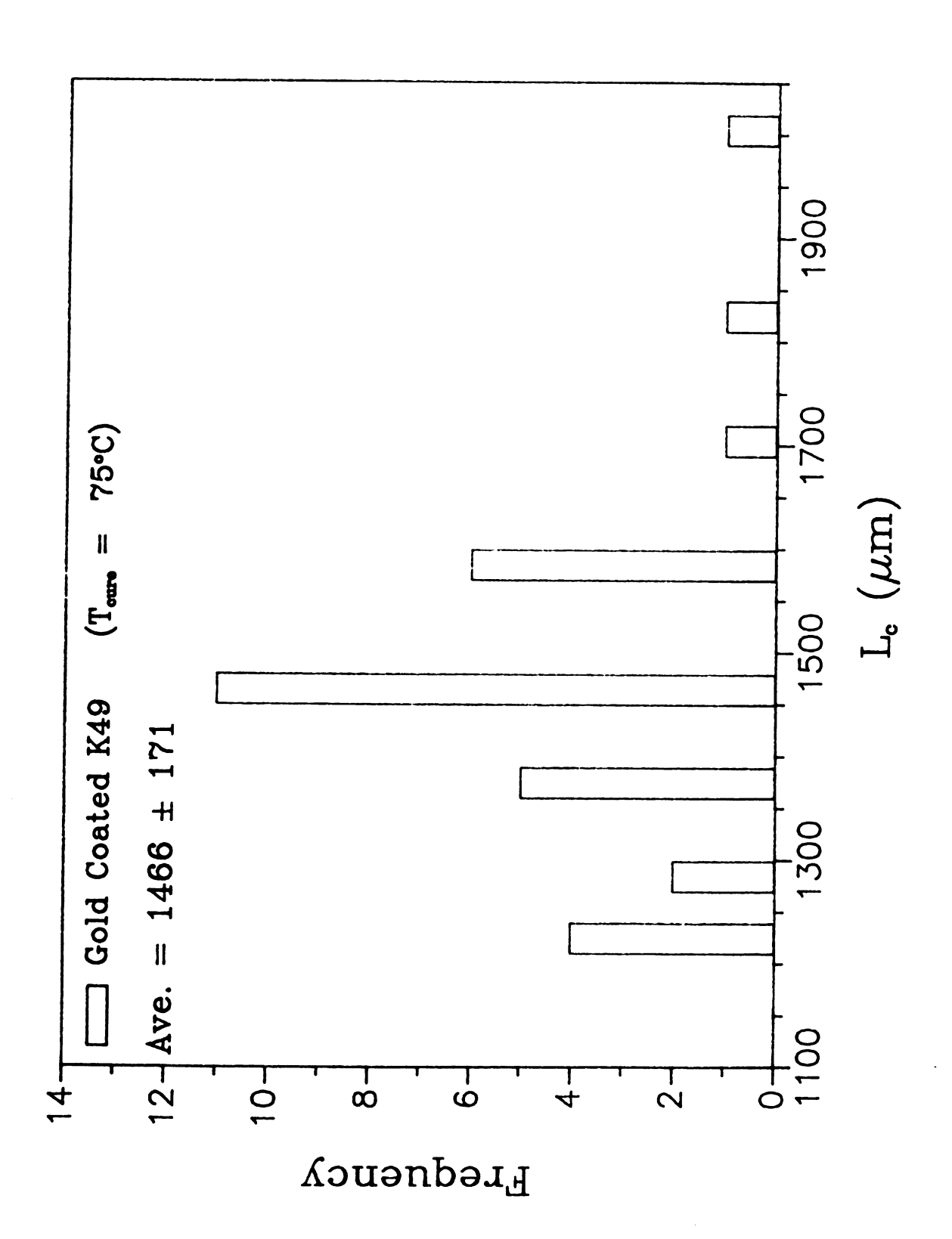


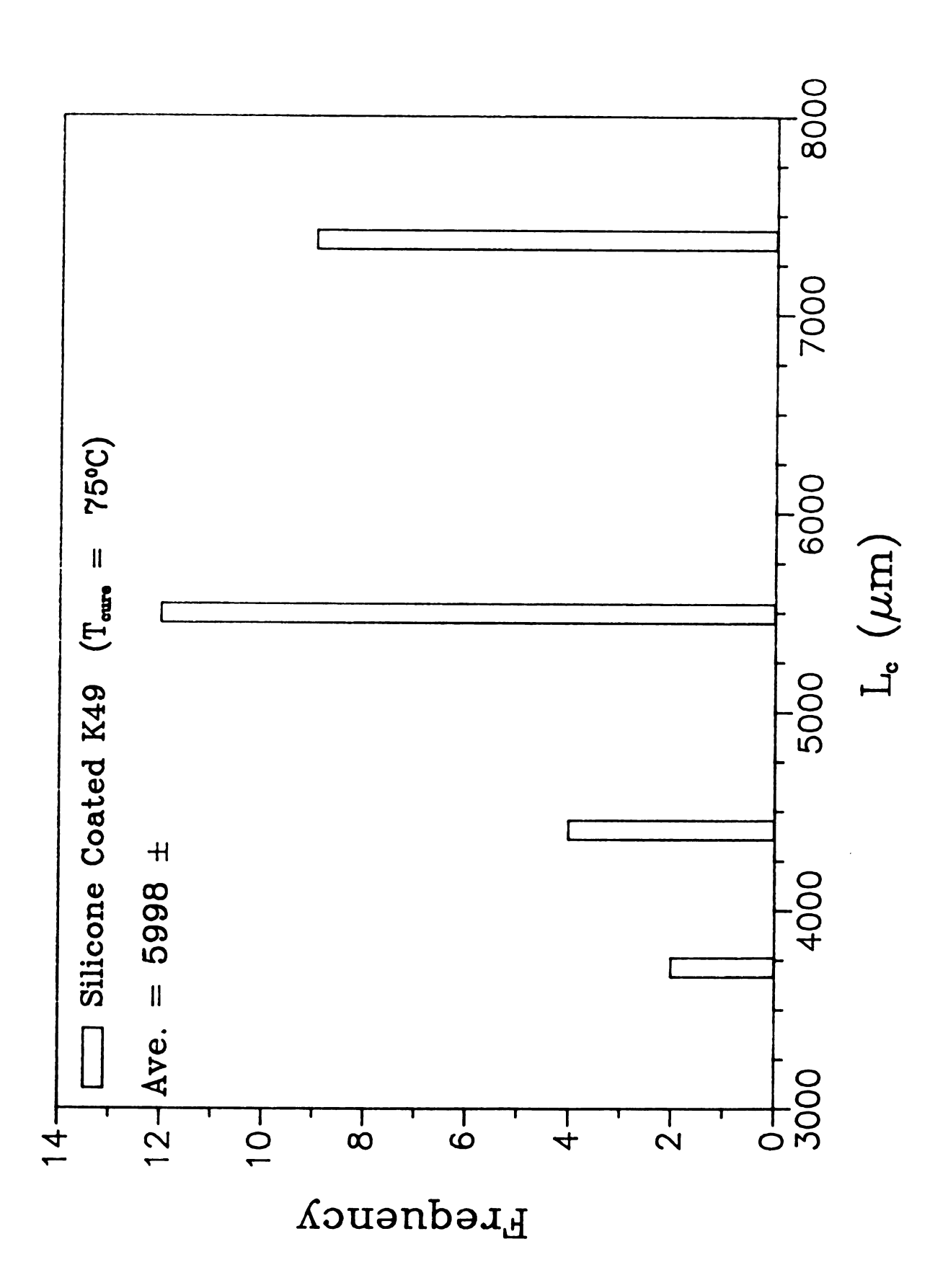


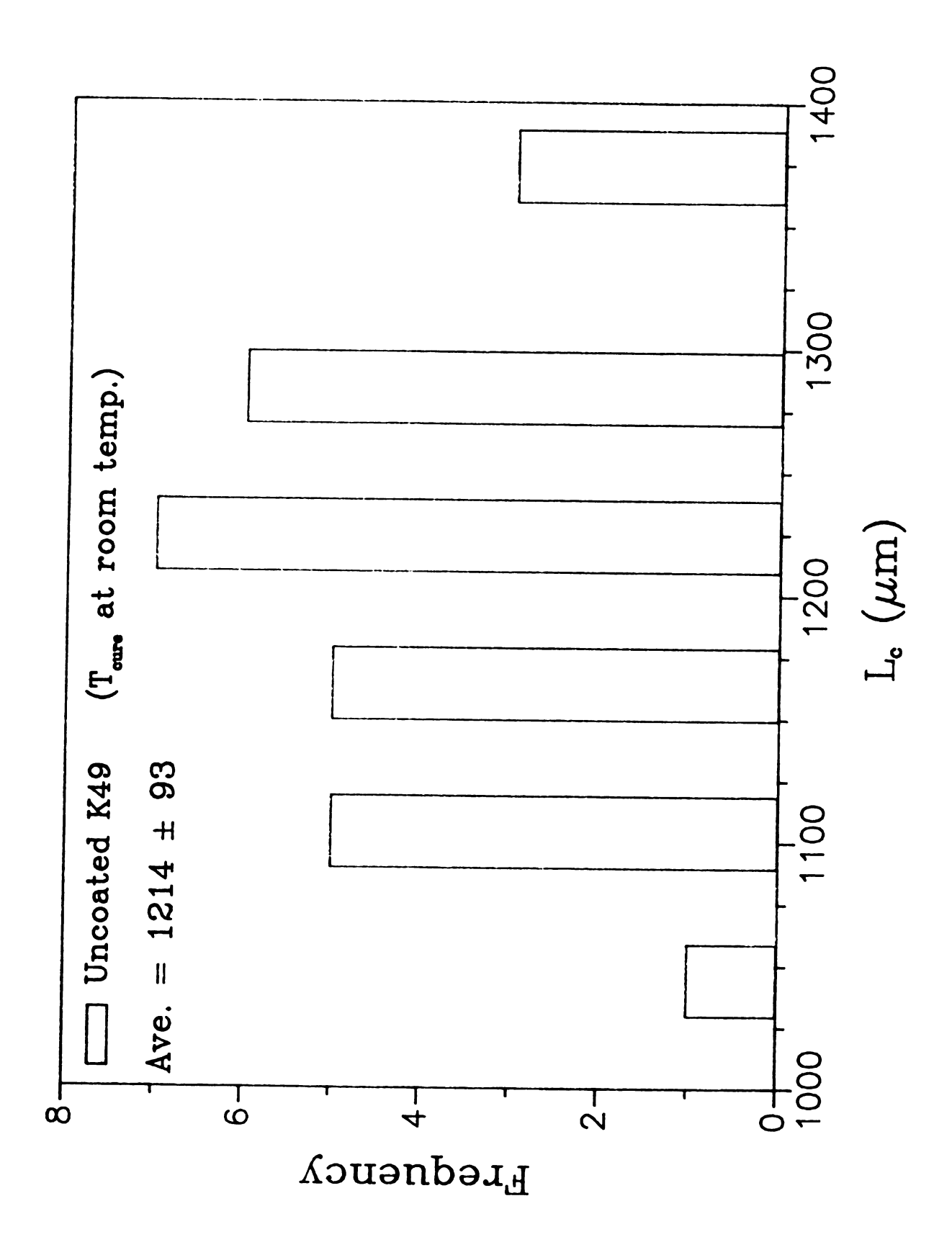


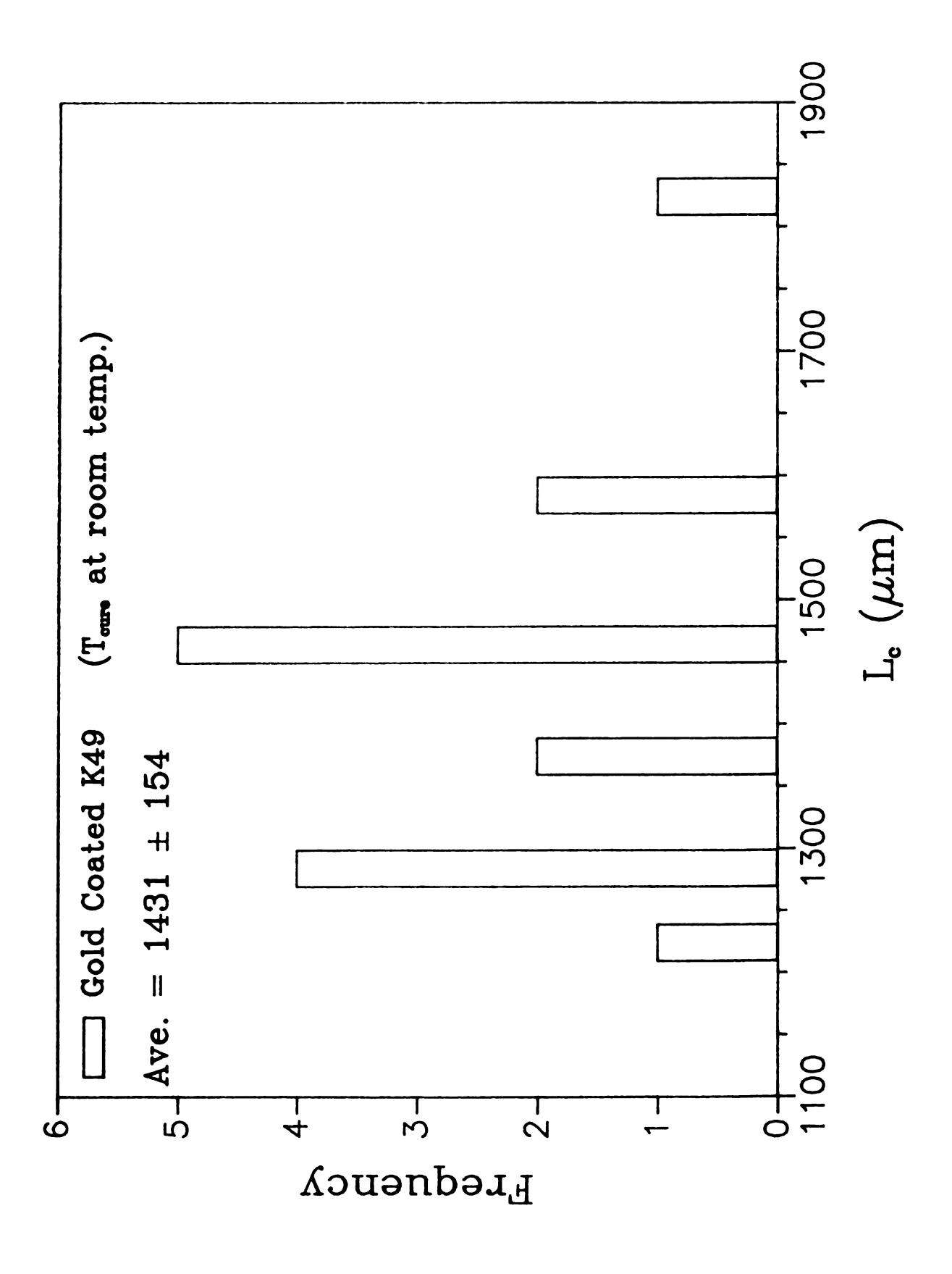


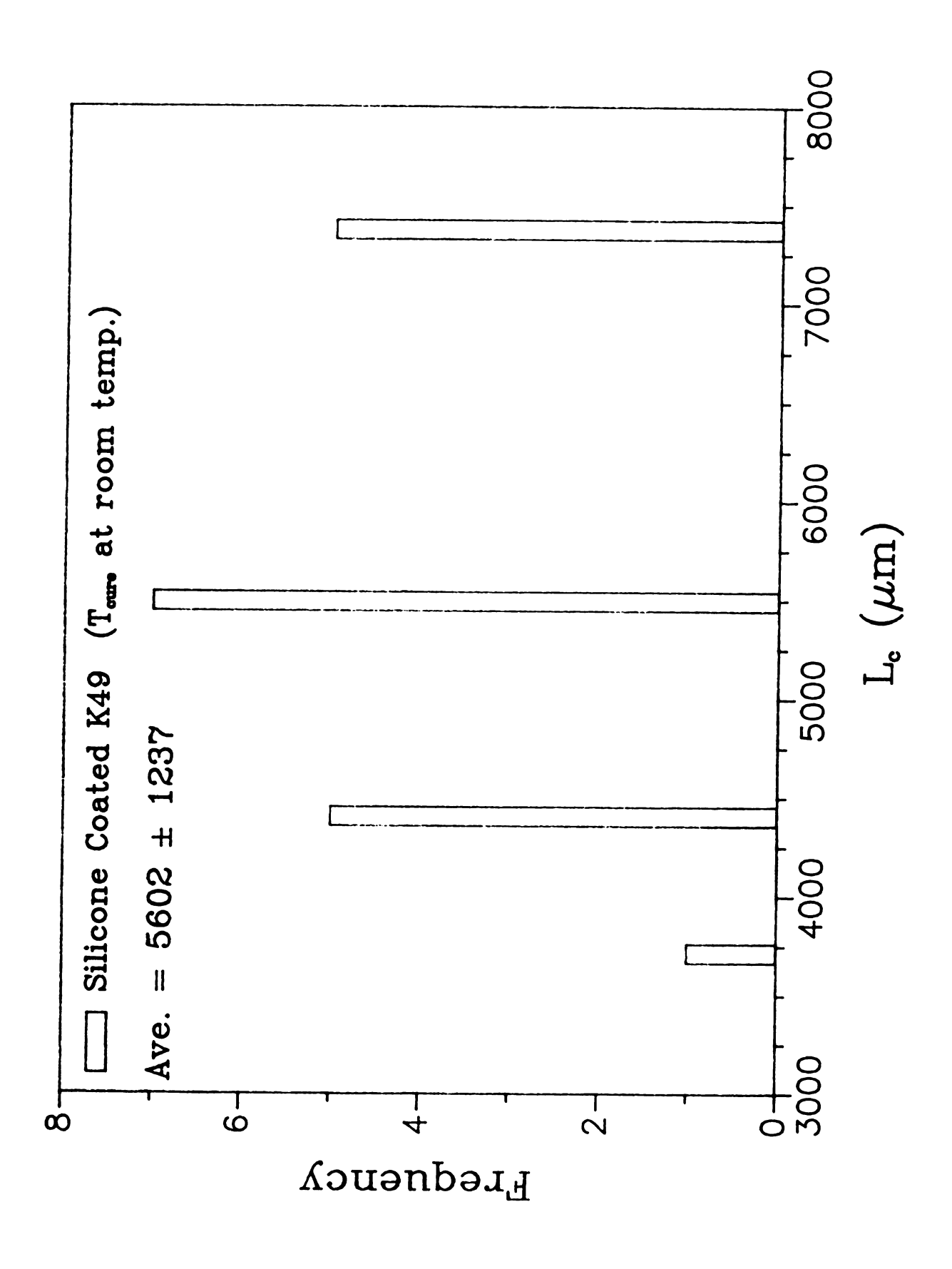










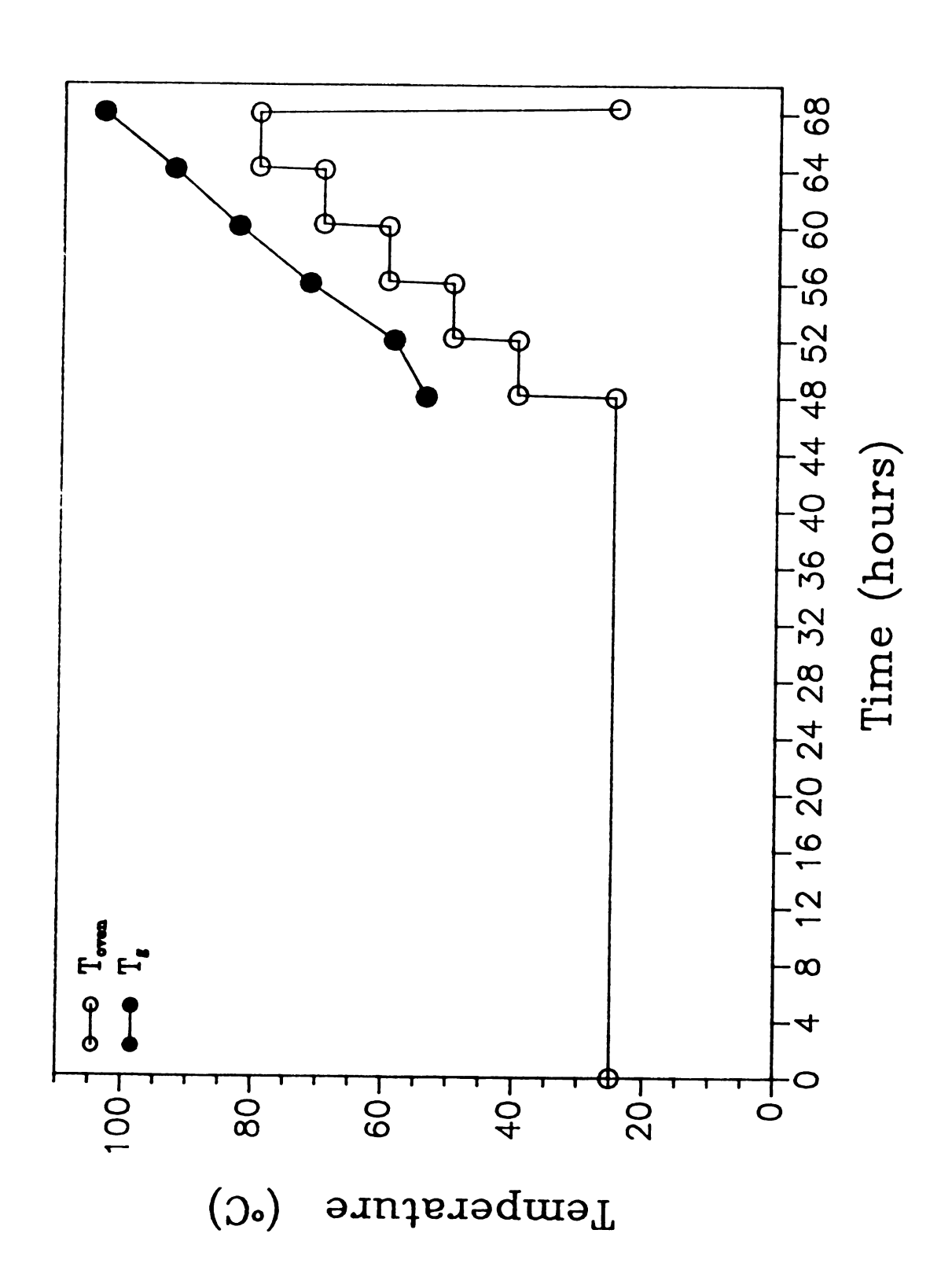


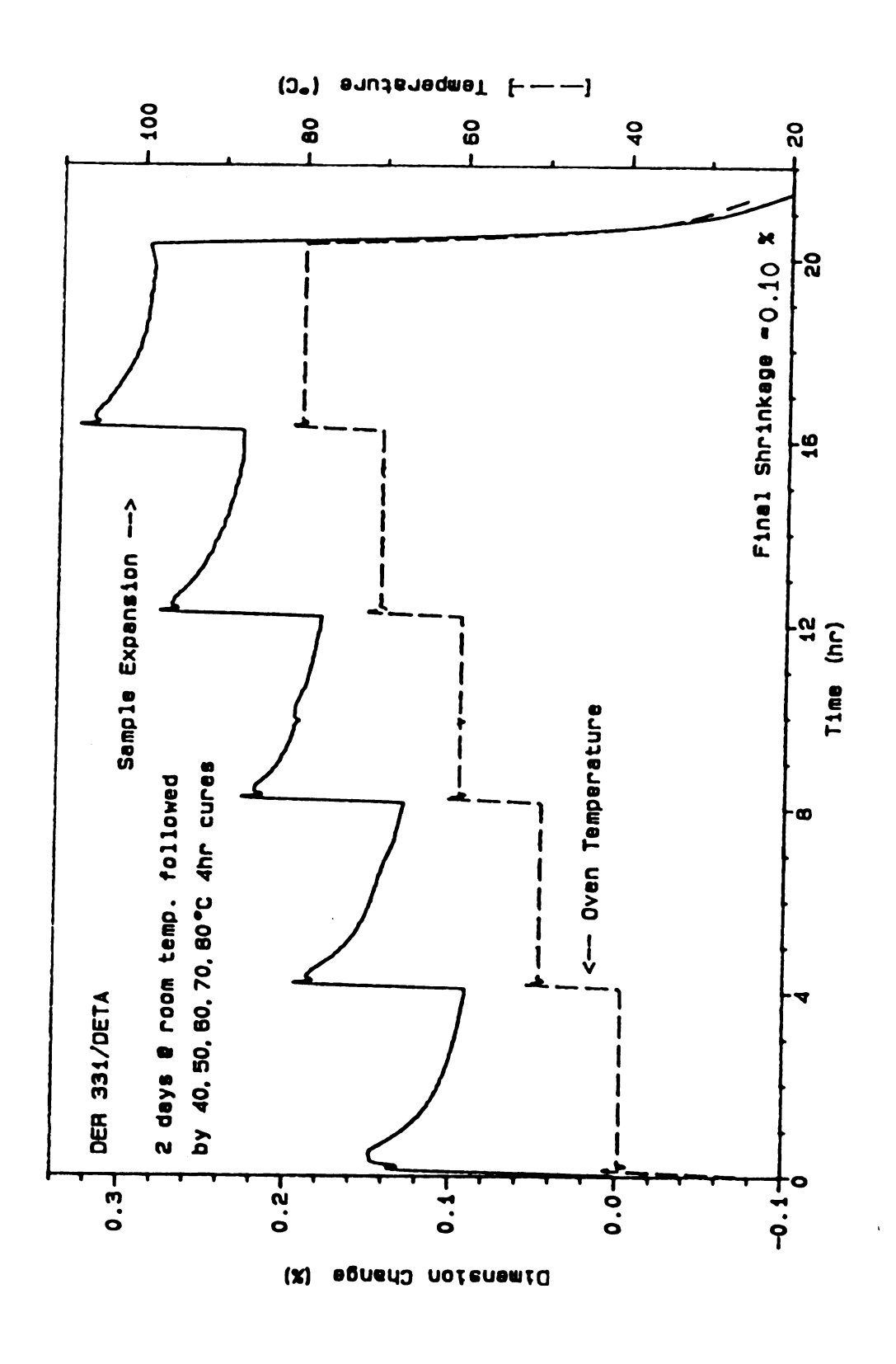


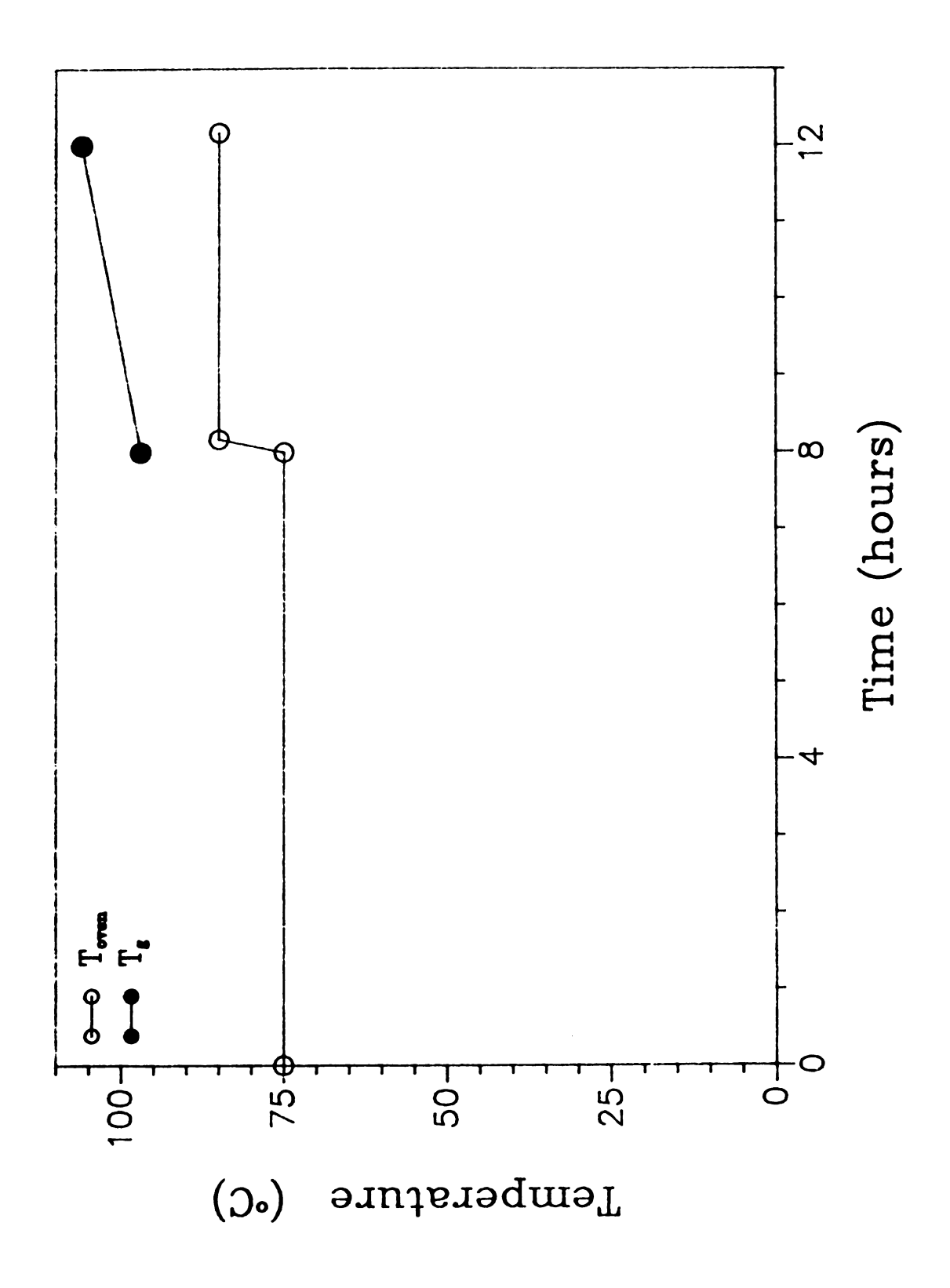
## Appendix C

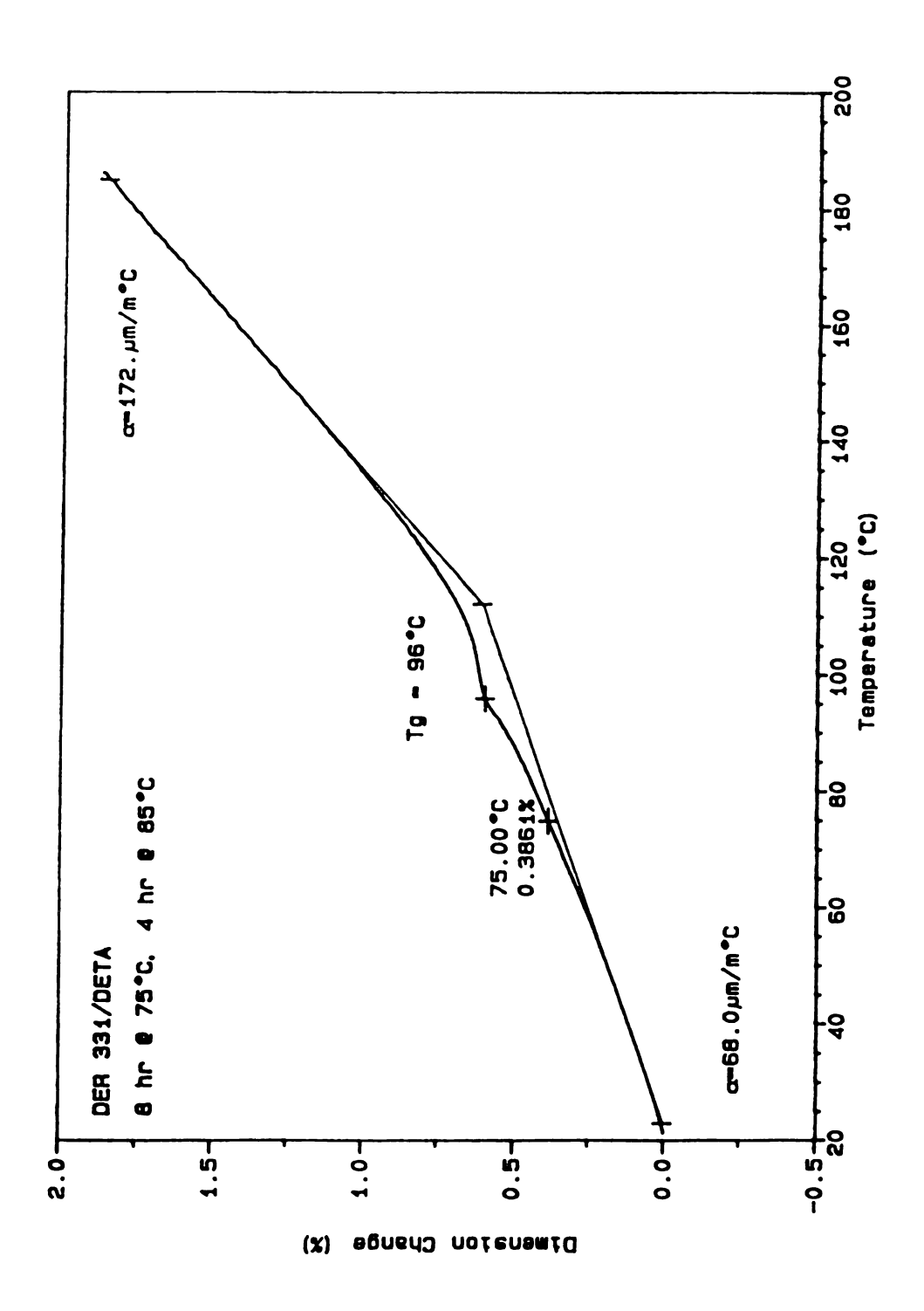
# Thermal Expansion & $T_g$ Data

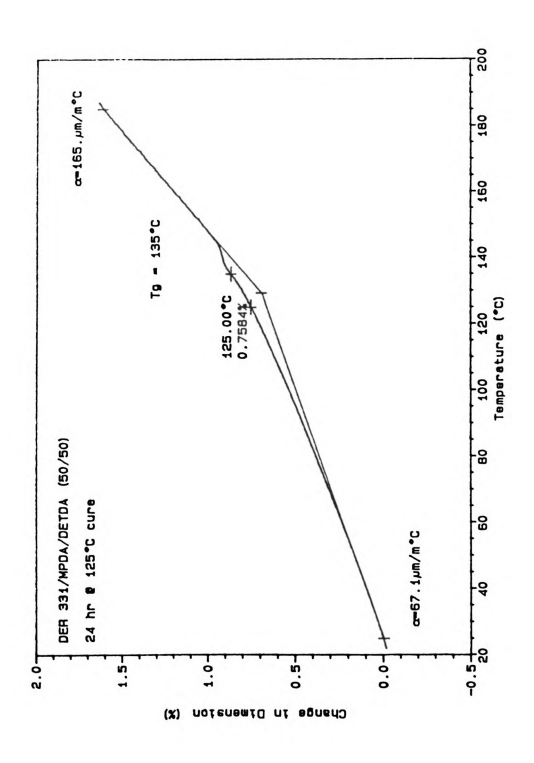
TMA plots of % thermal expansion of the 75°C, 125°C, and 175°C cured epoxies are presented. The plots also show the  $T_g$  of these epoxy systems. Plots of post-curing schedules for the room temperature and 75°C cured epoxy systems are also included.

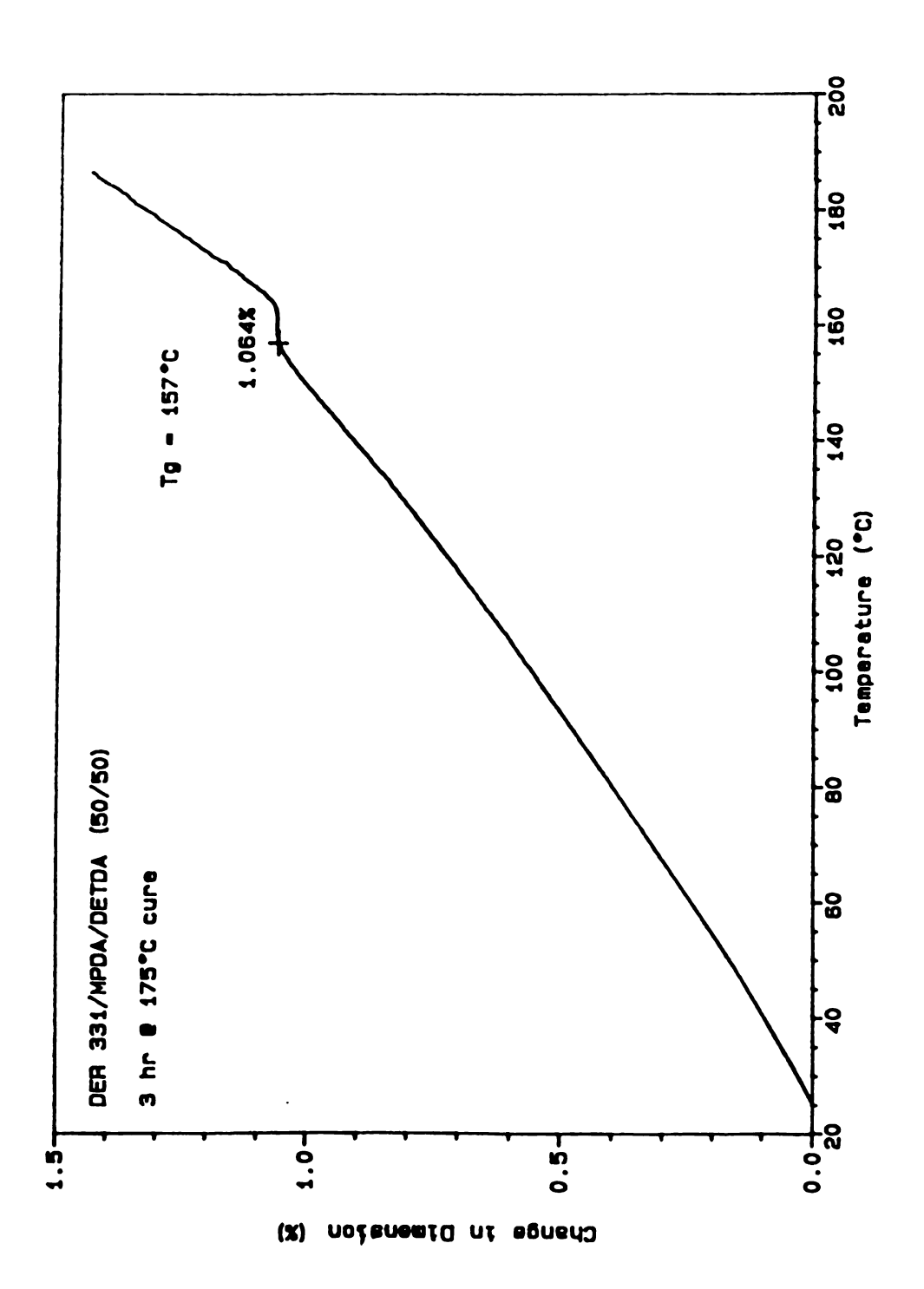


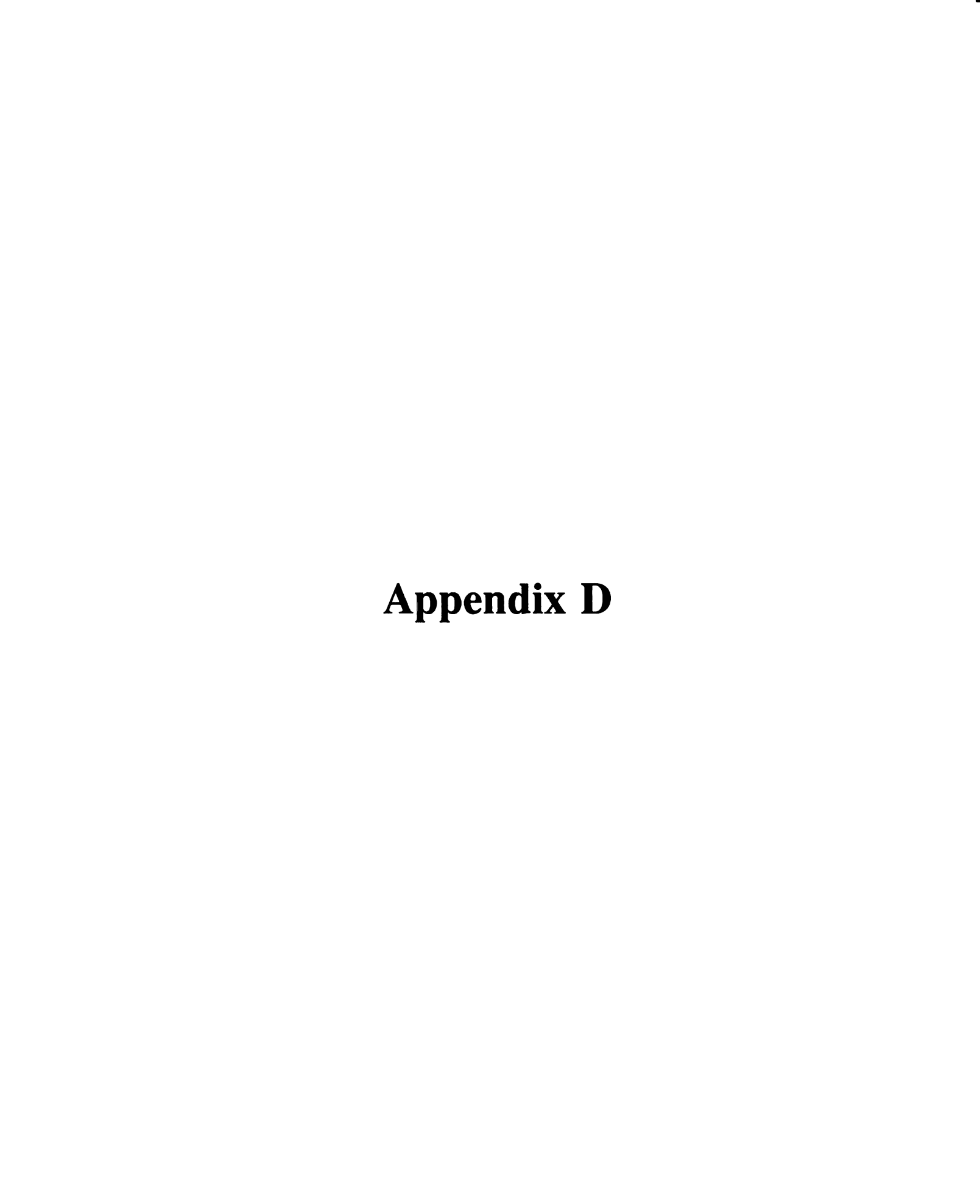












### Ultra-Thin Microtoming of Kevlar® 49 Fibers

In this appendix the techniques for microtoming the Kevlar fibers embedded in epoxy resins are discussed. For the benefit of others who may want to follow these technique, some of the encountered problems and ways to get around them are also mentioned.

### Introduction

An essential part of the TEM microscopy is the ultrathin microtoming of its samples. The TEM samples must be thin enough to transmit sufficient electrons to form an image. The samples must also be stable under the electron beam and in a high vacuum. TEM images are formed by combination of elastic, inelastic, and absorption interactions of the beam with the sample. Increasing the sample thickness increases the beam absorptions and reduces the image resolution and the beam stability. For a 100 kV electron beam the practical specimen thickness is limited to 100 nm.

#### **Procedure**

Kevlar fibers are embedded into epoxy dogbones as described in the dogbone preparation procedure. The gauge length of a dogbone is cut into  $\frac{1}{2}$  inch sections. The cuts are made with a razor blade, normally positioned and then tapped to fracture the section. The two halves of the first cut are examined to see which one has the pulled out fiber end, that half is chosen for the second cut. This inspection is necessary to avoid having samples with no embedded fibers. A sample is then placed into a sample holder and is clamped tightly. The sample is hand trimmed into a trapezoid of dimensions no longer than  $\frac{1}{4}$  mm. All the razor blades used in the above process are new blades and their edges are cleaned with ethanol soaked cotton swabs to avoid surface contamination.

The hand trimming of the trapezoid blocks is a very important step and needs further elaboration. The sample holder is placed under a sectioning microscope and the top face of the epoxy block is viewed at  $40\times$  magnification. The exposed pulled out fiber on the face helps to locate the position of the fiber. Four large blade marks of about 2 mm lengths are made to isolate the location of the fiber. With the fiber at the center of the blade marks, the epoxy outside the marks are trimmed at  $45^\circ$  angles. Next, two parallel cuts  $\sim \frac{1}{4}$  mm apart are made above and below the fiber. It is very important to have these two cuts parallel in order to have a good ribbon formation during the microtoming. Two more cuts at  $45^\circ$  to the two parallel cuts are made in order to form the final trapezoid block. All of these four cuts are normal to the face and about 1 mm deep. Finally, the top  $\frac{1}{2}$  mm of the trapezoid face is cut in order to remove the excess fiber and have a clean undamaged face for the microtoming.

Ultra-thin microtoming of the Kevlar samples requires a diamond knife. A 55° angle knife with 3 mm edge width has been purchased (Micro Star Co.). The right most  $\frac{1}{8}$  of the knife edge is dedicated to initial thick sectioning of the block. The next  $\frac{1}{8}$  of the knife edge is dedicated for the smoothing of the block face and experimenting with a new face for its ribbon formation behavior. The next  $\frac{1}{4}$  of the knife edge is dedicated for the final thin sectioning of the sample. The left  $\frac{1}{2}$  of the knife edge has not yet been used and will be used gradually as the rest of the edge becomes dull.

The sample holder is mounted into the microtoming arm and is fastened to avoid vibration problems. Attention was paid to make sure the longest edge of the sample trapezoid is facing down. The diamond knife is mounted at a 3° angle with respect to the block face. To wet and clean the diamond edge, the tip of a wooden applicator stick is shaved into a thin plate and is soaked in de-ionized water for at least 15 minutes. The boat of the knife is filled with de-ionized water and the diamond edge is wetted. The excess water is drawn off with a filter paper so that the surface of the fluid is concave behind the diamond edge. The knife is advanced manually toward the block face. Before the knife reaches the block, it is adjusted so that the right most  $\frac{1}{8}$  of the edge would touch the block first. The knife is then slowly advanced toward the block at 1 µm steps and block is manually moved. Once the cutting begins, several 1 µm sections are cut in order to prepare a clean smooth face for the thin sectioning. The knife is then receded and is shifted  $\frac{1}{8}$  of the edge to the left. Again the knife is slowly advanced until thin sections of gold or purple color are cut. Motorized sample advancing is turned on at 0.45 mm/sec speed and the thickness setting is adjusted to obtain gold colored sections. The ribbon formation of the sample is examined. If the ribbons do not form or badly tilted to a

side or the sections have cut marks, these indicate that the block face is not ready for the thin sectioning. If the ribbons do form but the sections are compressed and vary in thickness (i.e. color), that indicates that the water level is too high and then the water is drained until the problem is corrected. Once everything is ready for the thin sectioning, the knife is shifted to the middle  $\frac{1}{4}$  of its edge and the gold color sections are prepared at 0.33 mm/sec cutting speed.

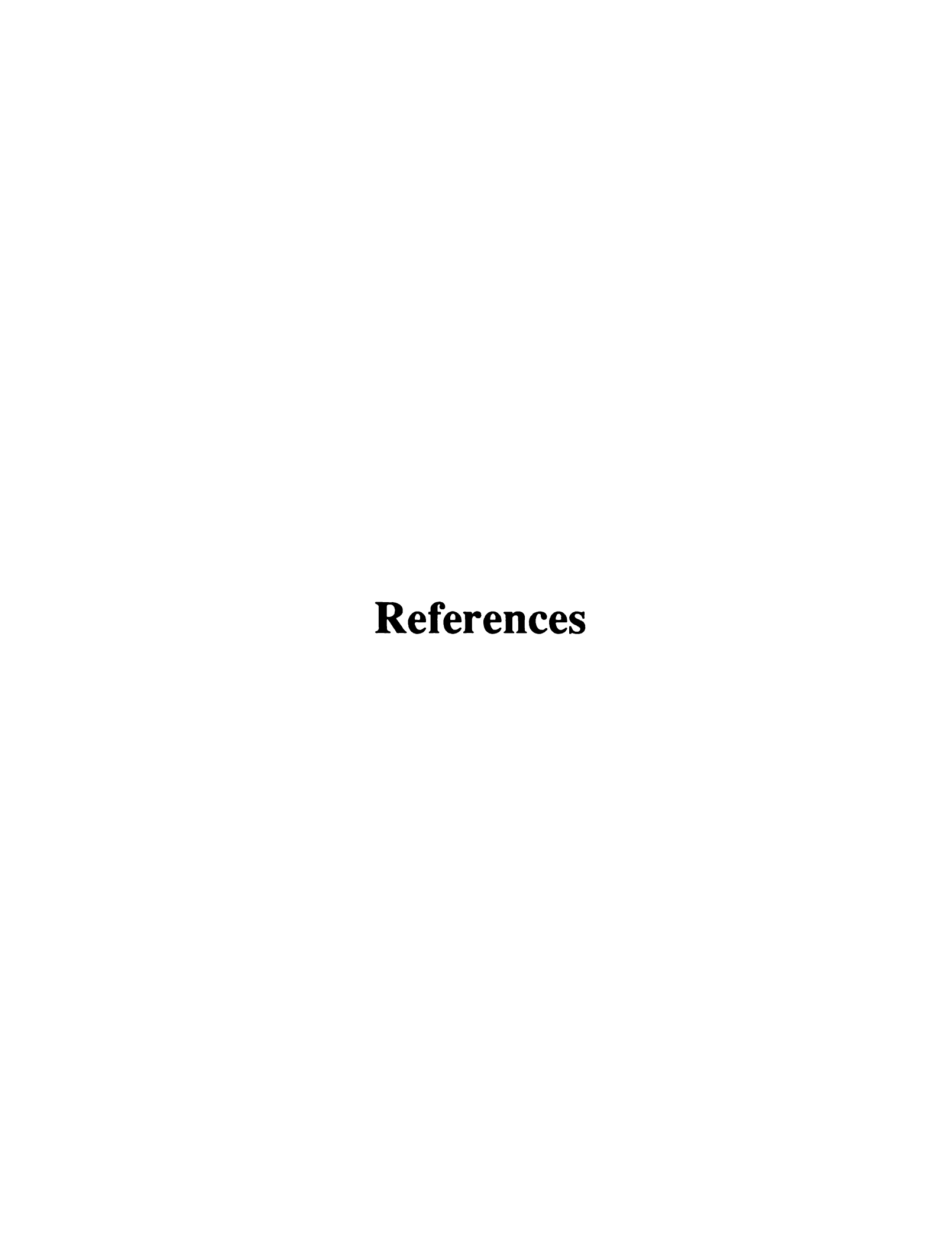
Sections form ribbons which float on the water. To manipulate ribbons, an eyelash applicator is prepared. An eyelash applicator is simply an eyelash mounted on a wooden applicator using a drop of nail-polish. With the eyelash applicator, the ribbons are assembled for the grid pick up. First the knife is receded and water is added to the boat. The ribbon sections are then arranged away from the diamond edge. The grids used are 200 mesh fine wire copper grids which have small end tabs for easy pick up. Under the microscope of the microtoming machine a grid is submerged in water and is approached underneath the assembled ribbons. The ribbons are picked up and the grid is drained on a filter paper. The grids are stored in a dessicator or treated for sample staining and carbon coating.

### **Special Comments**

The following statements summarize the important aspects of the described microtoming method plus a few other trouble-shooting suggestions.

-- Cutting speed of 0.33 mm/sec produces compression free sections.

- -- For untreated Kevlar samples with good epoxy adhesion, obtain gold coated sections, however, for poorly bonded samples such as silicone coated Kevlar samples obtain thicker gold-brown sections.
- -- Use of 3° knife angle produces compression free and uniform color ribbons and is recommended over the 2° and 4° knife angle settings.
- -- Always maintain the minimum water level possible without losing the meniscus. Sometimes it is hard to wet the diamond edge, to eliminate the problem, wet the eyelash applicator with your thong and then brush it against the diamond edge.
- -- Never breathe on the samples or use table light during the sectioning since they alter block dimensions.
- -- Fill up the boat with water before immersing the grid. Never pick up the ribbons from top because this can crumble your sections.
- -- 200 mesh fine wire grids are the best grids for our sample dimensions and provide good support with large exposed sample areas.



#### REFERENCES

- 1. Whitney, J.M., L.T. Drzal, Axi-Symmetric Stress Distribution Around An Isolated Fiber Fragment, ASTM STP, (in press).
- 2. Plueddeman, E.P., Interface in Polymer Matrix Composites, Academic, New York, (1974).
- 3. Agarwal, B.D. and L.J. Broutman, Analysis and Performance of Fiber Reinforceed Polymers, John Wiley and Sons, Inc. N.Y., (1980).
- 4. Drzal L.T., M.J. Rich, and S. Subramoney, "Fiber-Matrix and Its Effects On Composite Properties", *Proceeding of the Third Annual Conference on Advanced Composites*, Detroit MI, (Sept. 1987).
- 5. Owen M.J., "Fatigue of Carbon-Fiber-Reinforced Plastics", Fracture and Fatigue, L.J. Broutman ed., Academic Press, N.Y., pp. 341 (1974).
- 6. Peters P.W.M. and G.S. Springer, "Effects of Cure and Sizing on Fiber-Matrix Bond Strength", J. Composite Materials, 21, pp. 157, (1987).
- 7. Chang J., J.P. Bell and R. Joeseph, "Effects of a Controlled Modulus Interlayer Upon The Properties of Graphite/Epoxy Composite", SAMPE Quarterly, 18, pp. 39, (1987).
- 8. Mai Y.W. and F. Castino, "Fracture Toughness of Kevlar-Epoxy Composites with Controlled Interfacial Bonding", J. Material Science, 19, pp.1638, (1984).
- 9. Mark H. and A.V. Tobolsky, *Polymerscience and materials*, Ch. 11, New York, Wile-Interscience (1971).
- Takaho K., T. Katsura, K. Nakagawa and H. Makino, "High-Strength High-Modulus Polyimide Fibers I. One-Step Synthesis of Spinnable Polyimides", J. Applied Polymer Science, 32, pp. 3133, (1986).
- 11. Dvornic P.R., "Wholly Aromatic Polyamide-Hydrazides. IV. Structure-Property Relationships for Polymers Containing p-Phenylene and m-Phenylene Units", J. Polymer Scince: Part A: Polymer Chemistry, 24, pp.1133, (1986).
- 12. Magat E.E., "Fibers from extended chain aromatic polyamides", *Phil. Trans. R. Soc. Lond. A*, 294, pp. 463 (1980).
- 13. Preston J., "High-Strength/High-Modulus Organic Fibers", Poly. Engineering and Sciences, 15, pp.199, (1975).

- 14. Langston P.R., "Aramid Polymers, Their Properties and Application", 32nd International SAMPE Symposium, pp. 1399, (April 1987).
- 15. Tashiro K., M. Kobayashi and H. Tadokoro, Macromolecules, 10, pp. 413, (1977).
- 16. Carter G.B. and V.T.J. Schenk, *The Structure and Properties of Oriented Polymers*, I.M. Ward, Ed., Applied Science, London, Chap. 13 (1975).
- 17. Dobb M.G., D.J. Johnson and B.P. Saville, "Supramolecular Structure of a High-Modulus Polyaromatic Fiber (Kevlar 49)", J. Poly. Sci., Polym. Phys. Ed., 15, pp. 2201, (1977).
- 18. Morgan R.J., C.O. Pruneda, and W.J. Steele, "The Relationship between the Physical Structure and the Microscopic Deformation and Failure Processes of Poly(p-Phenylene Terephthalamide) Fibers", J. Poly. Sci.: Poly. Phy. Ed., 21, pp. 1757, (1983).
- 19. Chatzi E.G., M.W. Urban and J.L. Koening, "Characterization of Kevlar Fiber Surface Using a Newly Developed Infrared Photoacoustic Technique", *Makromol. Chem.*, *Macromal. Symp.*, 5, pp. 99, (1986).
- 20. Brown I.M., T.C. Sandreczki and R.J. Morgan, "Electron Paramagnetic Resonance of Kevlar 49 Fibers: Stress-Induced free radicals", *Polymer*, 25, pp. 759, (1984).
- 21. Morgan R.J. and R.E. Allred, Aramid Fiber Reinforcements, Technomic, S.M. Lee Ed., (in press).
- 22. Blades H., Dry-Jet Wet Spinning Process, U.S. Patent 3,767,756, Oct. 23, (1973).
- 23. Morgan R.J. and C.O. Pruneda, "The Characterization of the Chemical Impurities in Kevlar 49 Fibbers", *Polymer*, 28, pp.340, (1987).
- 24. Penn L. and F. Larsen, "Physicochemical Properties of Kevlar 49 Fibers", J. Appl. Poly. Sci., 23, pp. 59, (1979).
- 25. Ashbee E. and K.H.G. Ashbee, "Glauber's Salt Heaving in Kevlar 49 Fibers", J. Materials Science Letters, 4, pp. 249, (1985).
- 26. Whalley W.B., B.J. Smith and J.P. Greevy, "Decay of Kevlar", J. of Materials Science Letters, 5, pp. 342, (1986).
- 27. Lee J.S., J.F. Fellers and M.Y. Tang, "A Dynamic Small Angle X-ray Scattering Study of Stresses Kevlar 49/Epoxy Composites", J. Composite Materials, 19, pp. 114, (1985).
- 28. Chiao C.C. and T.T. Chiao, "Aramid Fibers and Composites", Handbook of Composites, Ch. 12, pp. 272, New York, Van Nostrand Reinhold Co., (1982).
  - 29. Kompaniets L.V., V.V. Potapov, G.A. Grigorian, E.V. Prut and N.S. Enikolopian, "Statical Aspects of Tensile Strength of Aramid Fibers and Unudirectional Composites", *Polymer Composites*, 6, pp. 54, (1985).

- 30. Knoff W.F., "A Modified Weakest-Link Model for Describing Strength Variability of Kevlar Aramid Fibers", J. Materials Science, 22, pp. 1024, (1987).
- 31. DeTeresa S.J., R.J. Porter and R.J. Farris, "A Model for the Compressive Buckling of Extended Chain Polymers", J. of Materials Science, 20, pp. 1645, (1985).
- 32. DeTeresa S.J., R.J. Porter, R.J. Farris and S.R. Allen, "Compressive and Torsional Behavior of Kevlar 49 Fiber", J. Materials Science, 19, pp. 57, (1984).
- 33. White J.R., T.J. Lardner, "Mechanical Model to Describe the Behavior of Polyaramid Fibers", J. Materials Science, 19, pp. 2387, (1984).
- 34. Wagner H.D., P. Schwartz and S.L. Phoenix, "Lifetime Statistics for Single Kevlar 49 Filaments in Creep-Rupture", J. Material Science, 21, pp. 1868, (1986).
- 35. Lafitte M.H. and A.R. Bunsell, "The Creep of Kevlar-29 Fibers", *Polymer Engineering and Science*, 25, pp. 182, (1985).
- 36. Lafitte M.H. and A.R. Bunsell, "The Fatigue Behavior of Kevlar-29 Fibers", J. of Materials Science, 17, pp. 2391, (1982).
- 37. Cook R., "A simple Kinetic Approach to Fiber Failure: 2. Lifetime distributions", *Polymer*, 27, pp. 1895, (1986).
- 38. Dickinson J.T., A. Jahan-Latibari an L.C. Jensen, "Fracto-Emission from Single Fibers of Kevlar", J. Materials Science, 20, pp. 1835, (1985).
- 39. Hamstad M.A. and R.L. Moore, "Acoustic Emission from Single and Multiple Kevlar 49 Filament Breaks", J. Composite Materials, 20, pp. 46, (1986).
- 40. Wagner H.D., "A Model for Longitudinal Splitting from Surface Defects in Anisotropic Filaments", J. Materials Science Letters, 5, pp. 229, (1986).
- 41. Riggs D.M., R.J. Shuford and R.W. Lewis, "Graphite Fibers and composites", *Handbook of Composites*, G. Lubin, ed., Van Nostrand Reinhold Co. New York, pp. 196 (1982).
  - 42. Donnet J. and R.C. Bansal, *Carbon Fibers*, International Fiber Science and Technology Series, 3, Marcel Dekker Inc., New York, (1984).
  - 43. Diefendorf R.J. and E.W. Tokarsky, "The relationships of Structure to Properties in Graphite Fibers, Part I", AFML-TR-72-133, (1973).
  - 44. Drzal L.T. and M.J. Rich, "Effects of Graphite Fiber/Epoxy Matrix Adhesion on Composite Fracture Behavior", Special Technical Testing Publication 864, ASTM, (1985).
  - 45. Phani K.K., "The Strength-Length Relationship for Carbon Fibers", Composite Science and Technology, 30, pp. 59, (1987).

- 46. Prime R.B., "Thermosets", *Thermal Characterization of Polymeric Materials*, Chapter 5, ed. Turi, Academic Press, London, (1981).
- 47. Barton J.M., "The application of Differential Scanning Calorimetry (DSC) to the Study of Epoxy Resin Curing Reactions", Advances in Polmer Science, 72, pp. 112, (1980).
- 48. Lee N. and K. Neville, Handbook of Epoxy Resins, McGraw-Hill, (1967).
- 49. Moroni A., J. Mijovic, E.M. Pearce and C.C. Foun, "Cure Kinetics of Epoxy Resins and Aromatic Diamines", J. Applied Polymer Science, 32, pp. 3761, (1986).
- 50. Wiggins P.L., "Curing Acceleration of a Hindered Aromatic Diamine-Epoxy System", SAMPE Quarterly, (1986).
- 51. Gupta V.B., L.T. Drzal, C.Y. Lee and M.J. Rich, "The Temperature-Dependence of Some Mechanical Properties of a Cured Epoxy Resin Sysytem", *Poly. Eng. and Sci.*, 25, pp. 812, (1985).
- 52. Bellenger V., J. Verdu and E. Morel, "Effects of Structure on Glass Transition Temperature of Amine Crosslinked Epoxies", J. Poly. Sci: Part B: Poly. Physics, 25, pp. 1219, (1987).
- 53. Gupta V.B., L.T. Drzal and M.J. Rich, "The Physical Basis of Moisture Transport in a Cured Epoxy Resin System", J. Applied Polymer Science, 30, pp. 4467, (1985).
- 54. Jean Y.C., T.C. Sanderczki and D.P. Ames, "Positronium Annihilation in Amine-Cured Epoxy Polymers", J. Polymer Science: Part B: Ploymer Physics, 24, pp. 1247, (1986).
- 55. Lee S.M., "Plastic Deformation in Epoxy Resins", Abstracts of Papers of the ACS, 193, pp. 65, (1987).
- 56. Mittelman H.H., I. Roman and G. Marom, "The Morphology of Shear Fracture of Kevlar Fiber-Reinforced Epoxy Composites", J. Material Science Letters, 4, pp. 1361, (1985).
- 57. Smith P.A., D.G. Gilbert and A. Poursartip, "Matrix Cracking of Composites Inside a Scanning Electron Microscope", J. Material Science Letters, 4, pp. 845, (1985).
- 58. Wu, S., "Polymer Interface and adhesion", Marcel Dekker, Inc. New York (1982).
- 59. Bjorksten J. and L.L. Yaeger, "Vinyl Silane Size for Glass Fabrics", Mod. Plast., 29, pp. 124, (1952).
- 60. Cooke T.F., "High Performance Fiber Composites with Special Emphasis on the Interface", J. Poly. Eng., 7, pp. 197, (1987).
- 61. Penn L.S., F.A. Bystery and H. Marchionni, "Relation of Interfacial Adhesion in Kevlar/Epoxy Systems to Surface Characterization and Performance", *Poly. Composites*, 4(1), pp. 27, (1983).

- 62. Wertheimer M.R. and H.P. Schreiber, "Surface Property Modification of Aromatic Polyamides by Microwave Plasmas", J. Appl. Poly. Sci., 26, pp. 2087, (1981).
- 63. Allred R.E., E.W. Merrill and D.K. Roylance, Molecular Characterization of Composite Interfaces, H. Ishida and G. Kumar, Eds, Plenum Press, New York, pp. 333, (1985).
- 64. Wu Y. and G.C. Tesoro, "Chemical Modification of Kevlar Fibers Surface and of Model Diamides", J. Appl. Poly. Sci., 31, pp. 1041, (1986).
- 65. Allen K.W., "A Review of Contemporary Views of Theories of Adhesion", J. Adhesion, 21, pp. 261, (1987).
- 66. Huntsberger J.R., Treatise on Adhesion and Adhesives, Chap. 4, 1, R.L. Patrick, Ed. Edward Arnold Ltd. London, (1966),
- 67. Timm D.C., A.J. Ayorinde and C.H. Lee, "Kevlar 49 Composite Performance: Dependence on Thermoset Resin Microstructure", *Poly. Eng. and Sci.*, 24, pp. 930, (1984).
- 68. Garton A. and J. H. Daly, "Characterization of the Aramid:Epoxy and Carbon:Epoxy Interphase", *Polymer Composite*, 6, pp. 195, (1985).
- 69. Chatzi E.G., M.W. Urban and J.L. Koening, "Determination of the Accessibility of N-H Groups of Kevlar 49 by Photoacoustic FTi.r. Spectroscopy", *Polymer*, 27, pp. 1850, (1986).
- 70. Chappell P.J.C. and D.R. Williams, "Surface Characterization of Kevlar By Inverse Gas Chromatography", *Proceeding of ICCM VI*, (1987).
- 71. Voyutskii S.S, Autohesion and Adhesion of High Polymers, Wiley-Interscience, New York, (1963).
- 72. Cherry B.W., Polymer Surfaces, Cambridge University Press, Cambridge, (1981).
- 73. Piggott M.R., P.S. Chua and D. Andison, "The Interface Between Glass and Carbon Fibers and Thermosetting Polymers", *Polymer Composites*, 6, pp. 242, (1985).
- 74. Kevlar 49 Data Manual, DuPont de Nemours Chemical Co., Wilmington, Delaware, (1974).
- 75. Mai Y.W. and F. Castino, "The Debonding and Pull-Out Properties of Coated Kevlar Fibers from an Epoxy Resin Matrix", J. Mat. Sci. Let., 4, pp. 505, (1985).
- 76. Reedy E.D., "Fiber Stress Concentrations in Kevlar/Epoxy Monolayers", J. Composite Materials, 19, pp. 533, (1985).
- 77. Shih G.C. and L.J. Ebert, "Theoretical Modelling of the Effect of the Intefacial Shear Strength on the Longitudinal Tensile Strength of Unidirectional Composites", J. of Composite Materials, 21, pp.207 (1987).

- 78. Nairn J.A. and P. Zoller, "Matrix Solidification and the Resulting Residual Thermal Stresses in Composites", J. Material Science, 20, pp. 355, (1985).
- 79. Rojstaczer S., D. Cohn and G. Marom, "Thermal Expansion of Kevlar Fibers and Composites", J. Material Science Letters, 4, pp. 1233, (1985).
- Hull D., An Introduction to Composite Materials, Cambridge University Press, Cambridge, (1981).
  - 81. Penn L., F. Bystry, W. Karp and S. Lee, "Aramid/Epoxy vs. Graphite/Epoxy: Origin of the Difference in Strength at the Interface", *Poly. Sci. and Technol.*, pp. 93, (1985).
  - 82. Fiber Composite Analysis and Desgin, Vol. 1 Composite Materials and Laminates, prepared by Material Science Corporation, U.S. Department of Transportation, Federal Aviation Administration, (1984).
  - 83. Drzal L.T, "Interfacial Behavior of Aramid and Graphite Fibers in an Epoxy Matrix", 15th National SAMPE Tech. Conf., Cincinati OH, (1983).
  - 84. Sharpe L.H., H. Schonhorn and R.F. Gold, Contact Angle, Wettability and Adhesion, ACS, Washington, D.C., (1964).
  - 85. Li S.K., R.P. Smith and A.W. Neumann, "Wihelmy Technique and Solidification Front Technique to Study the Wettability of Fibers", J. Adhesion, 17, pp. 105, (1984).
  - 86. Wesson S.P. and R.E. Allred, *Proc. of 7th Annual Meeting of the Adhesion Society*, Jacksonville Fl., pp. 27, (1984).
  - 87. Miller B., P. Muri and L. Rebenfeld, "A Microbond Method for Determination of the Shear Strength of a Fiber/Resin Interface", *Composite Science and Technology*, 28, pp. 17, (1987).
  - 88. Penn L.S., T.J. Byerley and T.K. Liao, "The Study of Reactive Functional Groups in Adhesion Bonding at the Aramid-Epoxy Interface", J. Adhesion, 23, pp. 163, (1987).
  - 89. Kelly A. and W. Tyson, "Fiber-Strengthened Materials", *High Strength Materials*, Ch. 13, V. Zackay, ed., John Wiley and Sons, New York (1965).